

**PHOTOCATALYTIC AND CATALYTIC ROUTES FOR
REMOVAL OF POLLUTANTS PRESENT IN WATER AND
AIR**

A THESIS

submitted by

G. MAGESH

for the award of the degree

of

DOCTOR OF PHILOSOPHY



**DEPARTMENT OF CHEMISTRY
INDIAN INSTITUTE OF TECHNOLOGY MADRAS
CHENNAI – 600 036**

APRIL 2010

Dedicated to my parents

THESIS CERTIFICATE

This is to certify that the thesis entitled “**PHOTOCATALYTIC AND CATALYTIC ROUTES FOR REMOVAL OF POLLUTANTS PRESENT IN WATER AND AIR**” submitted by **G. Magesh** to the Indian Institute of Technology Madras, Chennai, INDIA for the award of the degree of **Doctor of Philosophy** is a bonafide record of research work carried out by him under our supervision. The contents of this thesis, in full or in parts, have not been submitted to any other Institute or University for the award of any degree or diploma.

Research Guides

Prof. R.P. Viswanath
Department of Chemistry
IIT Madras

Prof. T.K. Varadarajan
Department of Chemistry
IIT Madras

Chennai – 600 036

Date:

ACKNOWLEDGEMENTS

I am deeply indebted to my research guides **Prof. R.P. Viswanath** and **Prof. T.K. Varadarajan** for their incessant encouragement, thought provoking discussions and unfailing guidance at every stage of the research programme. It gives me immense pleasure to have been associated with them. It is my privilege to express my gratitude to them for introducing me to the field of catalysis. I thank them for their patient guidance, open discussions, constant encouragement, unbounded enthusiasm and interest and I owe them a great intellectual and inspirational debt.

I express my sincere gratitude to **Prof. B. Viswanathan** for his inspiring, invaluable guidance, constant encouragement and thought provoking discussions through out the research work. I am really grateful to him for providing opportunities to learn various aspects in catalysis. I feel privileged to have been associated with him.

I sincerely thank the former Heads of Department of Chemistry, **Prof. S. Vancheesan** (late), **Prof. M.N. Sudheendra Rao**, **Prof. G. Sundararajan** (late) and the present Head of the Department of Chemistry, IIT Madras, **Prof. R. Dhamodharan**, for their help, suggestions and for providing the necessary infrastructural facilities during my research.

I express my thanks to all my doctoral committee members **Prof. G. Ranga Rao**, **Prof. M.V. Sangaranarayanan**, **Prof. K. Hariharan** and **Prof. P.S.T. Sai**, **Prof. M.S. Subramanian** and **Prof. D.V.S. Murthy** for their constant encouragement and valuable suggestions. I thank all the **faculty** members of the **Department of Chemistry** who have taught the various courses and for their constant help and suggestions during various stages of the programme.

I am very much thankful to **Dr. S. Sivasanker**, **Prof. P. Selvam**, **Dr. K.R. Krishna Murthy**, **Dr. A.V. Ramasamy** of NCCR for their constant support and invaluable suggestions during the discussions.

I express my sincere thanks to **Prof. L. Guzzi, Dr. Z. Schay and Dr. Andrea** of Institute of Isotopes, Hungary, for their valuable guidance, help and support. I am very much thankful to **Dr. Kriztina** and **Ms. Timea** for their help during my stay in Hungary.

I gratefully acknowledge **CSIR, New Delhi**, for the financial assistance. I am thankful to the **DST, New Delhi** for creating the **National Centre for Catalysis Research** where in I have carried out most of my research work.

My sincere thanks are due to all the staff members of **Department of Chemistry**. I thank the **Head and staff members of CGBS, SAIF and Department of Metallurgy IIT Madras** for providing the necessary instrumentation facilities. I am thankful to **Mr. Narayanan, Mr. Ramkumar, Mrs. Kanchanamala, Mrs. Shanti, Mr. Ragavaiah and Mrs. Bhavani Kumar** for their untiring and immediate help.

Words are inadequate to express my heartfelt gratitude to **Mr. Murali, Mr. Gomathi shankar, Mr. Justin, Mr. Mathiselvam, Mr. Karthikeyan, Dr. Jeyakumar, Mr. Charan and Mr. Sumanta** with whom I have spent many memorable occasions and who have been very helpful & supportive both in personal and academic.

I would like to place my sincere thanks to my senior lab mates, **Dr. Sathish, Dr V. Chidambaram, Dr. M. Sankaran, Dr. P. Suresh, Dr. Ganesan, Dr. Shanmugam, Dr. Jothiramalingam, Dr. Srimurugan, Dr. Himakumar, Dr. Venkateswara Rao, Dr. Meialagan, Dr. Kishore, Dr. Rajeswari, Dr. Helen and Dr. Chandravathanam** for their timely help, friendship and encouragement, which they have extended to me at IIT Madras.

I am extremely grateful to **Dr. T.S.N. Sankaranarayanan** of CSIR, Taramani for his encouragement and support. My thanks are due to my M.Sc. teachers **Dr. V. Murugesan, Dr. N. Rajendran and Dr. M. Palanisamy** for the constant support and encouragement.

I thank my colleagues **Mr. Indra Neel, Mr. Kuppan, Ms. Banu, Mr. Suthagar, Mr. Sankaranarayanan, Mr. Vamsi, Mr. Ramana, Mr. Mahendran, Ms. Nithya, Mr. Poliraju, Dr. Vidya, Dr. George, Dr. Sangeeta, Dr. Mahalakshmi, Dr. Radhika, Dr. Joyce, Dr. Sabiah, Dr. Murugan, Ms. Indumathi, Ms. Kiruba, Dr. Anuradha, Dr. Joseph, Dr. Thirunavukkarasu, Mr. Anil, Ms. Alagarasi, Mr. Venkatesan, Mrs. Premalatha, Ms. Smitha, Mr. Pachamuthu, Ms. Gomathi, Mr. Prakash, Ms. Sandhya, Mr. Vinoth, Ms. Deepa, Ms. Divya and Mrs. Geetha** for their help in all aspects.

I am also thankful to **Mr. Tarjan, Mr. Srinivasan, Mr. Manjunath, Dr. Sivakumar, Mr. Akbar, Mr. Manoj, Mr. Velkannan, Mr. Ramkarthik, Dr. Raghuraman, Mr. Karunanithi, Mr. Sivaraman, Mr. George, Mr. Muthukrishnan, Dr. David, Dr. Subramaniam, Dr. Vijay shankar, Dr. Vijay, Dr. Rajkumar, Dr. Vivek and Mr. Sudhakar** for their help at various stage of my research.

I express my sincere thanks to my B.Sc., M.Sc. classmates and friends **Mr. Selvabharathi, Mr. Thiru, Mr. Raja, Mr. Venugopal, Mr. Palani, Mr. Jermi, Mr. Ravi, Mr. Somanathan, Mr. Gokul, Mr. Selvaganapathi, Mr. Chandrasekar and Mr. Sathish, Mr. Premnath and Mr. Sivakumar** for their help and the valuable time which we have spent together.

My thanks are due to **Mr. Raja, Mr. Kumar, Mr. Umapathi,** for their help in printing and photocopying throughout the programme.

Last but not least I owe everything to **my grand mother, father (late), mother, brother, sister and relatives** for their constant support and encouragement whenever needed, without them it would have been impossible for me to complete this work.

G . Magesh

ABSTRACT

KEY WORDS: Photocatalysis, CeO₂-TiO₂, carbon-TiO₂, degradation of methylene blue, degradation of *p*-chlorophenol, cadmium stannates, water splitting, oxidation of CO, pollutant removal

The environment receives more and more pollutants these days due to growing population and increase in the industrial activity. The remediation of pollutants in water has attracted considerable interest, since most of the pollutants are soluble in water. Utilising the energy from sunlight for the decontamination of water would be the ideal situation. One of the ways of achieving such a goal is by the photocatalytic means. Sunlight is composed of 6 % of UV light and 48 % visible. The most affordable and stable photocatalyst, TiO₂, functions only with UV light because of its larger bandgap. Various methods have been studied to decrease the bandgap of TiO₂ so that it can absorb light in the visible region so that it can be effectively utilised as a photocatalyst for pollutant degradation.

CeO₂, which has a bandgap suitable for absorption of light in the visible region, suffers from large recombination of photogenerated charge carriers. Coupling CeO₂ and TiO₂ is expected to reduce the recombination, since the conduction band (CB) energy of CeO₂ is suitable for transfer of electrons to the CB of TiO₂. The present study involves the usage of CeO₂ modified TiO₂ systems as photocatalysts for the degradation of methylene blue using UV and visible light.

Adsorption of target pollutant molecules on the surface is an important step in the photocatalytic process, whereas TiO₂ does not have good adsorption of organic molecules. Carbon is a well known adsorbent and has its Fermi level suitable for

accepting excited electrons from TiO_2 . Hence, the photocatalytic activity of carbon- TiO_2 composites for the degradation of methylene blue has been studied.

Another strategy is to choose or develop new photocatalysts which can utilize visible light and are stable and easily available. Oxides of elements with completely filled *d*-orbitals are expected to have a shorter bandgap. Based on this, oxides of Cd and Sn have been studied for their photocatalytic activity towards degradation of *p*-chlorophenol. Their flat band potentials have been determined from Mott-Schottky plots in order to find out their ability to photo-split water to evolve hydrogen.

Industries and vehicles using fossil fuels cause pollution of the air by evolving CO_2 , CO, NO_x and sulphur oxides. Among them, CO can cause various health problems and is fatal at higher concentrations in the atmosphere. Gold when supported on various supports is active in converting CO to CO_2 . Gold supported on different crystalline phase of TiO_2 are studied as catalysts for oxidation of CO. Results showed that not only the support but also the method of deposition of gold on the support plays a significant role in the activity of the catalyst.

TABLE OF CONTENTS

	Title	Page No.
	ACKNOWLEDGEMENT	i
	ABSTRACT	iv
	LIST OF TABLES	xi
	LIST OF FIGURES	xii
	LIST OF SCHEMES	xv
	ABBREVIATIONS	xvi
	NOTATIONS	xvii
	CHAPTER 1 INTRODUCTION	
1.1	Pollution.....	1
1.2	Water pollution	1
1.3	Methods of water treatment	2
1.4	Advanced oxidation processes.....	3
1.4.1	Fenton processes	6
1.4.2	Photo assisted Fenton processes	7
1.4.3	Ozonisation process.....	7
1.4.4	Photocatalysis	8
1.5	Photocatalysis	10
1.5.1	Heterogeneous photocatalysis.....	10
1.5.2	Charge carrier trapping.....	12
1.5.3	Semiconductor-electrolyte interface	13
1.5.4	Effect of electron-hole recombination.....	16
1.5.5	Importance of position of energy levels	17
1.5.6	Choice of photocatalyst	19
1.5.7	Visible light photocatalysis.....	20
1.5.8	Importance of adsorption in heterogeneous photocatalysis.....	21
1.5.9	Alternatives to TiO ₂ photocatalyst	22
1.6	Air pollution.....	23
1.6.1	Pollution caused by carbon monoxide.....	23

Table of contents (Contd.,)		Page No.
1.7	Carbon monoxide oxidation.....	25
1.7.1	Kinetics of oxidation of CO at low pressure.....	26
1.7.2	Oxidation of CO by Au	27
1.8	Motivation and scope of the present work.....	29

CHAPTER 2 EXPERIMENTAL METHODOLOGY

2.1	Chemicals and materials used.....	31
2.2	Preparation of the catalyst	31
2.2.1	Preparation of Ce modified TiO ₂	31
2.2.2	Preparation of carbon-TiO ₂ composites	32
2.2.3	Preparation of CdSnO ₃ and Cd ₂ SnO ₄	33
2.2.4	Preparation of Au/TiO ₂	34
2.2.4.1	Preparation of TiO ₂ from TiCl ₄	34
2.2.4.2	Preparation of TiO ₂ from TiCl ₃	34
2.2.4.3	Gold loading on TiO ₂ by sol deposition method	35
2.2.4.3.1	Preparation of gold sol	35
2.2.4.3.2	Adsorption of gold sol on TiO ₂	35
2.2.4.4	Gold loading on TiO ₂ by deposition precipitation method	36
2.3	Characterization	37
2.3.1	Diffuse reflectance UV-visible spectrophotometric studies.....	37
2.3.2	Powder X-ray diffraction.....	37
2.3.2.1	Crystallite size determination by XRD line broadening	37
2.3.3	Surface area measurements.....	38
2.3.4	Transmission electron microscopic studies (TEM).....	38
2.3.5	Scanning electron microscopic studies (SEM)	38
2.3.6	Thermogravimetric analysis (TGA).....	39
2.3.7	UV-visible spectrophotometry	39
2.3.8	Infrared absorption studies (IR).....	39
2.3.9	Inductively Coupled Plasma analysis (ICP)	39
2.4	Photocatalytic activity	40
2.4.1	Photocatalytic degradation of methylene blue using Ce-TiO ₂	40

Table of contents (Contd.,)		Page No.
2.4.2	Photocatalytic degradation of methylene blue using carbon-TiO ₂ composites	40
2.4.3	Photocatalytic degradation of <i>p</i> -chlorophenol using CdSnO ₃ and Cd ₂ SnO ₄	41
2.4.4	Photocatalytic hydrogen evolution studies	41
2.5	Estimation of cerium by colourimetry.....	42
2.6	Adsorption and desorption experiments	42
2.7	Impedance measurements.....	43
2.8	Catalytic oxidation of CO using Au/TiO ₂	43
2.9	Chemical oxygen demand analysis (COD)	44

CHAPTER 3 CHARACTERIZATION AND PHOTOCATALYTIC ACTIVITY OF Ce MODIFIED TiO₂

3.1	Introduction.....	46
3.2	Results and discussion.....	49
3.2.1	X-ray diffraction studies.....	49
3.2.2	Diffuse reflectance UV-visible spectral studies.....	50
3.2.3	TEM and SEM analysis.....	52
3.2.4	TGA and Elemental analysis	55
3.2.5	Adsorption and photocatalytic studies	56
3.2.6	Mechanism for the activity in visible light	59
3.2.7	Optimum loading of cerium on TiO ₂	63
3.2.8	Photocatalytic activity in UV light.....	65
3.3	Conclusions.....	66

CHAPTER 4 CHARACTERIZATION AND PHOTOCATALYTIC STUDIES OF CARBON-TiO₂ COMPOSITES

4.1	Introduction	67
4.2	Results and discussion	69
4.2.1	X-ray diffraction patterns	69
4.2.2	Raman spectral studies	71
4.2.3	SEM studies	72
4.2.4	TEM studies.....	75

Table of contents (Contd.,)		Page No.
4.2.5	Diffuse reflectance UV-visible spectral studies.....	78
4.2.5.1	Carbon-TiO ₂ from TiCl ₃	78
4.2.5.2	Carbon-P25 TiO ₂	78
4.2.6	Photocatalytic experiments.....	80
4.2.6.1	Photocatalytic activity of carbon-TiO ₂ from TiCl ₃	80
4.2.6.2	Photocatalytic activity of carbon-P25 TiO ₂	81
4.3	Conclusions.....	83

**CHAPTER 5 CHARACTERIZATION, PHOTOCATALYTIC AND
ELECTROCHEMICAL STUDIES OF CdSnO₃ AND Cd₂SnO₄**

5.1	Introduction.....	84
5.2	Results and discussion.....	87
5.2.1	X-ray diffraction studies.....	87
5.2.2	Diffuse reflectance UV-visible spectral studies.....	89
5.2.3	Scanning Electron Microscopic analysis.....	90
5.2.4	Mott-Schottky analysis.....	94
5.2.5	Photocatalytic degradation of <i>p</i> -chlorophenol studies.....	96
5.2.6	Chemical Oxygen Demand analysis.....	97
5.2.7	Photocatalytic water splitting studies.....	98
5.3	Conclusions.....	99

**CHAPTER 6 CHARACTERISATION AND CO OXIDATION ACTIVITY OF
Au/TiO₂**

6.1	Introduction.....	101
6.2	Results.....	106
6.2.1	X-ray diffraction studies.....	106
6.2.2	Inductively coupled plasma-optical emission spectroscopy studies....	109
6.2.3	Scanning Electron Microscopic studies.....	110
6.2.4	Transmission Electron Microscopic studies.....	113
6.2.5	Diffuse reflectance UV-visible spectra of samples prepared by sol deposition.....	118
6.2.6	Activity of samples prepared by sol deposition for the oxidation of CO.....	118

Table of contents (Contd.,)		Page No.
6.2.7	Activity of samples prepared by deposition precipitation for the oxidation of CO.....	120
6.3	Discussion.....	121
6.3.1	Explanation for the decrease in activity of brookite after calcination..	121
6.3.2	Explanation for the higher activity of brookite in DP method.....	127
6.4	Conclusions.....	132
CHAPTER 7 SUMMARY AND CONCLUSIONS		133
REFERENCES		137
LIST OF PUBLICATIONS		158

LIST OF TABLES

Table No.	Title	Page No.
1.1	Oxidation potentials of various oxidising species.....	4
1.2	Second order rate constants for ozone and hydroxyl radical for a variety of compounds.	5
1.3	Sources involved in the various Advanced Oxidation Processes	5
1.4	Properties and significance of gaseous air pollutants.....	24
1.5	Estimates of global CO sources and sinks.....	25
2.1	Methodology for the preparation of various TiO ₂ and carbon-TiO ₂ catalysts.....	33
3.1	Colourimetric estimation of Ce ⁴⁺ in the mixed oxides.....	55
3.2	Overall and net photocatalytic decrease in concentration (photocatalytic) of methylene blue under UV and Visible irradiation after 90 min.....	57
3.3	Amount of methylene blue adsorbed in dark after 90 min of stirring and methylene blue desorbed from used catalyst using DMSO.....	58
3.4	Bandgap, conduction and valence band energy positions of various oxides	61
4.1	Photocatalytic activity and carbon content of the carbon-TiO ₂ samples from TiCl ₃ after 90 min irradiation.....	81
4.2	Photocatalytic activity and carbon content of the carbon-TiO ₂ samples from P25 TiO ₂ after 90 min irradiation.....	82
5.1	Percentage decrease in concentration of <i>p</i> -chlorophenol using cadmium stannates as photocatalyst estimated by UV-Visible spectrophotometry and COD analysis.....	97
6.1	Surface area and crystalline phase composition of the various supports.....	107
6.2	Calculated and actual loading of gold by ICP analysis for the various Au/TiO ₂ samples.....	110
6.3	Average Au particle size from various sol derived Au/TiO ₂ samples	113
6.4	Ti-O bond distances of the various allotropic forms of TiO ₂	131

LIST OF FIGURES

Figure No.	Title	Page No.
1.1	Processes involved in semiconductor photocatalysis	11
1.2	Fate of photo-excited electrons and holes in a semiconductor particle.....	12
1.3	Formation of depletion, accumulation layers and flat band in an n-type semiconductor.....	14
1.4	Effect of varying the applied potential (E) on the band edges in the interior of an n-type semiconductor. a) $E > E_{fb}$, b) $E = E_{fb}$, c) $E < E_{fb}$	16
1.5	Various types of semiconductors based on their band potentials.....	18
1.6	Band positions of various semiconductor photocatalysts.....	19
3.1	XRD patterns of (a) CeO_2 (b) 9 % CeO_2-TiO_2 (c) 5 % CeO_2-TiO_2 (d) 3 % CeO_2-TiO_2 (e) 2 % CeO_2-TiO_2 (f) 1 % CeO_2-TiO_2 (g) 0.5 % CeO_2-TiO_2 (h) 0.25 % CeO_2-TiO_2 (i) TiO_2	50
3.2	XRD patterns of the samples scanned at a slow rate (0.25 degree per min).....	51
3.3	UV-Visible absorption spectrum of the CeO_2 modified TiO_2 photocatalysts	52
3.4	TEM images of 3 % CeO_2 modified TiO_2	53
3.5	SEM images of 3 % CeO_2 modified TiO_2	54
3.6	Structure of methylene blue	58
4.1	XRD patterns of TiO_2 and carbon- TiO_2 samples calcined at different temperatures.....	69
4.2	XRD pattern of carbon- TiO_2 from sucrose and P25 TiO_2 (SDA370) calcined at 643 K.....	70
4.3	Raman spectra of carbon prepared from sucrose and carbon- TiO_2 from sucrose and $TiCl_3$ (STA30N66).....	72
4.4	SEM images of carbon- TiO_2 (STA30N66)	73
4.5	SEM images of carbon-P25 TiO_2 (SDA370).....	74
4.6	TEM images of carbon- TiO_2 (STA30N66)	76
4.7	TEM images of carbon-P25 TiO_2 (SDA370).....	77

List of figures (Contd.,)	Page No.
4.8 Diffuse reflectance UV-visible spectra of carbon-TiO ₂ from TiCl ₃	79
4.9 Diffuse reflectance UV-visible spectra of carbon-P25 TiO ₂ samples	79
5.1 X-ray diffraction patterns of CdSnO ₃ before and after using for photocatalytic degradation of <i>p</i> -chlorophenol reaction under UV-visible irradiation	88
5.2 X-ray diffraction patterns of Cd ₂ SnO ₄ before and after using for photocatalytic degradation of <i>p</i> -chlorophenol reaction under UV-visible irradiation.....	88
5.3 Diffuse reflectance UV-visible spectra of CdSnO ₃ before and after using for photocatalytic degradation of <i>p</i> -chlorophenol reaction under UV-visible irradiation.	90
5.4 Diffuse reflectance UV-visible spectra of Cd ₂ SnO ₄ before and after using for photocatalytic degradation of <i>p</i> -chlorophenol reaction under UV-visible irradiation	91
5.5 SEM images of rhombohedral CdSnO ₃ (A) 1000 magnification and (B) 5000 magnification.....	92
5.6 SEM images of orthorhombic Cd ₂ SnO ₄ (A) 5000 magnification and (B) 10000 magnification.....	93
5.7 Equivalent circuit used for curve fitting of CdSnO ₃ and Cd ₂ SnO ₄	94
5.8 Mott-Schottky plot of rhombohedral CdSnO ₃ film coated on Ti sheets measured in 0.5 M Na ₂ SO ₄ (pH 7.0) electrolyte under dark conditions in the frequency range of 10 ⁻² to 10 ⁵ Hz with amplitude of 5 mV.....	95
5.9 Mott-Schottky plot of orthorhombic Cd ₂ SnO ₄ film coated on Ti sheets measured in 0.5 M Na ₂ SO ₄ (pH 7.0) electrolyte under dark conditions in the frequency range of 10 ⁻² to 10 ⁵ Hz with amplitude of 5 mV.....	96
6.1 XRD patterns of BRT4 and BRT3 samples.....	108
6.2 XRD patterns of Au/BRT4 catalysts before and after catalytic measurements.....	108
6.3 XRD patterns of Au/P25 catalysts before and after catalytic measurements	109

List of figures (Contd.,)	Page No.
6.4 SEM images of Au/TiO ₂ catalysts prepared by sol method (a) Au/BRT4- fresh and (b) Au/BRT4-after reaction.....	111
6.5 SEM images of Au/TiO ₂ catalysts prepared by sol method (a) Au/P25-fresh and (b) Au/P25- after reaction.....	112
6.6 TEM images of Au/BRT4 samples prepared by sol method (A) fresh and (B) after reaction.....	114
6.7 TEM images of Au/P25 samples prepared by sol method (a) fresh and (b) after reaction.....	115
6.8 Au particle size distribution in Au/BRT4 catalysts prepared by sol method (a) fresh (b) after reaction	116
6.9 Au particle size distribution in the various Au/P25 catalysts prepared by sol method (a) fresh and (b) after reaction	117
6.10 Diffuse reflectance UV-Visible spectra of sol derived Au/TiO ₂ samples	118
6.11 CO oxidation activity of various Au/TiO ₂ samples prepared by sol method before and after calcination in O ₂	119
6.12 CO oxidation activity of various Au/TiO ₂ samples prepared by DP method before and after reduction in H ₂	120
6.13 TEM images of Au/BRT4 prepared by sol method (a) before and (b) after catalytic measurements	124

LIST OF SCHEMES

Scheme No.	Title	Page No.
3.1	Coupled semiconductor mechanism in Ce modified TiO_2 leading to visible light activity.....	63
5.1	Schematic diagram of band positions (vs. NHE) of CdSnO_3 and Cd_2SnO_4 with respect to hydrogen and oxygen evolution potentials	99

ABBREVIATIONS

AR	-	Analytical Reagent
IR	-	Infrared Spectroscopy
ppm	-	parts per million
SEM	-	Scanning electron microscopy
TG	-	Thermogravimetry
TEM	-	Transmission Electron Microscopic
UV-Vis	-	Ultraviolet-Visible
XRD	-	X-ray Diffraction
DOS	-	Density of States
COD	-	Chemical Oxygen Demand
FAS	-	Ferrous Ammonium Sulphate
IE	-	Ionisation Energy
EA	-	Electron Affinity
DMSO	-	Dimethyl sulphoxide
LUMO	-	Lowest Unoccupied Molecular Orbital
HOMO	-	Higher Occupied Molecular Orbital
AOP	-	Advanced Oxidation Process
NHE	-	Normal Hydrogen Electrode
AVS	-	Absolute Vacuum Scale
CB	-	Conduction Band
VB	-	Valence Band
MB	-	Methylene blue
ICP-OES	-	Inductively Coupled Plasma – Optical Emission Spectroscopy

NOTATIONS

eV	-	electron volt
m ² /g	-	Square meter per gram
K	-	Kelvin
g	-	Gram
Å	-	Angstrom
d	-	Interplanar spacing planar
λ	-	Wavelength
cm	-	Centimeter
nm	-	Nanometer
V	-	Volts
wt	-	Weight
kJ	-	Kilo Joule
h	-	Hour
θ	-	Bragg angle
v	-	Frequency
%	-	Percentage
°C	-	Degree Celsius
μmol	-	Micro mole
deg	-	degrees
Hz	-	Hertz
mL	-	milliliter
mmol	-	millimoles
Mt	-	metric ton
W	-	Watt
min	-	Minutes
mm	-	millimeter
χ	-	Electronegativity

CHAPTER 1

INTRODUCTION

1.1 POLLUTION

Over the last three decades there has been increasing global concern over the impact of environmental pollution on public health, and the suffering through various diseases. Various resources in our environment namely water, land and air have been continuously affected by pollution. Most of the diseases facing mankind today occur due to prolonged exposure to environmental pollution. However, most of the environment related diseases are not easily detected and may be acquired during childhood and become noticeable later in adulthood.

In addition, pollution leads to depletion of the ozone layer, global warming and climate change. Furthermore, various flora and fauna in the contaminated region are either threatened or made extinct by the pollution. Most polluted spots in the world include China, India, Peru and Russia (Block and Hanrahan, 2009). Indoor plus outdoor air pollution is the sixth-leading cause of death, causing over 2.4 million premature deaths worldwide (Murray and Lopez, 2002).

1.2 WATER POLLUTION

Water covers over two thirds of Earth's surface and less than a third is taken up by land. As population of Earth continues to grow, there is ever-increasing pressure on

the planet's land and water resources. Oceans, rivers, and other inland waters are being continuously polluted by human activities leading to a gradual decrease in the quality of water. Water pollution is mostly about the quantity of certain substances in water. If the concentration of a certain substance in water exceeds the specified limits, it is considered to be polluted. Water pollution has its impact on both surface water and ground water. Untreated sewage, industrial waste water, pesticides, fertilizers, heavy metals, radioactive waste, chemical wastes like polychlorinated phenols, dyes, oil and plastics are the major sources of water pollution. Water polluted by oil will devastate and affect the marine living organisms in the aqueous eco-system. Thus toxic species in water bodies indirectly enter our food chain through aquatic food.

1.3 METHODS OF WATER TREATMENT

Treatment of water involves three steps

- Primary treatment: Physical processes that remove non-homogenizable solids and homogenize the remaining effluent.
- Secondary treatment: Biological processes that remove most of the Biological Oxygen Demand (BOD).
- Tertiary treatment: Physical, biological, and chemical processes to remove nutrients like phosphorus and inorganic pollutants like heavy metals. To decolourise organic pollutants presence in effluent water, and to carry out further oxidation.

In order for the treated water to be discharged into a water body, it should be free from various soluble organic and inorganic species. These species cannot be removed

by the primary and secondary treatments of water. Primary and secondary treatments are part of conventional wastewater treatment plants. However, secondary treatment plant effluents are still significantly polluted with some BOD. Neither primary nor secondary treatment is effective in entirely removing phosphorus and other large organic compounds or toxic substances. Hence tertiary treatment is necessary to completely decontaminate the waters. Various tertiary treatment methods are aerobic oxidation, super-chlorination, reverse osmosis, ultra filtration, UV treatment and Advanced Oxidation Processes (AOPs).

1.4 ADVANCED OXIDATION PROCESSES

Methods which utilize hydroxyl radicals for carrying out the oxidation of the pollutants are grouped as Advanced Oxidation Processes. Irrespective of the method of generation of hydroxyl radicals, these processes are called Advanced Oxidation Processes. OH radicals are extraordinarily reactive species and have one of the highest oxidation potentials (Table 1.1). Hydroxyl radicals are known to attack the most part of organic molecules with rate constant values of the order of 10^6 – 10^9 $M^{-1} s^{-1}$ (Andreozzi *et al.*, 1999; Farhataziz and Ross, 1977; Hoigne and Bader, 1983) (Table 1.2). In addition, hydroxyl radicals have very little selectivity of the position of attack in a molecule, which is a useful aspect for an oxidant used in wastewater treatment. The fact that the production of OH radicals can be made by a variety of methods adds to the versatility of Advanced Oxidation Processes, thus allowing a better compliance with the specific treatment requirements. An important consideration to be made in the application of AOP to waste water treatments is the requirement of expensive reactants like H_2O_2 and/or O_3 . Hence, the Advanced Oxidation Processes cannot replace the application of more economic treatments such

as the biological degradation whenever possible. A list of the different possibilities offered by AOP is given in Table 1.3.

Table 1.1. Oxidation potentials of various oxidising species

Oxidant	Oxidation potential, V
Fluorine	3.0
Hydroxyl radical	2.8
Ozone	2.1
Hydrogen peroxide	1.8
Potassium permanganate	1.7
Chlorine dioxide	1.5
Chlorine	1.4

Hence, the exploitation of Advanced Oxidation Processes should be by using it for oxidation decomposition of toxic substances after the biological treatment methods. Another aspect to be considered during the application of Advanced Oxidation Processes is the amount of Chemical Oxygen Demand (COD) in the water to be treated. Only wastes with relatively small COD contents (<5.0 g/L) can be suitably treated by means of these techniques since higher COD contents would require the consumption of large amounts of expensive reactants. Wet oxidation or incineration can be conveniently used to treat wastes with more pollutant contents. (Mishra *et al.*, 1995) and this way be followed by AOPs for further removal of the pollutants present at low concentration/trace levels.

Table 1.2. Second order rate constants for ozone and hydroxyl radical for a variety of compounds (Andreozzi *et al.*, 1999)

Organic compound	Rate constant ($M^{-1} s^{-1}$)	
	O_3^a	$HO^{\bullet b}$
Benzene	2	7.8×10^9
n-Butanol	0.6	4.6×10^9
t-Butanol	0.03	0.4×10^9
Chlorobenzene	0.75	4×10^9
Tetrachloroethylene	<0.1	1.7×10^9
Toluene	14	7.8×10^9
Trichloroethylene	17	4×10^9

a – From Hoigne and Bader, 1983 b – From Farhataziz and Ross, 1977.

Table 1.3. Sources involved in the various Advanced Oxidation Processes

Sources of oxidants	Name of the process
H_2O_2/Fe^{2+}	Fenton
H_2O_2/Fe^{3+}	Fenton-like
$H_2O_2/Fe^{2+}(Fe^{3+})/UV$	Photo assisted Fenton
H_2O_2/Fe^{3+} -oxalate	NA
Mn^{2+} /Oxalic acid/Ozone	NA
$TiO_2/h\nu/O_2$	Photocatalysis
O_3/H_2O_2	NA
O_3/UV	Photo assisted oxidation
H_2O_2/UV	Photo assisted oxidation

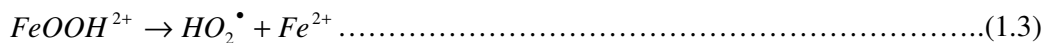
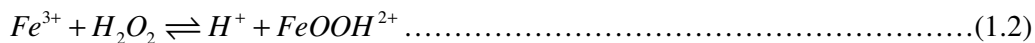
NA- Not applicable

1.4.1 Fenton processes

This process involving Fe^{2+} ions and H_2O_2 was discovered by Fenton in the 19th century (Fenton, 1894). However, its application for the oxidation of pollutants in water started only later in the 1960s. Currently, the application of Fenton's reagent to destroy toxic compounds such as phenols and herbicides in waste water is well known. In the Fenton process, the addition of H_2O_2 to Fe^{2+} salts generates the hydroxyl radicals (Haber and Weiss, 1934).

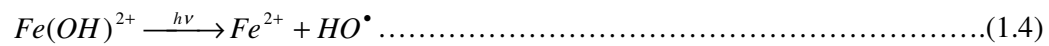


Neither special reactants nor special apparatus are required for this simple way of producing OH radicals. Since iron is abundant as well as non toxic element and also as the hydrogen peroxide is easy to handle and environmentally safe, this is an attractive oxidative system for waste water treatment. On the basis of the single reaction, the behaviour of the Fenton system cannot be completely explained (Equation 1.1). In fact, as pointed out in recent studies (Pignatello, 1992) the adoption of a proper value of pH (2.7–2.8) can result in the reduction of Fe^{3+} to Fe^{2+} (Equations 1.2 and 1.3) proceeding at an appreciable rate. Under these conditions, iron can be considered as the real catalyst.



1.4.2 Photo assisted Fenton processes

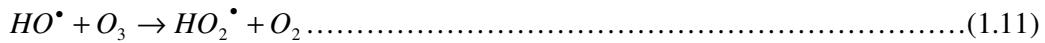
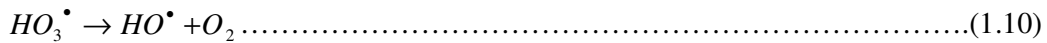
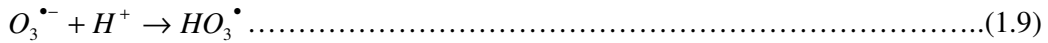
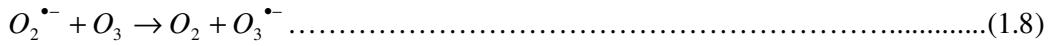
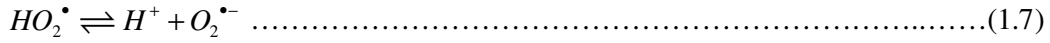
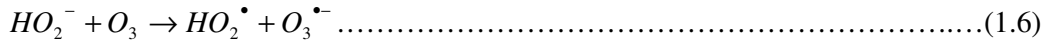
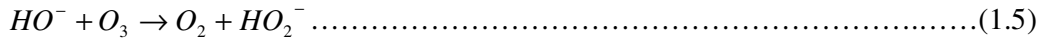
When irradiated by UV-Visible light, the rate of degradation of organic pollutant with Fenton and Fenton-like reagents is strongly accelerated (Kiwi *et al.*, 1993; Pulgarin and Kiwi, 1996). Irradiation with UV-Visible light of wavelength values higher than 300 nm was found to accelerate the Fenton oxidation reactions. On UV-Visible irradiation Fe^{3+} generated from the Fe^{2+} ions were reduced back to the ferrous ions (Equation 1.4) and the Fenton reaction continues due to the presence of H_2O_2 (Equation 1.1).



Despite the great deal of work devoted by researchers to these processes, there are very little industrial applications. This is for the reason that the applications of Fenton processes require strict pH control.

1.4.3 Ozonisation process

In order to understand the functioning of the O_3/H_2O_2 , a look in to the ozone chemistry in aqueous alkaline solutions is required. Hoigne (1998) has comprehensively and successfully studied this mechanism in order to give a chemical reasoning to the short life time of ozone in alkaline solutions. He showed that the decomposition of ozone in aqueous solution takes place through the formation of OH radicals. OH ion function as an initiator in the reaction mechanism (equations 1.5-1.11):



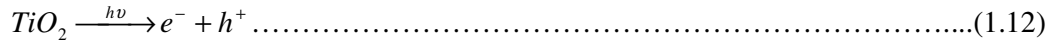
In an alkaline solution hydrogen peroxide exists as HO_2^- . As can be seen from equation 1.6 HO_2^- plays a significant role in the ozone decomposition. Hence, addition of HO_2^- into a solution containing ozone will facilitate the decomposition of O_3 and the simultaneous formation of hydroxyl radicals. In addition, the involvement of HO_2^- demonstrates the role played by pH in the formation of hydroxyl radicals from ozone. Hence an increase of pH and the addition of H_2O_2 to the aqueous O_3 solution will result in higher rates of OH radicals production and the attainment of higher steady-state concentrations of OH radicals in the radical chain decomposition process (Glaze and Kang, 1989).

1.4.4 Photocatalysis

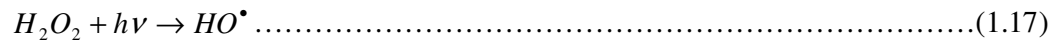
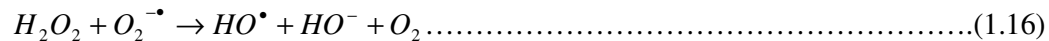
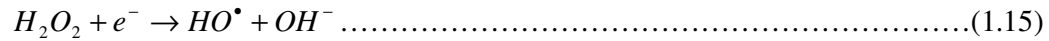
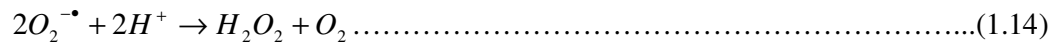
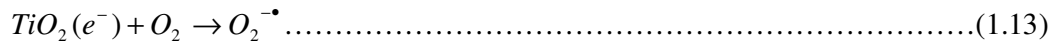
In the photocatalytic processes, semiconductors function as the catalyst and oxygen is used as the oxidizing agent (Ollis and Al-Ekabi, 1993). Among the many catalysts tested so far, only the anatase phase of TiO_2 seems to have the most of the desired

attributes such as high stability, good performance and low cost (Rajeshwar, 1995).

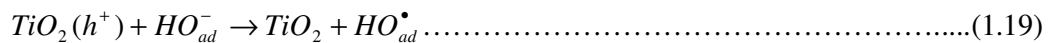
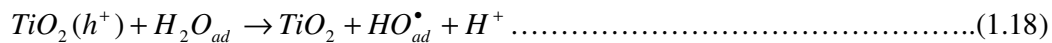
The photocatalytic process are initiated by the absorption of the radiation by the semiconductor leading to the formation of electron-hole pairs (Equation 1.12)



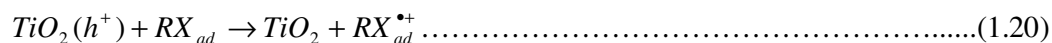
The photogenerated electrons have enough potential to reduce some metals and dissolved oxygen leading to the formation of the superoxide radical ion, $O_2^{\bullet -}$. Even though, superoxide radical ions can oxidize organic compounds, their contribution to the overall oxidization process is very small. Superoxide radical ions further react in different ways leading to the formation hydroxyl radicals (Fujishima *et al.*, 2008) (Equations 1.13-1.17).



On the other hand, the holes are capable of oxidizing adsorbed H_2O or HO^- to reactive HO radicals (Equations 1.18 and 1.19):



These reactions are important in the oxidative degradation processes due to the high concentration of adsorbed H₂O and HO⁻ on the particle surface. Direct oxidation of some of the substrates adsorbed on the semiconductor surface also takes place (equation 1.20):



1.5 PHOTOCATALYSIS

Among the three AOPs mentioned, photocatalysis is the most promising method. This is attributed to its potential to utilize energy from the sun without the addition of other forms of energy or reagents. Photoelectrochemistry involves compounds having an energy gap between the highest occupied molecular orbital (HOMO) or valence band and the lowest unoccupied molecular orbital (LUMO) or conduction band. The condition for a compound to be able to get activated by light is that the energy gap between LUMO and HOMO should be equal to that of the energy of the light used. The reactions carried out by the photocatalysts are classified into two categories namely homogeneous and heterogeneous photocatalysis.

1.5.1 Heterogeneous photocatalysis

Heterogeneous catalysis is based on the semiconductors which are used for carrying out various desired reactions in both liquid and vapour phase. Photocatalysis involve the excitation of electrons from the valence band to the conduction band on exposing

the catalyst to the radiation. This leads to the formation of highly reactive electrons and holes in the conduction band and valence band respectively (Fig. 1.1). The electrons are capable of carrying out reduction reactions and holes can carry out oxidation reactions. Various processes involved in semiconductor photocatalysis are shown in Fig. 1.2. The electrons and holes move to the surface of the photocatalyst and are trapped there. The trapped electron and hole react with acceptor (step c) or donor molecules (step d), respectively, or recombine at surface trapping sites (step a). The electron and hole can also be trapped at bulk trapping sites and recombine there with the release of heat (b).

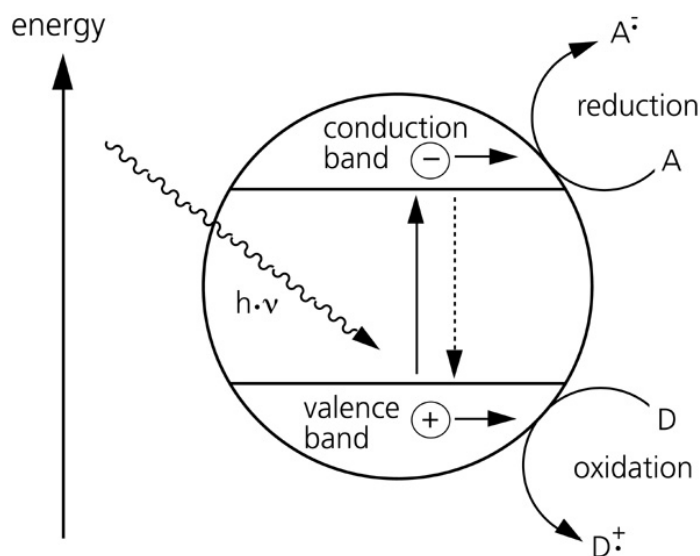
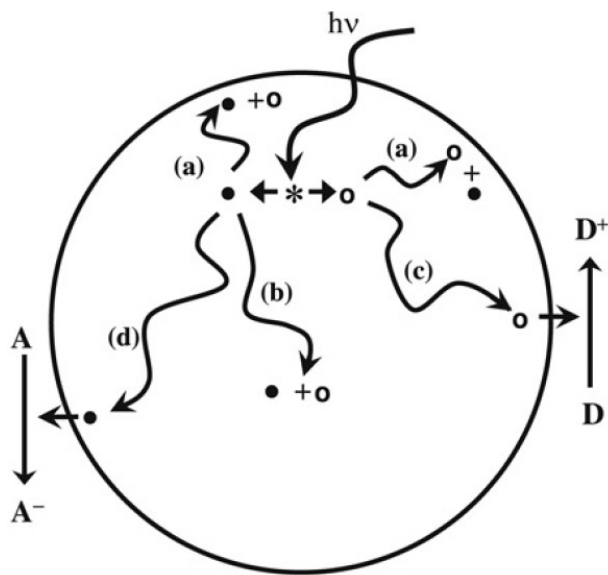


Fig. 1.1. Processes involved in semiconductor photocatalysis

These electrons and holes can be exploited by a variety of means as given below:

- (i) for producing electricity (solar cells) – photovoltaics
- (ii) for decomposing or removing pollutants - photooxidation
- (iii) for the synthesis and production of useful chemicals - photocatalysis
- (iv) for the photo electrolysis of water to produce H_2 - photoelectrochemistry



• = electron; o = hole

Fig 1.2. Fate of photo-excited electrons and holes in a semiconductor particle (Fujishima *et al.*, 2008)

1.5.2 Charge carrier trapping

The recombination of excited electron-hole pair should be minimized for efficient charge transfer reaction between semiconductor and adsorbed species. Trapping the excited electron by surface states increases the lifetime of the excited electron. As a result, the direct recombination of electron-hole pairs is reduced. In the case of nanocrystalline TiO₂ films, the recombination can be delayed, with a lifetime on the scale of microsecond (μs) (Peiro *et al.*, 2006; Yoshihara *et al.*, 2004). The recombination process is competing with the slow charge transfer of electrons to molecular oxygen. In order to trace the trapped electrons and holes in the nanoparticles of TiO₂ after irradiation, electron paramagnetic resonance (EPR) technique is commonly used (Howe and Gratzel, 1985; Hurum *et al.*, 2003). Trapped electrons can be detected in the form of Ti³⁺ at low temperatures. Upon adsorption of

O₂ at the surface of TiO₂, the Ti³⁺ EPR signals were found to be removed. In addition, trapped holes are also observed and are considered to be localized as deep trap states. Even though, much of the photogenerated holes are trapped in deep or shallow trapping sites, a large portion of the photo-excited electrons exist in a nearly free, untrapped state in the interior of the TiO₂ particle (Yamakata *et al.*, 2005). EPR and IR studies Berger *et al.*, (2005) have found that a major fraction (greater than 90%) of photo-excited electrons remained in the conduction band and were silent in EPR spectra under high-vacuum conditions, even at the low temperature of 90 K,.

1.5.3 Semiconductor-electrolyte interface

At the interface between a semiconductor and an electrolyte solution, a variety of situations exist. In order for the two phases to be in equilibrium, the electrochemical potential of the two phases must be the same. The redox potential of the electrolyte solution determines the electrochemical potential of the solution and the redox potential of the semiconductor is determined by the Fermi level. If the redox potential of the solution and the Fermi level were not at equal energy, a movement of charge between the semiconductor and the solution is essential in order to equilibrate the two phases. Unlike a metallic electrode, the excess charge that is now located on the semiconductor, does not lay at the surface. The excess charge extends into the electrode for a significant distance (10-1000 nm). This region is referred to as the space charge region, and has an associated electrical field. Consequently, there exist two double layers: the interfacial (electrode/electrolyte) double layer, and the space charge double layer.

In the case of an n -type semiconductor electrode at open circuit, the Fermi level is in general higher than the redox potential of the electrolyte. Hence, transfer of electrons will take place from the electrode into the solution. As a result, the space charge region has a positive charge which results in an upward bending of the band edges. This region is referred to as a depletion layer, as majority of the charge carriers of the semiconductor are removed from this region, (Fig. 1.3). In the case of a p -type semiconductor, the Fermi level is normally lower in energy than the redox potential of the solution. This will result in flow of electrons from the solution to the electrode to attain equilibrium. This leads to the formation of a negative charge in the space charge region, resulting in a downward bending in the band edges. This is again called a depletion layer, as the holes in the space charge region are removed by this process.

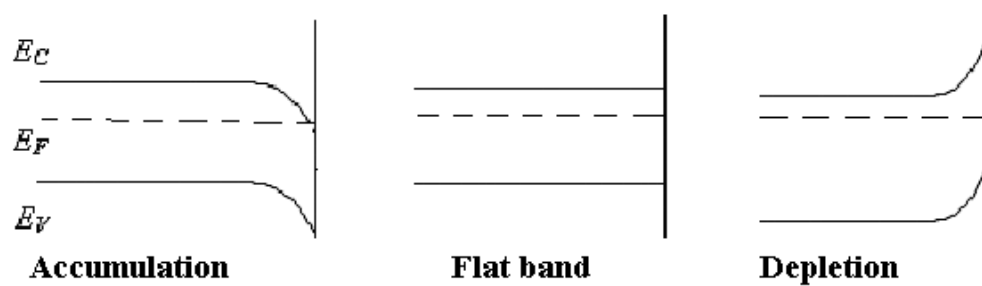


Fig. 1.3. Formation of depletion, accumulation layers and flat band in an n -type semiconductor

For metallic electrodes, changing the potential applied to the electrode shifts the Fermi level. In the case of semiconductor, the band edges in the interior (i.e., away from the depletion region) also vary with the applied potential in the same way as that of the Fermi level. However, the changes in the applied potential will not affect the energies of the band edges at the interface. Therefore, on moving from the interior of

the semiconductor to the interface, a change in the energies of the band edges is observed. Hence, the variation in the applied potential will vary the magnitude and direction of band bending. Three different situations were possible (Bott, 1998) (Fig. 1.4):

a) The Fermi energy and the redox potential of the solution lies at the same energy at certain applied potential. There is no band bending as there is no net transfer of charge (Fig 1.4b). Hence, this potential is called as the flatband potential, E_{fb} .

b) At potentials positive of the flatband potential, depletion regions occur for an *n*-type semiconductor. For a *p*-type semiconductor, depletion regions occur at potentials negative of the flatband potential (Fig. 1.4a).

c) In the case of *n*-type semiconductor, at potentials negative of the flatband potential, there is an excess of electrons in the space charge region, and hence denoted as an accumulation region (Fig. 1.4c). In the case of a *p*-type, an accumulation region arises at potentials more positive than the flatband potential.

For a semiconductor, the ability to transfer charge depends on whether there is an accumulation layer or a depletion layer. The semiconductor electrode behaves similar to a metallic electrode, if there is an accumulation layer. This is because, there is an excess of the majority of charge carriers available for charge transfer. On the other hand, if there is a depletion layer, then there are only a small amount of charge carriers available for transfer. Hence, if at all electron transfer reactions take place, will occur slowly.

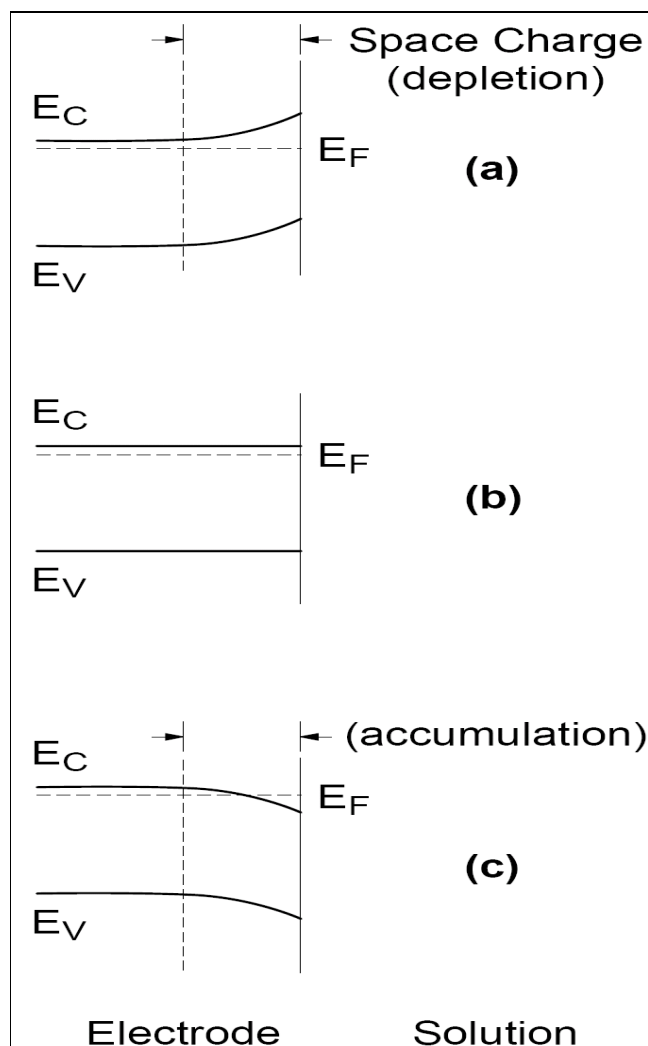


Fig. 1.4. Effect of varying the applied potential (E) on the band edges in the interior of an n -type semiconductor. a) $E > E_{fb}$, b) $E = E_{fb}$, c) $E < E_{fb}$

1.5.4 Effect of electron-hole recombination

Electron-hole recombination plays a major negative role in photocatalysis, as no chemical reactions take place if the photogenerated electron and hole pairs recombine instead of reacting with the substrates adsorbed on the surface. Unlike the measurement of the rate of reaction of the electrons and holes, measuring the rate of

recombination directly is not easy. The crystallinity of the semiconductor plays a major role in the extent of recombination (Kaneco and Okura, 2002). It was found that the recombination takes place at the surface defects (Landsberg, 1991). Recombination takes place mostly at the surface where the crystal is terminated thereby the larger the surface area, the faster the recombination. It was found that amorphous TiO₂ was found to have a higher recombination rate than the crystalline TiO₂. Despite the fact that both forms of TiO₂ are thermodynamically capable of reducing O₂, rutile possesses lower photocatalytic activity (higher electron-hole recombination) than anatase because of its lower capacity to adsorb O₂ (Serpone and Pelizzetti, 1989).

1.5.5 Importance of position of energy levels

The ability of a photocatalyst to carry out a particular reaction depends on the position of the energy levels of the catalyst as well as the substrate. For a compound to be able to carry out the reduction reaction, the potential of conduction band or LUMO should be more negative than that of the potential required for the reduction reaction. For a compound to be able to carry out the oxidation reaction the potential of the valence band or the HOMO should be more positive than the potential required for the oxidation reaction. Let us consider the reaction of the photocatalytic splitting of water as an example. The following are the two reactions involved.



The oxidation reaction leading to oxygen evolution mentioned in equation (1.22) will take place at a potential +1.23 V (NHE) where as the reduction reaction leading to the hydrogen evolution will take place at 0.00 V (NHE). The reduction reaction mentioned in equation (1.21) will happen only if the potential of conduction band of photocatalyst is more negative than 0.00 V. Likewise the oxidation reaction mentioned in equation (1.22) will happen only if the potential of the valence band of the photocatalyst is more positive than +1.23 V. Accordingly, depending on the positions of CB and VB, the systems can be classified as OR type (both reactions possible), O type (only oxidation is feasible), R type (only reduction is feasible) and X type (neither reactions can occur) (Fig. 1.5).

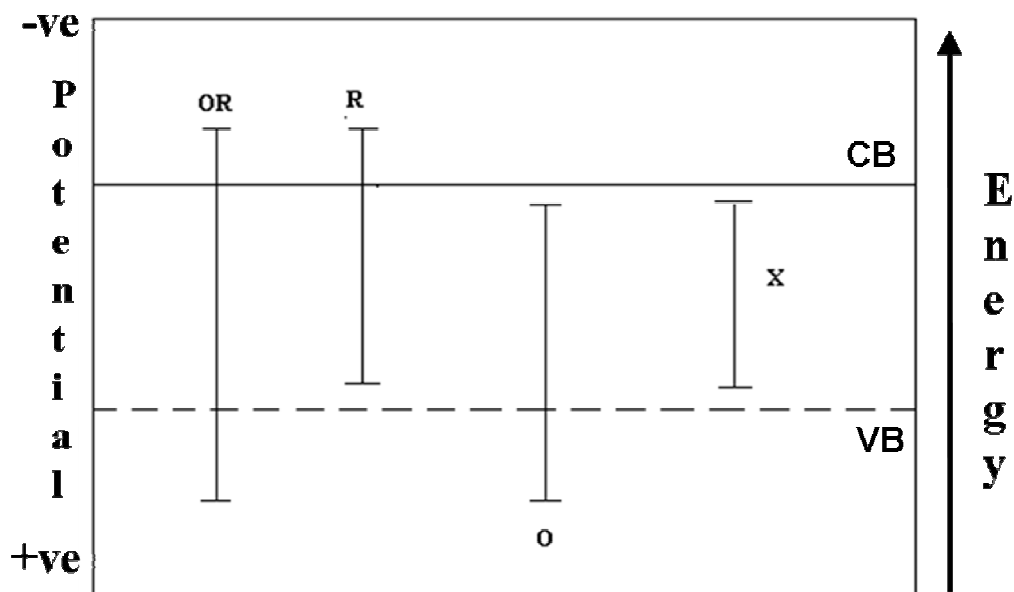


Fig. 1.5. Various types of semiconductors based on their band potentials

1.5.6 Choice of the photocatalyst

The band position and bandgap of selected semiconductor photocatalysts are shown in Fig. 1.6. Among them, WO_3 and Fe_2O_3 cannot carry out the photosplitting of water since their conduction band potentials are less negative than the hydrogen evolution potential. All the given catalysts can carry out the oxygen evolution reaction. However among all of them, only a few were studied for water splitting reaction because of other problems like photo corrosion, cost, higher bandgap and stability.

Another important parameter to be taken into account while choosing the photocatalyst is the percentage of ionic character of the cation-anion bond. A system which has higher percentage ionic character ($> 40\%$) will have higher band gap and

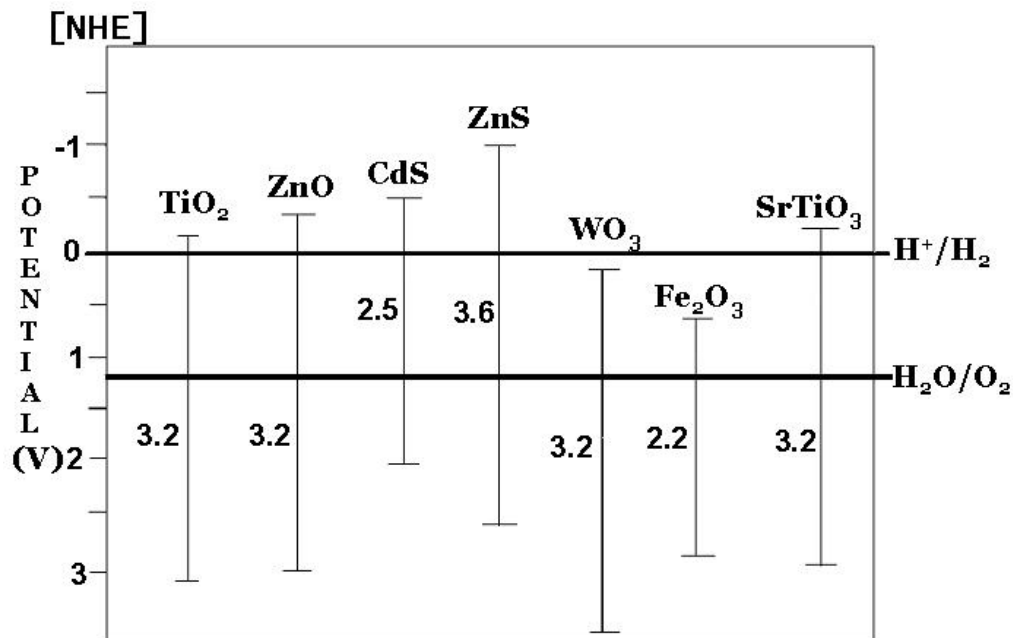


Fig 1.6. Band positions of various semiconductor photocatalysts

will not be able to absorb light in the visible region. A catalyst which has a percentage ionic character between 20-30 % with suitable positions of the valence and conduction band potentials with respect to the reaction under consideration will be successful for carrying out the reaction (Viswanathan, 2003). It is important to mention that the commercial success of a photocatalyst depends on its ability to function by utilizing the visible light. This is because of the composition of sunlight which has 46 % visible radiation, 47 % IR radiation and only 7 % UV radiation. But TiO₂, which is the most efficient and stable photocatalyst available, can function only by using the UV light. Hence, research all over the world is focussed on finding a photocatalyst or modifying the available catalysts so that they can function by absorbing light in the visible region.

1.5.7 Visible light photocatalysis

Unlike photocatalysis in green plants, the titanium dioxide photocatalyst in itself does not allow the use of visible light and can make use of only 7 % of solar beams that reach the earth. To address these problems, photocatalytic systems which are able to operate effectively and efficiently not only under UV but also under the most environmentally ideal energy source, sunlight, must be developed. It is vital to design and develop unique TiO₂ photocatalysts which can absorb and operate with high efficiency under solar and/or visible light irradiation. These efforts include doping TiO₂ with metal impurities (Devi *et al.*, 2009 & 2010; Dvoranova *et al.*, 2002; Iwasaki *et al.*, 2000; Sayilkan, 2007; Valentin *et al.*, 2009; Wu *et al.*, 2009; Yu *et al.*, 2009; Zhou *et al.*, 2006), doping TiO₂ with anions (non-metal doping) (Nakamura *et al.*, 2004; Park *et al.*, 2006; Torres *et al.*, 2004), coupling TiO₂ with narrow band-gap semiconductors (Doong *et al.*, 2001; Gouvea *et al.*, 2000; Ho *et al.*, 2004; Ho and Yu,

2006; Huang *et al.*, 2009; Lo *et al.*, 2004; Miyauchi *et al.*, 2000; Parra *et al.*, 2003; Robert, 2007; Tada *et al.*, 2006) and preparing oxygen-deficient TiO₂ (Hossain *et al.*, 2007; Ihara *et al.*, 2001; Justicia *et al.*, 2002; Kikuchi *et al.*, 2006).

During the recent years, doping with non-metals has been widely studied. Studies were carried out with various non-metallic elements such as nitrogen (Asahi *et al.*, 2001; Irie *et al.*, 2003; Liu *et al.*, 2009a & b; Maeda and Watanabe, 2006; Sakthivel *et al.*, 2004; Sathish *et al.*, 2005 & 2007), sulphur (Dunnill *et al.*, 2009; Ho *et al.*, 2006; Izumi *et al.*, 2009; Ohno *et al.*, 2003 & 2004; Sathish *et al.*, 2009; Yu *et al.*, 2005), carbon (Huang *et al.*, 2008; Irie *et al.*, 2006; Sakthivel and Kisch, 2003; Xiao *et al.*, 2008; Yang *et al.*, 2008), fluorine (Li *et al.*, 2005; Pelaez *et al.*, 2009; Xu *et al.*, 2008; Yang *et al.*, 2010; Yu *et al.*, 2002), phosphorus (Li *et al.*, 2009; Lin *et al.*, 2005; Zheng *et al.*, 2008 & 2010) and boron (Chen *et al.*, 2006; Huang *et al.*, 2009; Liu *et al.*, 2008; Ochiai *et al.*, 2010; Zhao *et al.*, 2004). All these elements on doping showed a red shift in the absorption spectrum of TiO₂.

1.5.8 Importance of adsorption in heterogeneous photocatalysis

As the recombination of the photogenerated electron and hole occurs on a picosecond timescale, electron transfer at the interface can kinetically compete with recombination only when the donor or acceptor is adsorbed on the semiconductor before irradiation. Hence, adsorption of the substrate prior to irradiation is very important for efficiency of the heterogeneous photocatalytic process (Fox and Dulay, 1993). Hydroxyl groups or water molecules adsorbed on the surface can serve as traps for the photogenerated hole, leading to the formation of hydroxyl radicals, in the case of metal oxide suspensions. Strong adsorption of acetone and 2-propanol on ZnO

has been observed during temperature-programmed desorption (Fox *et al.*, 1982) and X-ray photoelectron spectroscopy (Munuera *et al.*, 1990). Metal oxide surfaces have a surface density of about 4-5 hydroxyl groups/nm². These surface hydroxyl groups have different sets of acidities (Pichat *et al.*, 1987; Yamanaka and Tanabe, 1975), as has been shown by the continuous distribution of adsorption energies in the Freundlich isotherm (Tunesi and Anderson, 1991). Many organic substrates were found to play the role of adsorbed traps for the photo-generated holes. For example, in a colloidal suspension of TiO₂ in acetonitrile, radical ions are detected directly during flash excitation (Fox *et al.*, 1982).

1.5.9 Alternatives to TiO₂ photocatalyst

In recent years an increasingly great number of new photocatalysts have been designed and tested as possible alternatives to TiO₂. These materials are not derived from TiO₂ by any of the usual modifications such as doping, coupling with an additional phase or morphological changes. Instead, they are completely different compounds with distinct composition and structure. Various tantalates (Kato *et al.*, 2003; Kato and Kudo, 2001; Osterloh, 2008) and niobates (Domen *et al.*, 1990; Ebina *et al.*, 2005) were found to be effective photocatalysts for water splitting. Oxides of bismuth like Bi₂W₂O₉, Bi₂WO₆, (Yoshimura *et al.*, 1993) Bi₂MoO₆, Bi₂Mo₂O₉, Bi₂Mo₃O₁₂ (Shimodaira., *et al.*, 2006) and oxides of Indium such as In₂O₃ (Kudo and Mikami, 1998), Ba₂In₂O₅ (Wang *et al.*, 2005), MIn₂O₄ (M = Ca, Sr) (Sato *et al.*, 2003) were found to be capable of photosplitting water. Tantalum nitride (Ta₃N₅) (Hitoki *et al.*, 2002), and Tanatalum oxynitrides (TaON) (Hitoki *et al.*, 2002) were also found to be effective catalysts for water splitting.

1.6 AIR POLLUTION

Air pollution, both indoor and outdoor has a profound impact on the health of people around the world. Short term problems due to air pollution are irritation to the eyes, nose and throat. Other symptoms are nausea, headache and allergic reaction. Long term exposure to air pollution causes diseases like lung cancer, respiratory diseases and bronchitis. Air pollution also aggravates existing problems like asthma. At higher concentrations various pollutants will lead to fatality. The properties and significance as air pollutants of various compounds are shown in Table 1.4.

1.6.1 Pollution caused by carbon monoxide

Carbon monoxide (CO), a very simple molecule consisting of a single carbon atom and a single oxygen atom, primarily enters the air we breathe as a gaseous by-product of the incomplete combustion of hydrocarbon fuels, such as gasoline and diesel. A properly maintained car emits about 191 kg of CO each year, while a Sports Utility Vehicle (SUV) emits about 248 kg over the same period. Older vehicles and those with malfunctioning emission-control systems can create more CO (DeCicco and Thomas, 1999). CO is a toxic gas that affects the transport of oxygen in the blood stream. In the atmosphere, the concentration of carbon monoxide is negligible. In conditions where there is restricted ventilation as that found in towns, inside a car or house, higher concentrations of CO can be a significant health hazard. The various sources and sinks of CO are listed in Table 1.5.

Table 1.4. Properties and significance of gaseous air pollutants

Pollutant	Properties of importance	Significance as air pollutant
Sulphur dioxide (SO ₂)	Colourless gas, intense acrid odour, forms H ₂ SO ₃ with water	Damage to vegetation, building materials, respiratory system and acid rain
Sulphur trioxide (SO ₃)	Soluble in water to form H ₂ SO ₄	Highly corrosive and acid rain
Hydrogen sulphide (H ₂ S)	Rotten egg odour at low concentrations, odourless at high concentrations	Extremely toxic
Nitrous oxide (N ₂ O)	Colourless; used as aerosol carrier gas	Relatively inert; not a combustion product
Nitric oxide (NO)	Colourless; sometimes used as anaesthetic	Produced during combustion and high-temperature oxidation; oxidizes in air to NO ₂
Nitrogen dioxide (NO ₂)	Brown or orange gas	Component of photochemical smog formation; toxic at high concentration and acid rain
Carbon monoxide (CO)	Colourless and odourless	Product of incomplete combustion; toxic at high concentration
Carbon dioxide (CO ₂)	Colourless and odourless	Product of complete combustion of organic compounds; implicated in global climate change
Ozone (O ₃)	Very reactive	Damage to vegetation and materials; produced in photochemical smog
Hydrocarbons (C _x H _y)	Many different compounds	Emitted from automobile crankcase and exhaust
Hydrogen fluoride (HF)	Colourless, acrid, very reactive	Product of aluminium smelting; causes reactive fluorosis in cattle; toxic

Table 1.5: Estimates of global CO sources and sinks (Colls, 2002)

Sources	Range of estimates (Mt CO / year)
Fossil fuel combustion/industry	300-550
Biomass burning	300-700
Vegetation	60-160
Oceans	20-200
Methane oxidation	400-1000
Oxidation of other hydrocarbons	200-600
<i>Total</i>	1800-2700
Sinks	Range of estimates (Mt CO / year)
Tropospheric oxidation by OH	1400-2600
Stratosphere	~100
Soil uptake	250-640
<i>Total</i>	2100-3000

1.7 CARBON MONOXIDE OXIDATION

Oxidation of CO requires a temperature of about 973 K in the absence of a catalyst. The rate-determining step is the thermal dissociation of oxygen molecule to O atom. The activation energy for this reaction was experimentally determined to be 167.5 kJ/mol. In the presence of noble metal catalysts like Pt or Pd, the dissociation of oxygen molecule occurs catalytically on the active sites (on the metal surface). Hence, the reaction of adsorbed CO with the adsorbed oxygen atoms becomes the rate determining step. The reaction takes place at 373 K and the activation energy is

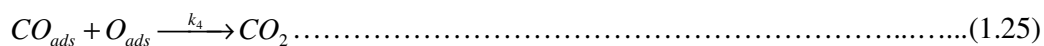
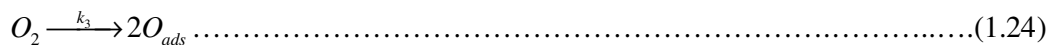
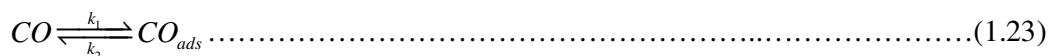
reduced to 83.7 kJ/mol in the presence of the catalyst. This is a significant reason why CO emission was considerably reduced from vehicles and power plants at moderate temperatures.

Various metal from the platinum group supported on alumina, that is Pt/Al₂O₃, Rh/Al₂O₃ and Ru/Al₂O₃ (Kahlich *et al.*, 1997; Oh and Sinkevitch, 1993), and zeolite-supported platinum catalysts (Pt/A-zeolite and Pt/mordenite) (Igarashi *et al.*, 1997), have been studied for this process. Among these, supported platinum catalysts gave the best results. Other than platinum, supported gold catalysts such as Au/Al₂O₃, Au/MnOx/MgO/Al₂O₃ (Bethke and Kung, 2000; Grisel and Nieuwenhuys, 2001), Au/MnOx (Sanchez *et al.*, 1997) and especially Au/ α -Fe₂O₃ (Kahlich *et al.*, 1999) were found to be very active for this process. Many papers report the use of supported metal catalysts for preferential CO oxidation in the presence of H₂. Other extensively studied noble metals are platinum, palladium, ruthenium and rhodium, supported on alumina or silica or on other supports such as zeolites or those based on ceria. Except the pioneer work of Brown *et al.*, (1960), papers on selective CO oxidation on noble metals started appearing in the 1990s. Oh and Sinkevitch (1993) have compared the catalytic performances of Pt, Pd, Rh and Ru supported on Al₂O₃.

1.7.1 Kinetics of oxidation of CO at low pressure

Kinetics of CO oxidation on Pt-group metals (Rh, Pt, Pd and Ru) at low pressures (<10⁻³ Torr) has been well-studied by using single crystal surfaces coupled with traditional ultrahigh vacuum surface science probes (Engel and Ertl, 1978 & 1979; McClure and Goodman, 2009). Pt, Rh, and Pd surfaces, in general, behave similarly. It is generally accepted that at low pressure conditions, CO oxidation takes place via a

Langmuir–Hinshelwood reaction mechanism, whereby co-adsorbed CO and O atoms react to form CO₂. This reaction scheme is shown below in Equations 23–25) (Engel and Ertl, 1979)



Adsorbed CO has been shown to inhibit adsorption of O₂ more effectively than inhibition of CO adsorption by oxygen adsorbed on the surface. (Engel and Ertl, 1978 & 1979; Jones *et al.*, 1999). Thus, at low temperatures, production of CO₂ is inhibited by adsorbed CO. At higher temperatures rate of CO₂ production increases due to increased rate of desorption of CO. Maximum CO₂ production rates occur at conditions where there is minimum coverage of CO on the surface (Engel and Ertl, 1978 & 1979; Jones *et al.*, 1999; Xu and Goodman, 1993).

1.7.2. Oxidation of CO by Au

Gold was usually considered to have very little use as a catalyst until the late 1980s. Chemical activities of gold, when present in the form of nanoparticles were reported during the 1970s (Bond *et al.*, (1973); McIntosh and Ozin, 1976). However, serious investigations were not carried out in spite of these results of catalytic activity of gold nanoparticles. It was only after Haruta *et al.*, (1989 & 1993) found that the gold particles deposited on selected metal oxides exhibit surprisingly high catalytic activity for CO oxidation even at 200 K, that studies on catalytic activity of gold became

extensive. Currently, literature describes the CO oxidation ability of gold nanoparticles supported on metal oxides such as TiO₂ (Date *et al.*, 2002; Grunwaldt and Baiker, 1999), Co₃O₄ (Haruta *et al.*, 1989), NiO (Haruta *et al.*, 1989), Fe₂O₃ (Bocuzzi *et al.*, 1999; Haruta *et al.*, 1989), Al₂O₃ (Costello *et al.*, 2002), SiO₂ (Overbury *et al.*, 2004) and ZrO₂ (Grunwaldt *et al.*, 1999). Au catalysts deposited on various supports show a wide variation in activity.

The properties of the oxides are responsible for most of the observed variation in activity of the Au catalysts on different supports. The point of zero charge for instance, affects the deposition of Au. The reducibility of the oxide support also affects the activity, as it affects the transfer of oxygen between the support and the Au nanoparticles. In order to have further understanding of the mechanism of catalysis of the gold nanoparticles supported on metal oxides, a study the effects of various phases of an oxide will be helpful. TiO₂ which exists in three different allotropic forms: anatase, brookite, and rutile, is a good candidate for such a study. So far, rutile (Remediakis *et al.*, 2005) and anatase (Bocuzzi *et al.*, 1999; Rodriguez *et al.*, 2002) have been extensively investigated as supports for gold nanoparticles in catalytic CO oxidation. The brookite phase of TiO₂ has only been studied in a few cases as support for Au towards catalytic CO oxidation reaction (Yan *et al.*, 2004 & 2005).

1.8 MOTIVATION AND SCOPE OF THE PRESENT WORK

Rare earth ions have been reported to induce a red shift in UV-visible spectrum of TiO₂ (Li *et al.*, 2005). The presence of Ce in TiO₂ has been reported to be consistently showing absorption in the visible region (Tong *et al.*, 2007). Because of its smaller bandgap CeO₂ is expected to induce activity in the visible light by a

coupled semiconductor mechanism. One of the ways of reducing the recombination is by increasing the availability of target molecules closer to the photocatalyst surface. This can be achieved by coating the surface of the photocatalyst with a good adsorbent like carbon. In addition, carbon is expected to increase the rate of the electron and hole transfer because of its conductivity (Oloman *et al.*, 1991). Materials containing elements with completely filled *d*-orbitals (d^{10}) have VB edge at higher energy and hence smaller bandgap (Sato *et al.*, 2001). As both cadmium and tin have d^{10} configuration in their outer orbitals, oxides based on them are expected to be visible light active photocatalysts.

Most of the CO oxidation studies were carried out using anatase and rutile phases of TiO_2 as supports for Au and the results indicate that anatase is a better support than rutile. CO oxidation reactions using brookite TiO_2 as support for gold have not been carried out extensively so far (Ho and Yeung, 2007). Yan *et al* (2005) have recently reported that the brookite phase is more active towards CO oxidation than anatase and rutile forms of TiO_2 . In addition, the brookite as support is described to be more stable at higher temperatures than anatase and rutile forms of TiO_2 .

The main focus of this thesis is on the following aspects

- Preparation of CeO_2 modified TiO_2 catalysts with various loadings of CeO_2 and to study their visible light photocatalytic activity towards methylene blue degradation.
- Preparation of carbon- TiO_2 composites by two different strategies and to compare their photocatalytic activities for the degradation of methylene blue.

- Preparation of CdSnO_3 and Cd_2SnO_4 and to study their photocatalytic activity towards degradation of *p*-chlorophenol under UV-Visible and Visible light irradiations.
- Determination of band potentials of CdSnO_3 and Cd_2SnO_4 by electrochemical impedance measurements and to study the ability of these systems to evolve hydrogen from water
- Loading of Au on TiO_2 by sol-deposition and deposition-precipitation methods and to study the influence of the method of loading on the CO oxidation activity
- Loading of Au on different phases of TiO_2 and to study the influence of TiO_2 phase on the CO oxidation activity.

CHAPTER – 2

EXPERIMENTAL METHODOLOGY

2.1 CHEMICALS AND MATERIALS USED

Titanium (IV) isopropoxide (97%) and Chloroauric acid (HAuCl_4) (AR grade) were obtained from Sigma-Aldrich India Ltd. Ammonium ceric nitrate (99.0 %) and *p*-chlorophenol (> 99.5 %) were obtained from SD fine chemicals, India. Commercial TiO_2 (P25) was obtained from Degussa, Germany. 15 % TiCl_3 solution (AR grade) was obtained from Loba Chimie, India. Sucrose, $3\text{CdSO}_4 \cdot 8\text{H}_2\text{O}$ and TiCl_4 solution (AR grade) were obtained from Merck India Ltd. $\text{SnCl}_4 \cdot 5\text{H}_2\text{O}$ (AR grade) was obtained from CDH Chemicals, India. All other chemicals used in the investigations were of analytical (AR) grade and were obtained from Qualigens, India or S.D. Fine Chemicals, India.

2.2 PREPARATION OF THE CATALYST

2.2.1 Preparation of CeO_2 modified TiO_2

Nanoparticles of Ce modified TiO_2 were synthesized in an aqueous solution of 0.01 % polyacrylamide (M. Wt. 5×10^6). pH of the aqueous solution of polyacrylamide was adjusted to 12.7 using aqueous ammonia. Titanium (IV) isopropoxide and ammonium ceric nitrate were taken as the source of titanium and cerium respectively. Titanium (IV) isopropoxide dissolved in dichloromethane and ammonium ceric nitrate dissolved in double distilled water were added drop wise to the polyacrylamide solution at the rate of 1.5 mL per min and 0.5 mL per min respectively under

conditions of vigorous stirring. The obtained gel was stirred for 12 h and then washed 3 times with double distilled water. It was then dried at 343 K and calcined in air for 6 h at 873 K. Various Ce loadings such as 0.25 % (1 g catalyst = 0.025 g CeO₂ + 0.975 g TiO₂), 0.5 %, 1.0 %, 2.0 %, 3.0 %, 5.0 % and 9.0 % were prepared. Pure CeO₂ and TiO₂ were also prepared by precipitating only ammonium ceric nitrate and titanium (IV) isopropoxide, respectively under similar experimental conditions as those adopted for Ce modified TiO₂ preparation.

2.2.2 Preparation of carbon-TiO₂ composites

Carbon-TiO₂ composites were prepared by using sucrose and TiCl₃ as the sources for carbon and TiO₂ respectively. To the aqueous solution of sucrose, TiCl₃ solution was added and stirred until a homogeneous solution was obtained. The obtained solution was placed in an oven at 488 K for 12 h. Upon hydrolysis of TiCl₃ and decomposition of sucrose, TiO₂ and carbon were formed. The obtained material was ground well and calcined initially under air atmosphere to remove the carbon partially. It was followed by calcination in nitrogen atmosphere to improve the crystallinity of TiO₂. Calcination of the catalyst in N₂ atmosphere (containing 2 % O₂) was done at 573 K, 673 K, 773 K and 873 K in order to vary the amount of carbon. Pure TiO₂ was prepared by heating the solution of sucrose and TiCl₃ at 488 K for 12 h followed by calcination in air at 873 K. The conditions of preparation of various catalysts are given in Table 2.1. Carbon-Degussa P25 TiO₂ was prepared by dispersing P25 TiO₂ in an aqueous solution of sucrose followed by heating in an oven at 488 K. The amount of carbon in the case of carbon-P25 TiO₂ was modified by varying the calcination temperature.

Table 2.1 Methodology for the preparation of various TiO₂ and carbon-TiO₂ catalysts

Sample code	Carbon source	TiO ₂ source	Calcination in air		Calcination in N ₂	
			K	Time (h)	K	Time (h)
STA66	Sucrose	TiCl ₃	873	6	Not done	Not done
STA30N36	Sucrose	TiCl ₃	573	4	573	6
STA30N46	Sucrose	TiCl ₃	573	4	673	6
STA30N56	Sucrose	TiCl ₃	573	4	773	6
STA30N66	Sucrose	TiCl ₃	573	4	873	6
SDA400	Sucrose	P25 TiO ₂	673	4	Not done	Not done
SDA360	Sucrose	P25 TiO ₂	633	4	Not done	Not done
SDA365	Sucrose	P25 TiO ₂	638	4	Not done	Not done
SDA370	Sucrose	P25 TiO ₂	643	4	Not done	Not done
SDA375	Sucrose	P25 TiO ₂	648	4	Not done	Not done

2.2.3 Preparation of CdSnO₃ and Cd₂SnO₄

In a typical procedure, CdSnO₃ was prepared from separate aqueous solutions containing 3CdSO₄ · 8H₂O (2.77 × 10⁻³ mol) and SnCl₄ · 5H₂O (8.59 × 10⁻³ mol). The two solutions were then added to an aqueous solution of NaOH (0.0625 mol) to precipitate Cd²⁺ and Sn⁴⁺ ions. The precipitate obtained was stirred overnight, washed to remove the sulphate and chloride and then dried at 333 K. The powder obtained was calcined at 1123 K under air for 6 h.

Cd_2SnO_4 was prepared as follows: An aqueous solution containing $\text{SnCl}_4 \cdot 5\text{H}_2\text{O}$ (8.59×10^{-3} mol) was precipitated by adding to an aqueous solution of NaOH (0.036 mol). The solution was stirred overnight and the obtained precipitate was washed to remove the chloride. The precipitate was then dissolved in concentrated H_2SO_4 and $\text{CdSO}_4 \cdot 8\text{H}_2\text{O}$ (5.55×10^{-3} mol) was added. The Cd^{2+} and Sn^{4+} ions were then precipitated by adding to an aqueous solution of NaOH (0.526 mol) and stirring overnight. The precipitate obtained was washed to remove the sulphate, dried and calcined in the presence of air at 1173 K for 6 h.

2.2.4 Preparation of Au/TiO₂

2.2.4.1 Preparation of TiO₂ from TiCl₄

0.15 M solution of TiCl_4 was added to 250 mL of 3.0 M HCl in a 500 mL sealed bottle and heated to 373 K for 48 h (Pottier *et al.*, 2001). The resulting precipitate contained both brookite and rutile TiO_2 . The brookite phase was separated by peptisation as follows: The precipitate was dispersed in 3.0 M nitric acid and the resulting suspension was centrifuged. The solid phase obtained was dispersed in water and then centrifuged. The centrifugate was freeze dried to obtain pure brookite which was dried at 373 K for 4 h. The TiO_2 prepared is labelled as BRT4.

2.2.4.2 Preparation of TiO₂ from TiCl₃:

In addition, TiO_2 was also prepared using TiCl_3 according to the procedure adopted by Lee *et al.*, (2008) as follows: 30 g of urea was dissolved in a litre of 0.015 M TiCl_3 solution. The resulting solution was refluxed at 373 K for 7 h whilst stirring. This leads to the formation of a cream coloured precipitate. The cream coloured

precipitate formed was then separated by centrifugation followed by repeated washing with de-ionized water and finally with anhydrous ethanol. The precipitated powder was then dried at 373 K for 2 h in an oven. TiO₂ prepared by this method was denoted as BRT3.

2.2.4.3 Gold loading by sol deposition method

2.2.4.3.1 Preparation of gold sol

Solution A: 600 mL of 3.33×10^{-4} M HAuCl₄ solution.

Solution B: The solution was made by mixing 32 mL of 1 wt % sodium citrate, 8 mL of 1 wt % tannin and 120 mL of water. pH of the solution was adjusted to 8 using 4 wt % sodium carbonate solution.

Solution A and solution B were heated separately to 333 K with continuous stirring. Solution B was then added to solution A (600 mL) and maintained at 333 K for 30 min under stirring. The colour of the solution turned pink due to the formation of gold sol.

2.2.4.3.2 Adsorption of gold sol on TiO₂

Gold sol was adsorbed on to the surface of TiO₂ using poly (diallyldimethylammonium chloride) (PDDA). The amount of PDDA solution required for complete adsorption was different for the various supports. Hence, the amount of PDDA solution required for complete adsorption of gold sol was calculated beforehand for the different supports by adding PDDA solution drop wise to a mixture of 5 mg of the catalyst and 2 mL of sol. The PDDA solution required for the various supports were 0.023 mL/mg, 0.035 mL/mg and 0.020 mg/mL for P25 TiO₂,

BRT3 and BRT4 respectively. The dispersion obtained was stirred for 90 min. Due to the adsorption of gold nanoparticles on the surface, the TiO₂ particles turned pink while the solution became colourless. The resulting precipitate was washed with water and dried at 333 K for 24 h. Gold sol was thus loaded on BRT4, BRT3 and commercial Degussa P25 TiO₂. The amount of gold taken for loading on these catalysts was 2 wt %.

2.2.4.4 Gold loading on TiO₂ by deposition-precipitation method:

Gold was loaded onto BRT4 and P25 TiO₂ by adopting the method reported by Yan *et al.*, (2004 & 2005). Typical method comprises of the preparation of a stock solution of gold by dissolving 1.0 g of HAuCl₄.3H₂O in 100 mL water. 15 mL of HAuCl₄ stock solution was diluted using water to 25 mL in a beaker. pH was adjusted to 8 by using 1.0 M KOH. pH higher than 8 leads to the precipitation of gold ions present in the solution. The solution was heated to 333 K with constant stirring. 500 mg of TiO₂ (Degussa P25) was added to the above solution at 333 K and stirred for 2 hrs. The solution thus obtained was centrifuged at 5000 rpm for 10 min and the solid obtained was washed and centrifuged thrice with 30 mL of water and finally with ethanol. The solid obtained was dried at 333 K for 12 h. The amount of gold taken for loading on these catalysts was 2 wt %.

2.3 CHARACTERIZATION

2.3.1. Diffuse reflectance UV-Visible spectrophotometric studies (DRS)

Diffuse reflectance UV-Visible absorption spectra of the catalysts were recorded using a Thermo Scientific Evolution 600 spectrophotometer equipped with a Praying Mantis diffuse reflectance accessory.

2.3.2 Powder X-ray diffraction (XRD)

X-ray diffraction patterns of various samples were recorded using a Rigaku D/max 2400 diffractometer using Ni-filtered Cu K α radiation ($\lambda = 1.5418 \text{ \AA}$) in the range of 10-90 degrees at a scan rate of 3 degrees per min.

2.3.2.1 Crystallite size determination by XRD line broadening

The crystallite sizes of the materials were calculated by XRD broadening technique employing Debye-Scherrer equation (Cullity, 1971) as shown below:

$$t = \frac{0.89 \lambda}{\beta \cos \theta_B}$$

Where

t = crystallite size

λ = wavelength of the radiation used

β = integral breadth of peak (full width at half maximum)

θ_B = Bragg diffraction angle

For these measurements, the X-ray diffraction patterns were recorded and the reflections corresponding to three highest intense peaks were taken for the calculation of the average particle size.

2.3.3 Surface area measurements

Surface area and pore volume of the catalysts were measured using CE Instruments model Sorptomatic 1990. The samples were out gassed at 423 K and 10^{-3} torr vacuum for 6 - 10 h depending on the nature of the sample. For adsorption experiments, pure nitrogen was used at liquid nitrogen temperature.

2.3.4 Transmission electron microscopic studies (TEM)

Transmission electron micrographs were recorded with a JEOL-JEM 100SX microscope, working at a 100 kV accelerating voltage. Samples for TEM were prepared by dispersing the powdered sample in acetone by sonication followed by drop drying on a copper grid (400 mesh) coated with carbon film.

2.3.5 Scanning electron microscopic studies (SEM)

Scanning electron micrographs were taken using FEI Model: Quanta 200. The sample powders were deposited on a carbon tape before mounting on a sample holder.

2.3.6 Thermogravimetric analysis (TGA)

Thermogravimetric analysis of catalyst precursor was performed to know the calcination temperatures. The TG was recorded using a Perkin Elmer TGA (Delta series TGA7) instrument with a heating rate of 20 K min^{-1} under air atmosphere.

2.3.7 UV-Visible spectrophotometry

Analysis of the degradation of the methylene blue, *p*-chlorophenol and calorimetric estimation of Ce were monitored using Jasco V-530 UV-Visible spectrophotometer.

2.3.8 Infrared (IR) absorption studies

FT-IR absorption spectra of the samples were recorded using a Bruker FT-IR spectrometer (Tensor 27) at room temperature in the range $4000\text{-}400 \text{ cm}^{-1}$. The powdered samples were ground with KBr and pressed into pellets (5 ton/cm^2) for recording the spectra.

2.3.9 Inductively Coupled Plasma (ICP) analysis

Gold loading on TiO_2 was confirmed using ICP-OES analysis (Model: Perkin Elmer Optima 5300 DV): Known amount of catalyst was first heated at 473 K in an ammonium sulphate and concentrated H_2SO_4 mixture to dissolve the TiO_2 . The remaining sulphuric acid was evaporated by heating to 573 K. The gold was then dissolved in hot aqua regia at 423 K followed by evaporating the aqua regia at 473 K.

2.4 PHOTOCATALYTIC ACTIVITY

2.4.1 Photocatalytic degradation of methylene blue using Ce-TiO₂

Photocatalytic degradation of methylene blue in visible light was carried out in a glass reactor (9 cm x 3.5 cm) with an outer jacket for water circulation. A sample of 100 mg of the catalyst was suspended in 80 mL of $53.49 \times 10^{-6} \text{ mol L}^{-1}$ ($42.79 \times 10^{-7} \text{ mol / 80 mL}$) aqueous methylene blue solution. The contents were stirred using a magnetic stirrer. The solution was stirred in dark for 30 min to attain the adsorption-desorption equilibrium and it was then irradiated using a 400 W high pressure mercury lamp (Newport Corporation, USA). Light of wavelengths < 420 nm were cut off using a filter (HOYA L-42). The irradiation was carried out for 90 min. The samples were then centrifuged at 12,000 rpm to remove the suspended catalyst particles and then analyzed using UV-Visible spectrophotometer after required dilution. The degradation of methylene blue was monitored by measuring the absorbance at 662 nm (λ_{max}). In another study, reactions were carried out under ultraviolet light irradiation in a photocatalytic apparatus which contains eight 8 W (64 W) Hg lamps which emit only light of wavelength 365 nm. A quartz reactor (18 cm x 3.5 cm) was used and the reactions were carried out under similar conditions as those employed in the visible light studies.

2.4.2 Photocatalytic degradation of methylene blue using carbon-TiO₂ composites

Photocatalytic degradation of methylene blue in UV-Visible light was carried out in a quartz reactor (18 cm x 3.5 cm) with an outer jacket for water circulation. A sample of 100 mg of the catalyst was suspended by stirring magnetically in 80 mL of 50 ppm

(13.37×10^{-5} mol/L) (11.45×10^{-6} mol / 80 mL) aqueous methylene blue solution. The degradation of methylene blue was monitored by measuring the absorbance at 662 nm (λ_{\max}) as described in 2.4.1.

2.4.3 Photocatalytic degradation of *p*-chlorophenol using CdSnO₃ and Cd₂SnO₄

Photocatalytic degradation of *p*-chlorophenol was carried out using a quartz reactor (20 cm X 4.5 cm) with an outer jacket for water circulation. A sample of 50 mg of the catalyst was suspended in 50 mL of 25 ppm aqueous *p*-chlorophenol solution. The solution was stirred in dark for 30 min to attain the adsorption-desorption equilibrium and it was irradiated using a 480 W high pressure mercury lamp (Newport Corporation, USA) where light of wavelengths < 420 nm were cut off using a filter (HOYA L-42). The irradiation was carried out for 90 min. The samples were then centrifuged at 12,000 rpm to remove the suspended catalyst particles. The degradation of *p*-chlorophenol was analyzed using UV-visible spectrophotometer by measuring the absorbance at λ_{\max} 223 nm after making necessary dilution of the sample. In another study, reactions were carried out under UV-Visible light (without HOYA L-42 filter) irradiation in the same photocatalytic apparatus under identical conditions as those in visible light studies.

2.4.4. Photocatalytic hydrogen evolution studies

Photocatalytic hydrogen evolution experiments were performed using a quartz reactor with provisions for water circulation at the outer wall of the reactor and specific outlet for gas collection. For a typical photocatalytic experiment, 50 mg of the catalyst was added to 35 mL of water: methanol mixture (5:1 ratio). Before illumination by the

light source, the solution was purged with nitrogen gas for 30 min to remove the dissolved oxygen. Then the mixture was irradiated with photons from 480 W Hg lamp (Newport corporation, USA) with both UV-Visible and Visible ($\lambda > 420$ nm) light. The evolved gas can be collected over brine solution using an inverted gas burette and the volume can be measured.

2.5 ESTIMATION OF CERIUM BY COLOURIMETRY

To estimate the exact amount of Ce loaded onto various Ce-TiO₂ samples, colourimetric method of estimation was carried out (Kolthoff *et al.*, 1963; Sandell, 1959). Cerium ion in the oxidation state of +4 has an absorption maximum at 320 nm. By monitoring the absorbance at 320 nm, the amount of Ce was estimated. This was carried out by dissolving the catalyst in hot concentrated sulphuric acid. The resulting solution was diluted and all the Ce was oxidized to Ce⁴⁺ using potassium persulphate as the oxidizing agent in the presence of silver sulphate as the catalyst. The resulting solution was boiled for 15 min to decompose the excess persulphate since persulphate also absorbs at 320 nm. The amount of cerium was then estimated by UV-Visible spectrophotometry.

2.6. ADSORPTION AND DESORPTION EXPERIMENTS

To study the decrease in the concentration of methylene due to its adsorption on catalyst surface, reactions were also carried out in the dark under similar conditions as those employed during irradiation studies. Desorption experiments were carried out to confirm that all methylene blue was adsorbed only on the catalyst surface. Desorption was done by separating the used catalyst from the reaction mixture by

centrifugation followed by drying at 333 K. This was followed by sonicating the catalyst in dimethyl sulphoxide (DMSO) for 30 min followed by centrifugation to remove the catalyst. The process of sonication of the catalyst in DMSO followed by centrifugation was repeated thrice. The obtained clear solution was made up to known volume and analyzed by UV-Visible spectrophotometry.

2.7 IMPEDANCE MEASUREMENTS

The working electrodes for evaluating the electrochemical properties of the cadmium stannates were fabricated by mixing 90 wt % of the respective stannate with 10 wt % polyvinylidene difluoride (PVdF) binder and a few drops of 1-methyl-2-pyrrolidinone (NMP). The mixture was ground well to form a uniform colloid. The colloid was then coated (area of coating = 1 cm²) on pre-treated Ti foil (0.1 mm thick) and dried at 333 K for 12 h in air. Electrochemical impedance spectroscopy (EIS) studies were performed on CHI 7081C electrochemical workstation using three-electrode configuration with Ti foil coated with cadmium stannate as the working electrode, Pt foil (1 × 2 cm²) as the counter electrode and Ag/AgCl as the reference electrode. The electrodes were dipped in 0.5 M Na₂SO₄ deoxygenated aqueous electrolyte adjusted to pH 7. The electrochemical impedance spectra were measured by imposing a frequency of 10⁻² to 10⁵ Hz with an amplitude of 5 mV. For Mott-Schottky measurements, the potential was scanned with 0.1 V per step from -0.5 V to 0.9 V.

2.8 CATALYTIC OXIDATION OF CO USING Au/TiO₂

Carbon monoxide oxidation was measured in a reactor at atmospheric pressure connected to a Quadruple Mass Spectrometer (QMS). The fresh catalyst was pressed

in a hydraulic press and the resultant pellet was crushed. The obtained powder was sieved and particles in the range 0.25 mm to 0.4 mm were used for the catalytic studies. Sixty mg of catalyst was used, which was calcined *in situ* at 673 K in 20 vol. % O₂ in Ar for 1 h (10 K/min heating rate, 30 mL/min gas flow). Temperature programmed reaction was performed with 35 mL/min of gas flow (0.5 vol. % carbon monoxide, 9.4 % oxygen, 51.9 % helium and 38.2 % argon) and at a ramp rate of 5 K/min. The ion currents of CO₂ (m/e = 44) and CO (m/e = 28) were monitored during heating and cooling of the catalysts under the flow of the reaction mixture. The heating and cooling cycles were repeated until the concordance in ion current vs. temperature plot was achieved. The CO oxidation activity was measured before and after the calcination of the catalyst in O₂. Conversion of CO was calculated on the basis of the CO₂ ion current (m/e = 44) from the mass spectrometer after making appropriate corrections.

2.9 CHEMICAL OXYGEN DEMAND (COD) ANALYSIS

COD for the phenolic samples was determined using open reflux method (Clesceri *et al.*, 1998). For analysis, 25 mL of phenol solution was taken in a 250 mL single neck round bottom flask. 1.0 g HgSO₄ and several glass beads were added to the above solution, and 5.0 mL sulphuric reagent (5.5 g AgSO₄/ kg H₂SO₄) was added very slowly with mixing to dissolve HgSO₄. The resulting mixture was cooled while mixing to avoid possible loss of volatile materials. 25 mL of 0.04167 M K₂Cr₂O₇ solution was added to the above solution and mixed well. The flask was attached with a water-cooling condenser, and 70 mL of sulphuric reagent was added to the mixture through the open end of the condenser. The above mixture was refluxed for 2h, cooled and diluted to about twice its volume with distilled water. The excess K₂Cr₂O₇ was

titrated with 0.25 M ferrous ammonium sulphate (FAS), using 0.10 to 0.15 mL ferroin indicator. Blank experiment was also done with distilled water.

$$\text{COD as mg O}_2 / \text{L} = \frac{(A - B) \times M \times 8000}{\text{ml of sample}}$$

A = mL FAS used for blank

B = mL FAS used for sample

M = molarity of FAS

8000 = milliequivalent weight of oxygen X 1000 mL/L

CHAPTER 3

CHARACTERIZATION AND PHOTOCATALYTIC ACTIVITY OF Ce MODIFIED TiO₂

3.1 INTRODUCTION

Protection of environment and the possibility of a renewable energy sources are the two major issues that the world has been facing recently. Photocatalysis can possibly contribute to solving these two issues. A photocatalyst capable of utilizing sunlight to decompose the various pollutants present in air, water and solid surfaces can drastically decrease the level of pollutants present in the environment. In addition, a photocatalyst which can split water to produce hydrogen utilizing sunlight can contribute to a renewable energy source. TiO₂ has been widely used and studied photocatalyst because of its desirable properties like stability, low cost, high light absorption, favourable band positions and inertness. However, the bandgap of TiO₂ is large and can function only by absorbing UV light, whereas sunlight contains only 7 % UV radiation. For a catalyst to be able to work using sun light, it should absorb light in the visible region. This can be achieved by reducing the bandgap of available materials like TiO₂ by doping with various cations (Kim *et al.*, 2004; Klosek and Raftery, 2002; Morikawa *et al.*, 2006; Shi *et al.*, 2006; Zhu *et al.*, 2004 & 2006) or anions (Sathish *et al.*, 2005 & 2007; Yamaki *et al.*, 2002) or by coupling with other materials (Bassekhouad *et al.*, 2006; Ho and Yu, 2006; Wu *et al.*, 2006) having a lower bandgap.

Various attempts have been made to decrease the bandgap of TiO₂ by doping various transition metal ions like V, Cr, Fe, Co, Ni and Cu. However, conflicting results with both increase (Kim *et al.*, 2004; Klosek and Raftery, 2002; Morikawa *et al.*, 2006; Shi *et al.*, 2006; Zhu *et al.*, 2004 & 2006) and decrease (Cameiro *et al.*, 2007; Chang *et al.*, 2005) in activity, compared with pure TiO₂, have been reported. Recently, there have been studies dealing with rare earth elements like Ln, Nd, Eu and Ce mixed with TiO₂ showing activity in the visible region (Carrettin *et al.*, 2004; Li *et al.*, 2005 & 2005a; Liu *et al.*, 2005; Liu and Gao, 2004; Nolan *et al.*, 2006; Pavasupree *et al.*, 2005; Tong *et al.*, 2007; Wei *et al.*, 2004; Xie *et al.*, 2005a & 2005b; Xie and Yuan, 2004a & 2004b). Rare earth elements mixed with TiO₂ show a red shift due to doping of rare earth elements leading to the formation of inter band states (Li *et al.*, 2005; Xie and Yuan, 2004a). Moreover, with addition of rare earth element, the recombination of the electrons and holes decreased effectively. This has been attributed to trapping of charge carriers as wells as their faster movement along the surface of TiO₂ due to the presence of rare earth elements (Li *et al.*, 2005a; Xi *et al.*, 2005b; Xie and Yuan, 2004b).

Among various rare earth elements, Ce has been reported to be consistently showing activity in visible region when mixed with TiO₂ (Liu *et al.*, 2005; Pavasupree *et al.*, 2005; Tong *et al.*, 2007). The advantage associated with Ce is that it is one among the four most abundant rare earth elements. CeO₂ is widely used in fuel cells and pollution control applications because of its redox behaviour, oxygen defects and catalytic activity (Carrettin *et al.*, 2004; Nolan *et al.*, 2006). Catalytic properties of CeO₂ have been attributed to the formation of Ce³⁺ defect sites and subsequent oxygen vacancies. CeO₂ is an *n*-type semiconductor whose bandgap has been reported to be varying from 2.7 to 3.4 eV depending on the method of preparation

(Ozer, 2001). In the present study Ce modified TiO₂ has been prepared by a simple and economical route and its photocatalytic activity is studied for the degradation of methylene blue. A polyacrylamide gel route has been used to synthesize the nanoparticles of the catalyst (Douy and Odier, 1989; Pal *et al.*, 2007; Pan *et al.*, 2008). With polymeric chains forming a network, metal ions are entrapped evenly within the polyacrylamide gel, which prevents the agglomeration of the particles.

Although various reports deal with visible light activity of Ce modified TiO₂, the mechanism has not yet been convincingly evolved. Understanding the mechanism involved in the observed visible light activity of Ce modified TiO₂ will be of help in developing catalytic systems with improved activity in the visible region. Some of the reports claim that Ce when doped into the lattice of TiO₂ leads to the formation of interband states resulting in photocatalytic activity when exposed to visible light (Pavasupree *et al.*, 2005; Tong *et al.*, 2007). But the size difference between Ce (Ce⁴⁺ : 0.093 nm, Ce³⁺ : 0.103 nm) and titanium (Ti⁴⁺ : 0.068 nm) is so large that Ce cannot be accommodated in to the TiO₂ lattice.

The aim of this study is to explain the mechanism involved in the observed visible light activity of Ce modified TiO₂. Earlier reports claim that modifying TiO₂ with Ce will decrease the recombination of charge carriers because of the redox behaviour exhibited by the Ce⁴⁺/Ce³⁺ couple (Pavasupree *et al.*, 2005; Tong *et al.*, 2007). In such a case Ce modified TiO₂ should have a higher activity than TiO₂, when the reactions are carried out in UV light alone. In order to make sure that Ce³⁺/Ce⁴⁺ couple decreases the recombination rate, the reactions were also carried out in the UV light.

3.2 RESULTS AND DISCUSSION

3.2.1 X-ray diffraction study

X-ray diffraction patterns of all the prepared samples are given in Fig. 3.1. Ce-TiO₂ shows peaks corresponding to the presence of both anatase (JCPDS File No. 21-1272) and rutile (JCPDS File No. 21-1276) phases up to a Ce loading of 1 %. At 2 % loading of Ce (Fig. 3.1e) and above, the rutile peaks disappeared and peaks due to cubic CeO₂ phase appeared (Fig. 3.1b-3.1d).

This is in agreement with the reported ability of Ce to suppress the transformation of anatase to rutile phase (Xu *et al.*, 2006). It is known that added substances can affect the phase transformation in both ways. Inhibition of phase transition can be due to structural dissimilarity and facilitating phase transformation can arise due to structural similarity. This is significant since the anatase phase of TiO₂ is photocatalytically more active than rutile phase. Furthermore, this shows that the loaded Ce is present in the form of CeO₂ in the prepared catalyst. XRD patterns of all the samples irrespective of the Ce loading showed line broadening which indicates the formation of nanoparticles. To further confirm the presence of CeO₂ in the samples with low amount of Ce, XRD measurements were performed for all the samples at a slow scan rate of 0.25 degree per min and 0.01 degree step size. The corresponding XRD patterns are given in Fig. 3.2, where the presence of CeO₂ peaks can be observed even at 0.5 and 1 % loading of Ce.

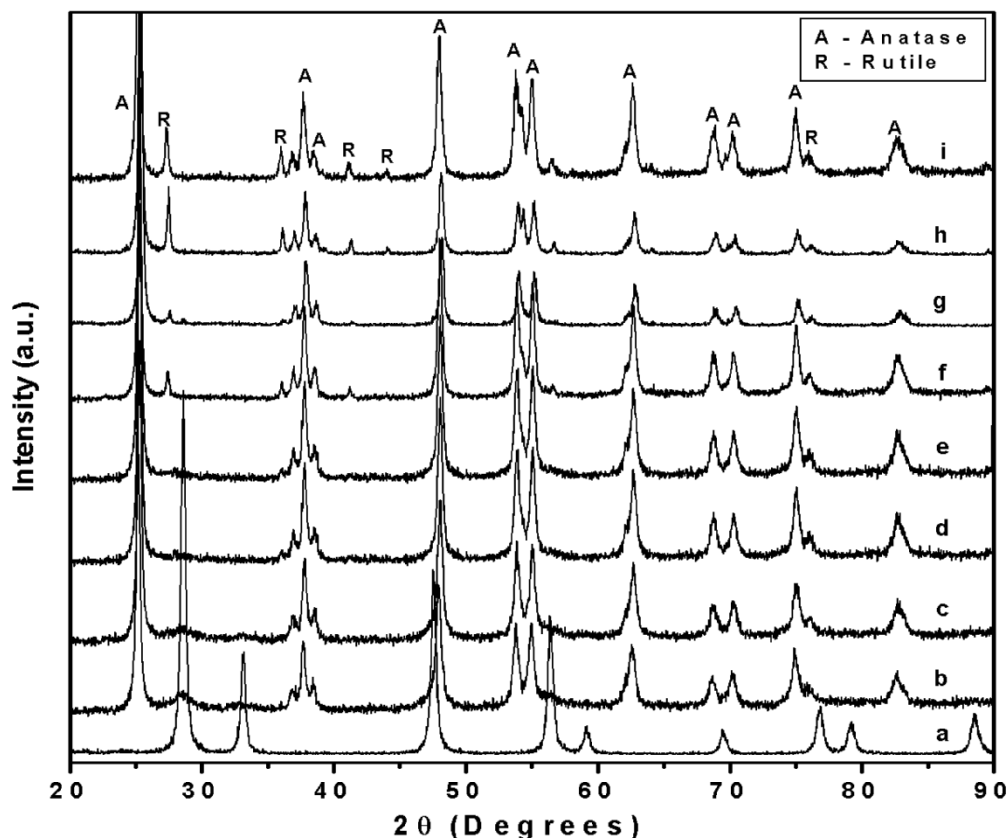


Fig. 3.1. XRD patterns of (a) CeO_2 (b) 9 % $\text{CeO}_2\text{-TiO}_2$ (c) 5 % $\text{CeO}_2\text{-TiO}_2$ (d) 3 % $\text{CeO}_2\text{-TiO}_2$ (e) 2 % $\text{CeO}_2\text{-TiO}_2$ (f) 1 % $\text{CeO}_2\text{-TiO}_2$ (g) 0.5 % $\text{CeO}_2\text{-TiO}_2$ (h) 0.25 % $\text{CeO}_2\text{-TiO}_2$ (i) TiO_2

3.2.2 Diffuse reflectance UV-visible spectral studies

UV-Visible absorption spectra of TiO_2 , CeO_2 and Ce modified TiO_2 are given in Fig. 3.3. From the onset of the absorption edge, the bandgap of the various samples were calculated using the method adopted by Tandon and Gupta (1970). UV-Visible absorption spectrum showed an absorption onset at 400 nm for pure TiO_2 and at 450 nm (Bandgap = 2.76 eV) for pure CeO_2 . Patsalas *et al.*, (2003) have found that the bandgap of CeO_2 varies and lower bandgap could be attributed to the presence of Ce^{3+}

ions in the grain boundaries depending on the method of preparation. For the CeO_2 loaded TiO_2 samples, the absorbance showed a redshift with increase in the CeO_2 loading which shows that CeO_2 is responsible for the observed shift in CeO_2 modified TiO_2 samples. A redshift of up to 50 nm was observed for CeO_2 loaded samples.

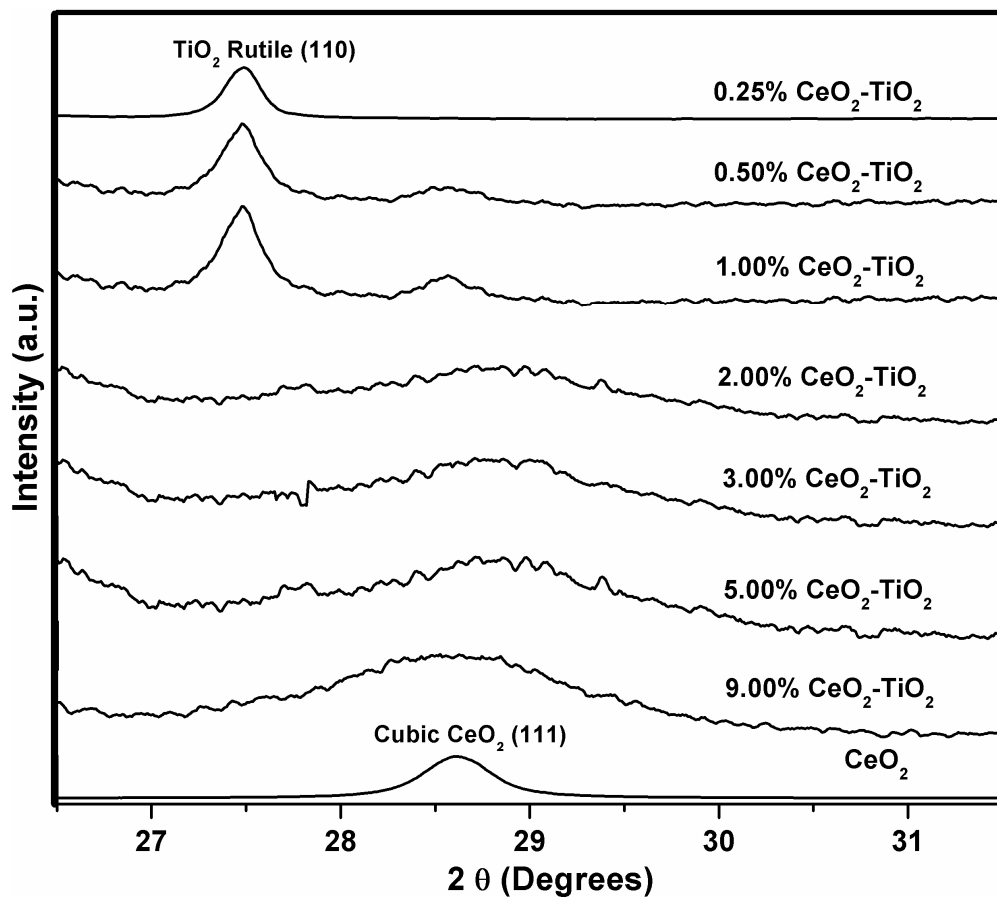


Fig. 3.2. XRD patterns of the samples scanned at a slow rate (0.25 degree per min)

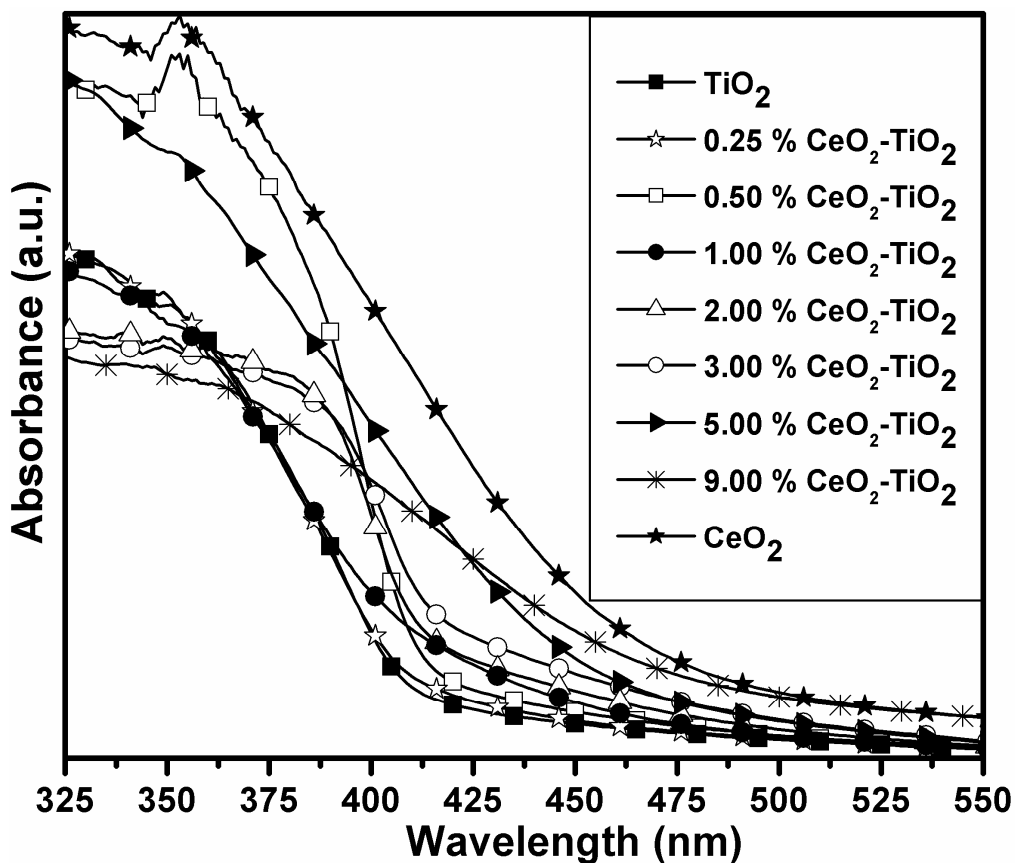
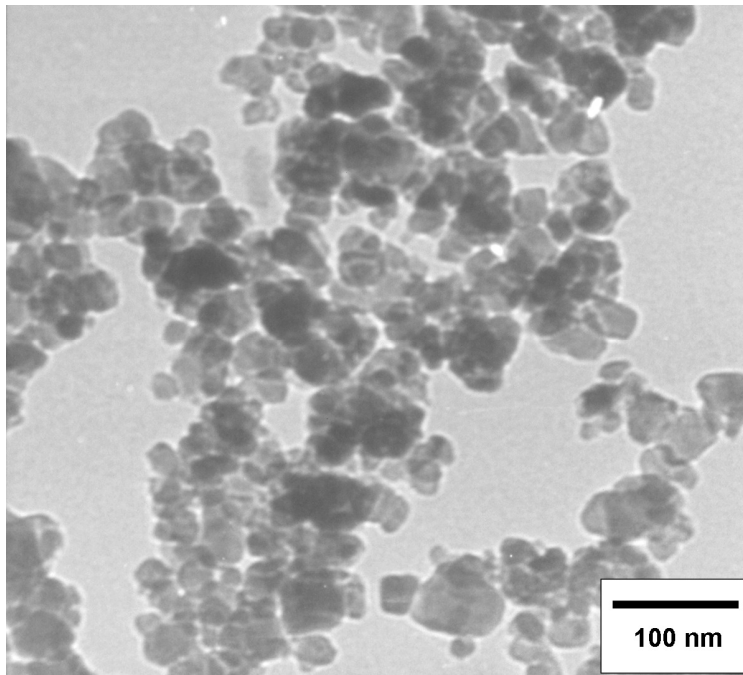


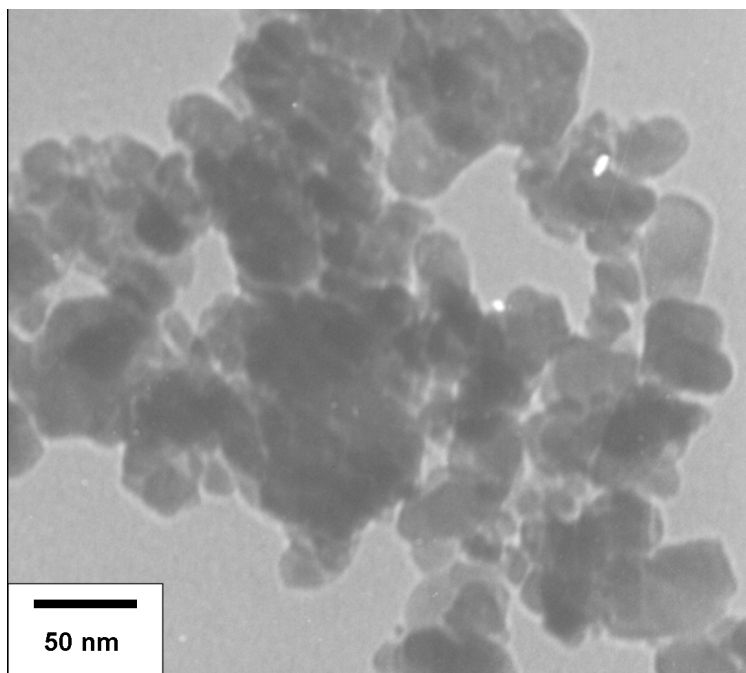
Fig. 3.3. UV-Visible absorption spectrum of the CeO₂ modified TiO₂ photocatalysts

3.2.3 TEM and SEM analysis

TEM images of the CeO₂ modified TiO₂ samples at different magnifications are given in Fig. 3.4. TEM analysis shows that nanoparticles don't have any specific shape. Particles were present closely in the form of chains which are typically observed in most of the reported microscopic images of TiO₂ (Park and Kang, 2005; Yang *et al.*, 2007; Zhang *et al.*, 2006). The particle sizes were found to be distributed in a wide range (10-50 nm) and majority of the particles were of 25 nm in size. SEM images of CeO₂ modified TiO₂ samples are given in Fig. 3.5.

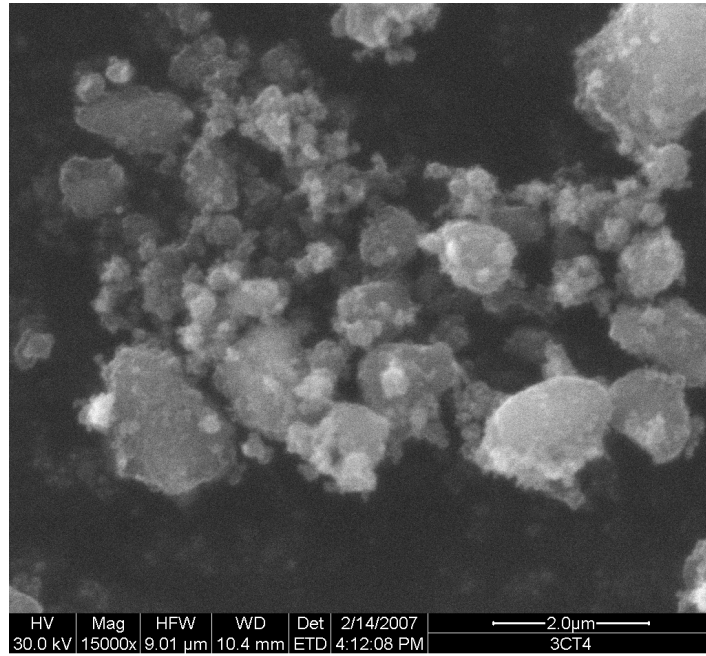


(a)

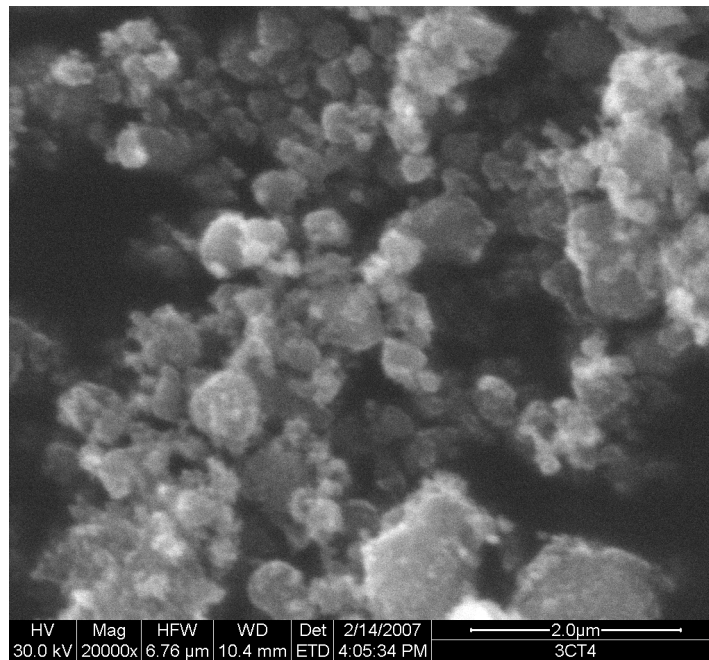


(b)

Fig. 3.4. TEM images of 3 % CeO₂ modified TiO₂



(a)



(b)

Fig. 3.5. SEM images of 3 % CeO₂ modified TiO₂

3.2.4 TGA and Elemental analysis

The TGA profile of as-synthesized TiO₂ showed a weight loss up to 723 K which can be attributed to the decomposition of the polyacrylamide. Based on this observation, the samples were calcined at 873 K for 6 h in air. Energy Dispersive X-ray (EDX) spectrum of CeO₂ modified TiO₂ confirmed the presence of titanium, oxygen and cerium in the prepared oxides. Percentages of cerium (IV) oxide in the prepared catalysts, estimated by colourimetry are given in Table 3.1. The results were well in agreement with the cerium taken in the precursor.

Table 3.1 Colourimetric estimation of Ce⁴⁺ in the mixed oxides

Percentage of CeO₂ loaded	Percentage of CeO₂ estimated
0.25	0.23
0.50	0.46
1.00	0.93
2.00	1.87
3.00	2.84
5.00	4.70
9.00	8.55

3.2.5 Adsorption and photocatalytic studies

The overall decrease in the concentration of methylene blue under visible light irradiation is presented in Table 3.2. Considerable decrease in the concentration was observed in the case of pure TiO₂ which does not have visible light absorption. In order to check whether adsorption of methylene blue on the photocatalyst has a role in its decrease in concentration, reactions were carried out in the absence of irradiation, under similar conditions as those adopted under irradiation. Reactions carried out in dark helped in establishing the reaction mechanism involved as well. The concentrations of methylene blue adsorbed on the catalyst in the absence of irradiation are shown in Table 3.3. It can be seen that the decrease in the concentration of methylene blue under dark, in the case of pure TiO₂ is the same as that observed under irradiation conditions. Moreover, the concentration of methylene blue adsorbed was found to decrease with increasing concentration of CeO₂. The reason for adsorption could be as follows: methylene blue, which is chemically 3,7-bis (dimethylamino) phenazathionium chloride trihydrate (by IUPAC nomenclature), has a positively charged sulphur atom as shown in (Fig. 3.6). Electrophoresis experiments showed that methylene blue remains positive in the pH range 4 to 9 (Fetterolf *et al.*, 2003). TiO₂ in aqueous solutions has a Point of Zero Charge (PZC) of 6. As a result, at pH > 6, the surface of TiO₂ becomes negatively charged. Since the reactions were carried out in neutral medium, positively charged methylene blue becomes adsorbed on negatively charged surface of TiO₂ by electrostatic attraction (Chen *et al.*, 2003; Chuan *et al.*, 2004; Fetterolf *et al.*, 2003). To further confirm that methylene blue is adsorbed on TiO₂ by purely electrostatic interactions, desorption experiments were carried out by dispersing the catalyst in a more polar solvent like DMSO. The results obtained were presented in Table 3.3. It can be seen that almost all the methylene

blue adsorbed on the catalyst was recovered during desorption experiments. The studies further pointed out that the amount of adsorption of methylene blue by TiO₂ was almost thrice compared to that of CeO₂.

Table 3.2 Overall and net photocatalytic decrease in concentration (photocatalytic) of methylene blue under UV and Visible irradiation after 90 min

Catalyst	Amount decreased (x 10 ⁻⁷ mol / 0.1 g catalyst)			
	Visible		UV	
	Overall	Net photocatalytic	Overall	Net photocatalytic
TiO ₂	9.63	0.53	32.40	23.30
0.25 % CeO ₂ -TiO ₂	14.65	6.31	34.56	26.22
0.50 % CeO ₂ -TiO ₂	17.01	9.74	37.28	30.01
1.00 % CeO ₂ -TiO ₂	16.80	10.27	40.45	33.92
2.00 % CeO ₂ -TiO ₂	14.65	8.87	39.22	33.44
3.00 % CeO ₂ -TiO ₂	14.12	8.66	31.61	26.18
5.00 % CeO ₂ -TiO ₂	11.34	6.74	28.17	23.57
9.00 % CeO ₂ -TiO ₂	9.73	5.55	26.83	22.65
CeO ₂	8.66	5.24	5.18	1.76

The decrease in concentration of methylene blue solely due to the photocatalytic degradation was thus obtained by subtracting the concentration of methylene blue adsorbed from the overall decrease in concentration (Table 3.2). The photocatalytic degradation of methylene blue was found to increase with an increase in CeO₂ up to a loading of 1 wt. % and beyond this loading the degradation of methylene blue was found to decrease. It is important to note that the photoactivity values of all CeO₂

modified TiO₂ samples were found to be higher than that of either pure TiO₂ or CeO₂. This indicates that CeO₂ and TiO₂ contribute to a synergistic effect in the photodegradation of methylene blue.

Table 3.3 Amount of methylene blue adsorbed in dark after 90 min of stirring and methylene blue desorbed from used catalyst using DMSO

Catalyst	Amount adsorbed (x 10 ⁻⁷ mol / 0.1 g catalyst)	Amount desorbed (x 10 ⁻⁷ mol / 0.1 g catalyst)
TiO ₂	9.10	8.55
0.25 % CeO ₂ -TiO ₂	8.34	7.81
0.50 % CeO ₂ -TiO ₂	7.27	6.74
1.00 % CeO ₂ -TiO ₂	6.53	5.88
2.00 % CeO ₂ -TiO ₂	5.78	5.46
3.00 % CeO ₂ -TiO ₂	5.46	4.82
5.00 % CeO ₂ -TiO ₂	4.60	4.28
9.00 % CeO ₂ -TiO ₂	4.18	3.74
CeO ₂	3.42	3.10

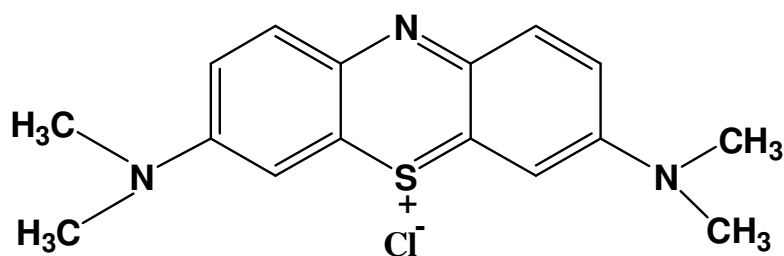


Fig. 3.6. Structure of methylene blue

3.2.6 Mechanism for the activity in visible light

There are two possible mechanisms for the observed visible light photocatalytic activity of the Ce modified TiO₂. The first possibility is the formation of mixed oxides upon the substitution of Ce into the TiO₂ lattice. This may result in the formation of additional energy states belonging to partially filled Ce 4f levels between the conduction and valence band (VB) of TiO₂. Visible light can excite the electrons from the VB to the interband Ce 4f levels or from the Ce 4f levels to the conduction band (CB) leading to the formation of electrons and holes. Formation of mixed oxides of Ce and Ti can be revealed by studying the XRD patterns. There are six phases of mixed oxides which are reported in the JCPDS database. X-ray diffraction patterns for the Ce modified TiO₂ show no peaks corresponding to any of these six phases of Ce-Ti mixed oxides even at the highest loading of 9 % of CeO₂. In addition, doping of Ce into the lattice of TiO₂ should lead to an increase in d-values between the corresponding planes. The calculated d-values for both the anatase and rutile peaks for various Ce modified TiO₂ catalysts were found to be the same as that of pure TiO₂. This can be attributed to the absence of doping of Ce into the lattice of TiO₂ in the Ce modified TiO₂ samples. Doping of Ce into TiO₂ lattice is not possible due to the fact that Ce and Ti have different coordination numbers of 8 and 6 in CeO₂ and TiO₂ respectively. It is difficult for the 8 coordinated Ce present in cubic lattice of CeO₂ to replace 6 coordinated Ti in tetragonal lattice of TiO₂. Further the ionic sizes of Ce⁴⁺ and Ti⁴⁺ are 0.093 nm and 0.068 nm respectively; the difference in ionic radius being high and hence lattice substitution in TiO₂ by Ce⁴⁺ is highly improbable. This shows that Ce is present as CeO₂ on the surface of TiO₂ (Xu *et al.*, 2006).

The second mechanism which can explain the observed visible light activity is the coupled semiconductor mechanism. Band energy positions of the various oxides involved, like CeO₂, Ce₂O₃ and TiO₂ were required to establish the coupled semiconductor mechanism. To calculate the band positions of CeO₂, the method used by Xu and Schoonen (2000) was employed. This method was verified for more than 30 metal oxides and sulphides and was found to be well in agreement with the experimentally determined values. This method is based on the idea that the electronegativity of a compound is the geometrical mean of the electronegativities of various elements involved. For example, the electronegativity of TiO₂ can be given by

$$\chi(\text{TiO}_2) = [\chi(\text{Ti}) \chi^2(\text{O})]^{1/3}$$

where $\chi(\text{TiO}_2)$, $\chi(\text{Ti})$, and $\chi(\text{O})$ are the electronegativities of TiO₂, titanium, and oxygen respectively. The electronegativity, electron affinity (EA), and ionization energy (IE) values of a compound were equivalent to that of the Fermi level energy, CB energy, and VB energy respectively (by adding or subtracting half of the bandgap value (i.e., $E_g/2$) from the electronegativity of the compound). The VB energy (IE) and CB energy (EA) of the compound can be calculated.

It can be represented by

$$\text{IE}(\text{TiO}_2) = E_{\text{VB}}(\text{TiO}_2) = \chi(\text{TiO}_2) + \frac{1}{2} E_g$$

$$\text{EA}(\text{TiO}_2) = E_{\text{CB}}(\text{TiO}_2) = \chi(\text{TiO}_2) - \frac{1}{2} E_g$$

where E_g , EA, IE, E_{CB} , and E_{VB} represent the bandgap, electron affinity, ionization energy, conduction band energy position and valence band energy positions

respectively of the compound. The values obtained were in absolute vacuum scale (AVS) and were converted to the normal hydrogen electrode (NHE) scale by subtracting 4.5 from them.

$$E_{CB}(\text{TiO}_2)_{(\text{in NHE})} = E_{CB}(\text{TiO}_2) - 4.5 \text{ eV}_{(\text{in AVS})}$$

The energy values of the bands calculated based on the above equations are listed in Table 3.4. The calculated energy position values show that both the oxides of Ce i.e., CeO₂ and Ce₂O₃ have their CB energies more negative than that of TiO₂. It is clear from the recorded UV-Visible spectrum (Fig. 3.3) and literature reports (Xu and Schoonen, 2000) that CeO₂ and Ce₂O₃ have bandgaps suitable to absorb light in the visible region up to 450 nm and 516 nm respectively.

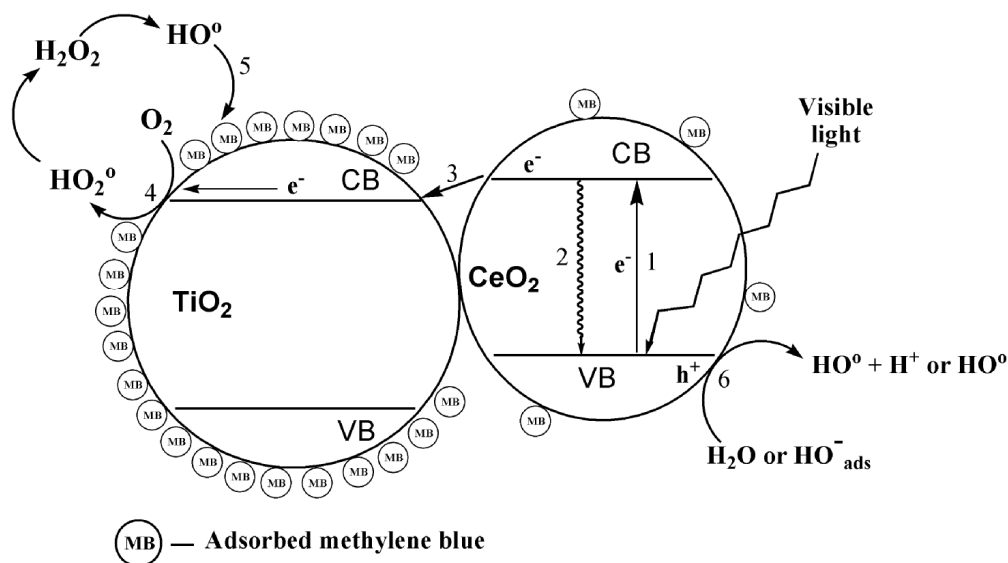
Table 3.4. Bandgap, conduction and valence band energy positions of various oxides

Semiconductor	Bandgap (in eV)	E_{CB} w.r.to NHE (in eV)	E_{VB} w.r.to NHE (in eV)
TiO ₂	3.20	-0.29	2.91
CeO ₂	2.76	-0.32	2.44
Ce ₂ O ₃	2.40	-0.47	1.93

Since CeO₂ and Ce₂O₃ absorb light in the visible region and have CB energy values more negative than that of TiO₂, they will transfer excited electrons to the CB of TiO₂. Ce₂O₃ is an unstable compound and gets oxidized to CeO₂ in the presence of trace amounts of O₂. Even though the presence of Ce₂O₃ has not been confirmed, it

may exist in aqueous medium under the photocatalytic reaction conditions. The electrons present in the CB of TiO₂ will then be used for various processes leading to the formation of hydroxyl radicals which will then oxidize the adsorbed methylene blue. In the case of CeO₂, even though it can form the oxidizing species like hydroxyl radicals there is lesser availability of methylene blue on CeO₂ surface as compared to TiO₂ (Table 3.3). Thus the hydroxyl radicals formed through CB of CeO₂ recombine to form H₂O₂ or react with other species without oxidizing the methylene blue. Since the excited electrons in CeO₂ are immediately transferred to TiO₂, the recombination of charge carriers is significantly decreased in the coupled CeO₂-TiO₂ system compared to pure CeO₂. A pictorial representation of the coupled semiconductor mechanism responsible for visible light activity is given in Scheme 3.1.

However, it is assumed that the visible light induced degradation of methylene blue is small as the absorption wavelength required for methylene blue is 662 nm. Previous reports also have showed a very little decrease in methylene blue under photolysis. Madhavi and Tim (2007) reported a 12 % degradation of methylene blue under UV + visible light photolysis whereas 100 % degradation can be achieved in the presence of catalyst under identical conditions. This shows that the observed degradation of methylene blue is due to the photocatalytically generated electrons and holes and not due to the self degradation of methylene blue.



Scheme 3.1 Coupled semiconductor mechanism in CeO₂ modified TiO₂ leading to visible light activity (**Step 1.** Excitation of CeO₂ by visible light; **Step 2.** Recombination of charge carriers; **Step 3.** Transfer of excited e⁻ to CB of TiO₂; **Step 4.** Transfer of electron from CB of TiO₂ to dissolved O₂; **Step 5.** Oxidation of methylene blue by hydroxyl radicals; **Step 6.** Oxidation of H₂O and HO⁻ to HO[•] by holes)

3.2.7 Optimum loading of CeO₂ on TiO₂

Photocatalytic activity of CeO₂ modified TiO₂ catalysts, in the visible region, increased with CeO₂ loading and reached a maximum with 1.0 % CeO₂ loading. Further loading of CeO₂ decreased the activity and at 9 % CeO₂ loading, the activity was similar to that of CeO₂. This can be explained as follows: CeO₂ in the prepared catalysts is uniformly dispersed over the TiO₂ surface. CeO₂ can absorb visible light and then transfer the excited electrons to TiO₂, whereas TiO₂ can adsorb methylene blue efficiently. At 0.5 % and 1.0 % loading of CeO₂, the coverage of TiO₂ surface by CeO₂ is optimum so that enough CeO₂ can be in contact with TiO₂ as well as there is enough uncovered surface of TiO₂ where methylene blue can get adsorbed. This leads to a situation where the following four steps such as (i) absorption of light by

CeO₂ resulting in excited electrons and holes, (ii) transfer of electrons to TiO₂, (iii) adsorption of methylene blue on TiO₂ and (iv) the oxidation of methylene blue by hydroxyl radicals, takes place simultaneously in an optimum manner. As the loading of CeO₂ is increased, the surface of TiO₂ is increasingly covered by CeO₂ and lesser surface of TiO₂ is in contact with the methylene blue solution. Thus even though the absorption of light by CeO₂ increases, the adsorption of methylene blue by TiO₂ decreases due to the lowering of the available surface area leading to the hampering of the reaction of methylene blue with the hydroxyl radicals. CeO₂ modified TiO₂ (2-5 %) catalysts showed higher activity than pure TiO₂ but less than that of 1 % CeO₂ modified TiO₂. At a loading of 9 % of CeO₂, the surface is almost fully covered by CeO₂ and even though there is enough visible light absorption, there is only little adsorption of methylene blue on TiO₂. Thus, 9 % CeO₂ loaded sample gave almost the same activity as that of pure CeO₂.

Optimum loading of CeO₂ (1 %) can also be attributed to larger decrease in the recombination of electrons and holes. When there is a thin layer of CeO₂ present on the surface of TiO₂, the excited electrons created in CeO₂ due to visible light irradiation can be immediately transferred to TiO₂. This leads to an efficient separation of the electrons and holes across the boundary between TiO₂ and, thereby decreasing the recombination. Above the optimum loading of CeO₂, the thickness of CeO₂ layer becomes higher, and the electrons and holes created on the CeO₂ at the surface get recombined before the electrons travel and reach the CeO₂-TiO₂ interface. These results demonstrate the poor visible light photocatalytic activity of CeO₂ in spite of having a suitable bandgap and band position (because of the very high recombination as well as poor adsorption towards methylene blue). However, CeO₂ exhibits far better activity in the visible light compared to that of pure TiO₂.

3.2.8 Photocatalytic activity in UV light

There are some reports which claim that the $\text{Ce}^{3+}/\text{Ce}^{4+}$ redox couple can decrease the recombination by enabling faster electron transfer along the TiO_2 surface (Li *et al.*, 2005b; Xu *et al.*, 2006). Since increase in activity of CeO_2 modified TiO_2 in the visible light can be attributed to the coupled semiconductor mechanism, we have carried out the reactions using only UV light to study the effect of $\text{Ce}^{3+}/\text{Ce}^{4+}$ couple in reducing recombination (Table 3.2). The results showed that modifying the TiO_2 with CeO_2 considerably enhanced the activity in the UV light as well. Even with 0.25 % CeO_2 loading, an increase in the activity compared to pure TiO_2 is observed. The optimum CeO_2 loading was found to be between 0.5 - 2.0 %. With further increase in CeO_2 loading the activity was found to decrease and was found to be lesser than that of pure TiO_2 . Pure CeO_2 showed negligible activity in the UV light. These observations can be explained as follows. The CB of TiO_2 has a potential of -0.29 V which is more negative than that of Ce^{4+} to Ce^{3+} reduction potential (1.61 V). Hence the CB electrons of TiO_2 are able to reduce Ce^{4+} to Ce^{3+} . Also, the VB of TiO_2 has a potential of $+2.91$ V which is more positive than Ce^{3+} to Ce^{4+} oxidation potential. The VB electrons can hence oxidize Ce^{3+} to Ce^{4+} . These reduced Ce^{3+} and oxidized Ce^{4+} species can subsequently transfer the charges to the species present in the reaction medium (Xie *et al.*, 2005b). Hence, ions of Ce decrease the recombination of the charge carriers and there by enhance the activity in the UV light as well. The observed optimum loading in this case can be attributed to the fact that CeO_2 is less active compared to TiO_2 . Below 3 % CeO_2 loading, the amount of $\text{Ce}^{4+}/\text{Ce}^{3+}$ species present on the TiO_2 surface is favourable for faster charge transfer and at the same time allows light to reach the TiO_2 surface. But above 3 % CeO_2 loading the amount

of CeO₂ on the surface of TiO₂ is very high such that, it blocks absorption of light by TiO₂ showing lesser activity compared to pure TiO₂.

3.3 CONCLUSIONS

CeO₂ modified TiO₂ nanoparticles were prepared by a simple polymer assisted method. Prepared CeO₂ modified TiO₂ samples showed red shift compared to TiO₂ and were active in the visible light for the photocatalytic degradation of methylene blue with 1.0 % CeO₂ modified TiO₂ showing the maximum activity. The mechanism of visible light photocatalytic activity of CeO₂-TiO₂ system was established. Added Ce is present as CeO₂ on the surface of TiO₂ and has its CB energy at a position more negative than that of TiO₂. CeO₂ absorbs visible light and transfers the excited electrons to CB of TiO₂ which was utilized for the photocatalytic degradation of methylene blue. In spite of the suitable band gap and band position, CeO₂ was less active in visible light compared to CeO₂ modified TiO₂ because of high recombination and poor adsorption of methylene blue. Higher CeO₂ loading resulted in a decrease in the activity because of the blocking of TiO₂ surface by CeO₂ as well as due to the increase in the recombination of charge carriers. Reactions in the UV light confirmed that CeO₂ loading decreases the recombination of charge carriers because of the easy redox nature of Ce⁴⁺/Ce³⁺ couple. Although the redshift in CeO₂ modified TiO₂ was less, insights obtained in this work while studying the mechanism will be helpful in developing coupled semiconductor photocatalysts. Moreover, the importance of adsorption in determining the photocatalytic activity showed that it should be given consideration before selecting the photocatalysts for different target compounds. This study also showed that coupling a photocatalyst with high recombination rate with a suitable material will enhance its activity.

CHAPTER – 4

CHARACTERIZATION AND PHOTOCATALYTIC STUDIES OF CARBON-TiO₂ COMPOSITES

4.1 INTRODUCTION

TiO₂ is one of the most prominent and promising photocatalyst because of its stability, inertness, low cost and wide availability. However, its wide spread commercial application has not been possible because of the higher recombination of electrons and holes and its inability to utilize the visible spectrum of sunlight. Research has been carried out to achieve visible light activity by doping TiO₂ with various elements like metals as well as non metals (Morikawa *et al.*, 2006; Sathish *et al.*, 2007). Several studies have been carried out to utilize the photons effectively. One of the ways of preventing recombination of electrons and holes is to use the generated electrons and holes as soon as they are formed. One way of achieving this is by using electron traps like Pt, Pd and hole traps like RuO₂ (Maeda *et al.*, 2008; Yamashita *et al.*, 2002). The electron and hole traps immediately capture the charges because of their favourable band energy levels compared to that of TiO₂. Once they are trapped they can be efficiently transferred to the reacting species thereby reducing recombination. However these metals are costly and cannot be used in the scale-up application expected for a photocatalyst.

Another way of decreasing the recombination rate is by increasing the availability of target molecules closer to the photocatalyst surface. This can be achieved by dispersing carbon on the surface of the photocatalyst. Carbon being inexpensive and

having simple preparation methods is the suitable choice for increasing the availability of the target compound near the photocatalyst surface. Carbon has its Fermi level at a lower energy than the conduction band of TiO₂. Hence, it functions as an electron sink similar to Pt, thereby reducing the recombination of the excited electrons and holes (Kongkanand and Kamat, 2007). In addition, carbon is expected to increase the rate of electron and hole transfer because of its conductivity (Oloman *et al.*, 1991).

There are reports in this regard, which have utilized carbon and TiO₂ together as a photocatalyst. Different methods have been adopted in the catalyst preparation. One of them is the use of carbon as a support for various forms of TiO₂, where TiO₂ has been prepared in a solution containing carbon (Geng *et al.*, 2008; Li *et al.*, 2008). Another method involves preparing carbon and TiO₂ separately and then mixing them in the same medium and carrying out the photocatalytic study (Ao *et al.*, 2008; Cordero *et al.*, 2007). In addition, there are reports in which carbon was formed over laboratory made or commercially available TiO₂ (Janus *et al.*, 2006; Hu *et al.*, 2008). Carbon has also been doped into the lattice of TiO₂ for achieving visible light photocatalytic activity (Neumann *et al.*, 2005). It is expected that preparing carbon and TiO₂ together in the same medium will help in achieving better interaction between carbon and TiO₂ and thereby facilitating the charge transfer between the catalyst and the target molecule. There are only a few studies where carbon and TiO₂ have been prepared in the same medium simultaneously (Li *et al.*, 2008).

This work involves (i) preparation of carbon and TiO₂ simultaneously using titanium (III) chloride and sucrose (ii) influence of various amounts of carbon in the

photocatalytic degradation of methylene blue has been studied and (iii) influence of the calcination temperature on the amount of carbon and the photocatalytic activity.

4.2 RESULTS AND DISCUSSION

4.2.1 X-Ray diffraction patterns

XRD patterns of the samples from sucrose and TiCl_3 calcined at different temperatures are shown in Fig. 4.1.

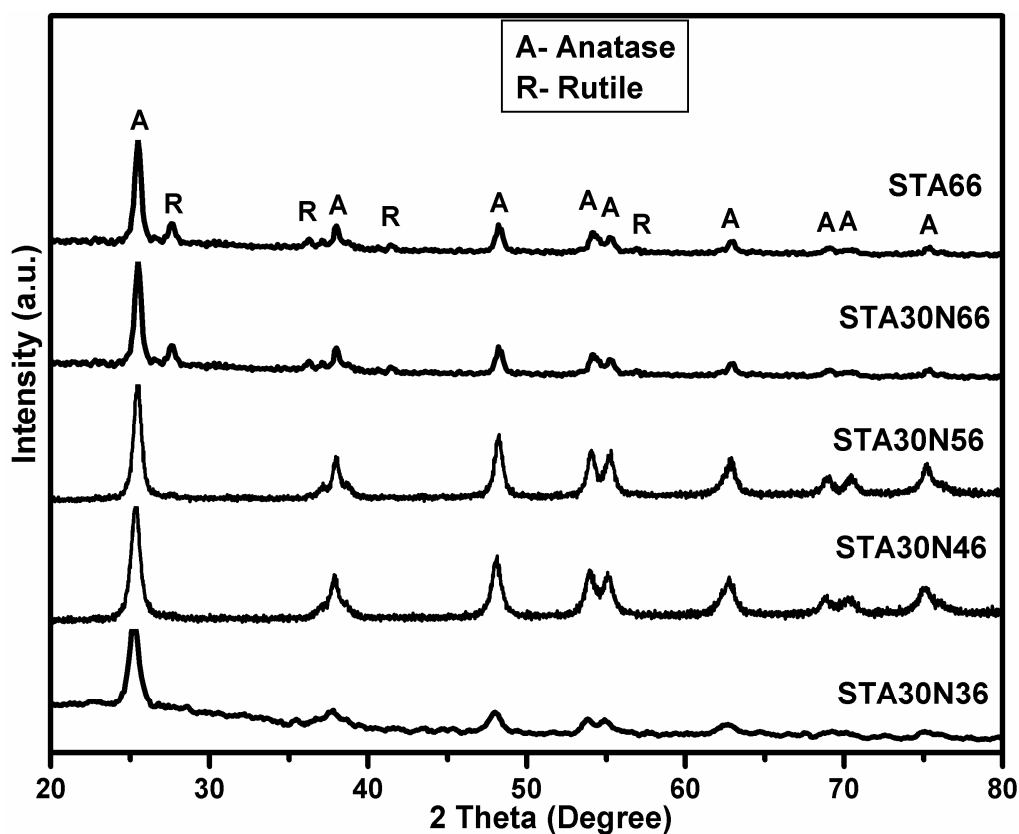


Fig. 4.1. XRD patterns of TiO_2 and carbon- TiO_2 samples calcined at different temperatures (Details of sample code are given in Table 2.1, Chapter 2)

Peaks corresponding to anatase phase of TiO_2 (JCPDS No. 21-1272) were observed in all the samples. Samples calcined at 573 K in N_2 (STA30N36) also showed the anatase phase although the intensity of the peaks were lower. The samples calcined at 873 K (STA30N66) showed the formation of anatase and rutile (JCPDS No. 21-1276) phases. Fig. 4.2. shows the XRD pattern of Carbon-P25 TiO_2 (SDA370).

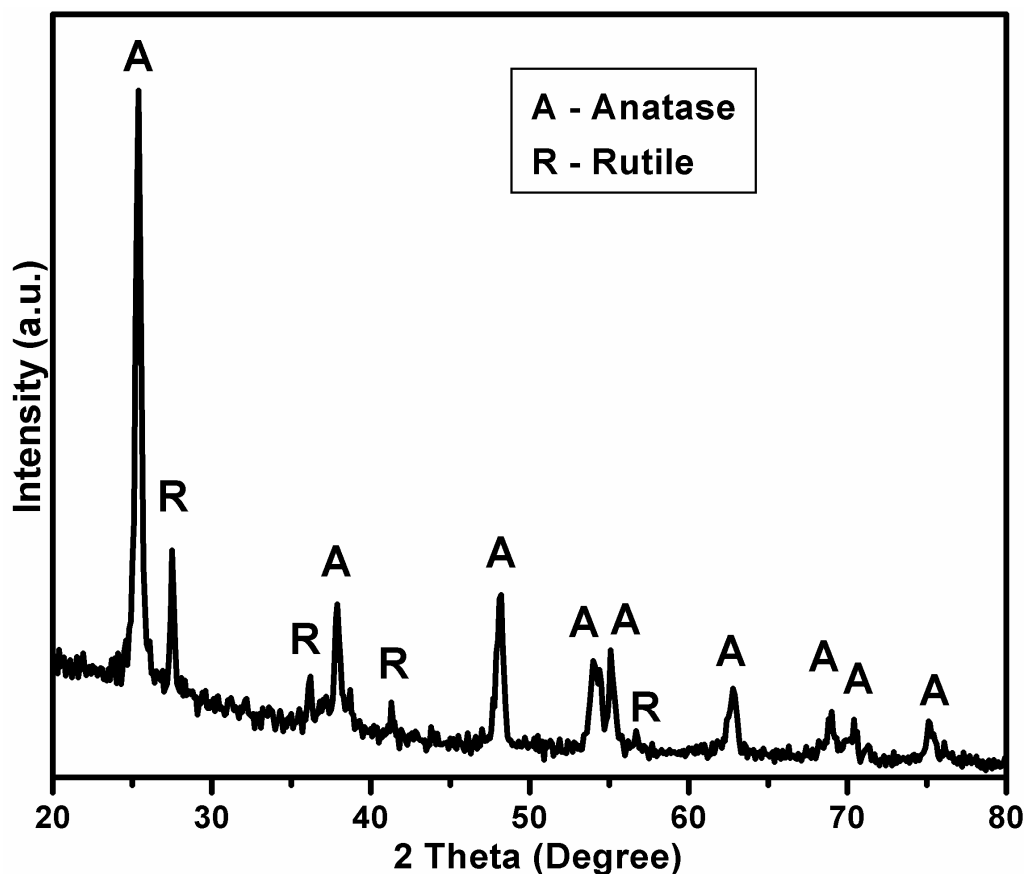


Fig. 4.2. XRD pattern of carbon- TiO_2 from sucrose and P25 TiO_2 (SDA370) calcined at 643 K

Peaks corresponding to both anatase and rutile phases were observed in the XRD pattern. This is well in agreement with the composition of Degussa P25 TiO₂ which is 75 % anatase and 25 % rutile.

4.2.2 Raman spectral studies

Raman spectral study was carried out to find out the nature of the allotropic forms of the carbon formed. Raman spectra of the carbon prepared from sucrose and STA30N66 are given in Fig.4.3. A G-band (1580 cm⁻¹) corresponding to an ideal graphite lattice vibration mode with E_{2g} symmetry and D-band (1360 cm⁻¹) corresponding to graphitic lattice mode vibration with A_{1g} symmetry were observed. Based on the presence of the above two bands, the carbon can be described as graphitic in nature (Sadezky *et al.*, 2003).

Furthermore, from the Raman spectrum it is clear that the TiO₂ is of anatase phase. The bands observed at 395, 515 and 638 cm⁻¹ arise from the optical modes represented as B_{1g} (ν₄), A_{1g} + B_{1g} (ν₂+ν₃) and E_g(ν₁) respectively (Liu *et al.*, 2007). Raman spectrum was taken for carbon prepared from sucrose without TiCl₃. It also showed the G and D-band of the graphitic carbon.

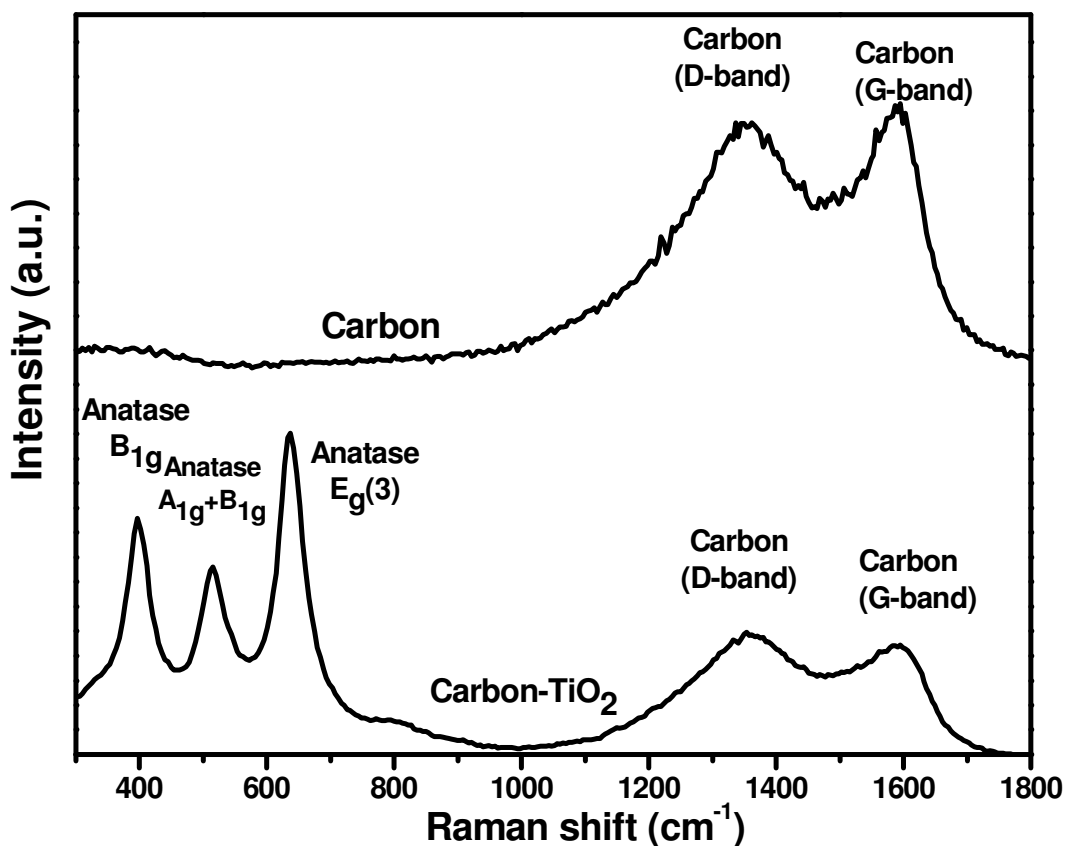


Fig. 4.3. Raman spectra of carbon prepared from sucrose and carbon-TiO₂ from sucrose and TiCl₃ (STA30N66) (Refer Table 2.1, Chapter 2 for details of sample code)

4.2.3 SEM studies

Scanning electron microscopy (SEM) studies were carried out to see the morphology of the catalysts. SEM images of the STA30N66 and SDA370 are given in Fig. 4.4 and Fig. 4.5 respectively. The SEM images of STA30N66 show agglomeration of particles of 0.5 to 2.5 μm. These agglomerates which are of circular shape with disordered edges were composed of TiO₂ held together by a film of carbon. SEM images of SDA370 show large aggregates of particles up to 20 μm in size.

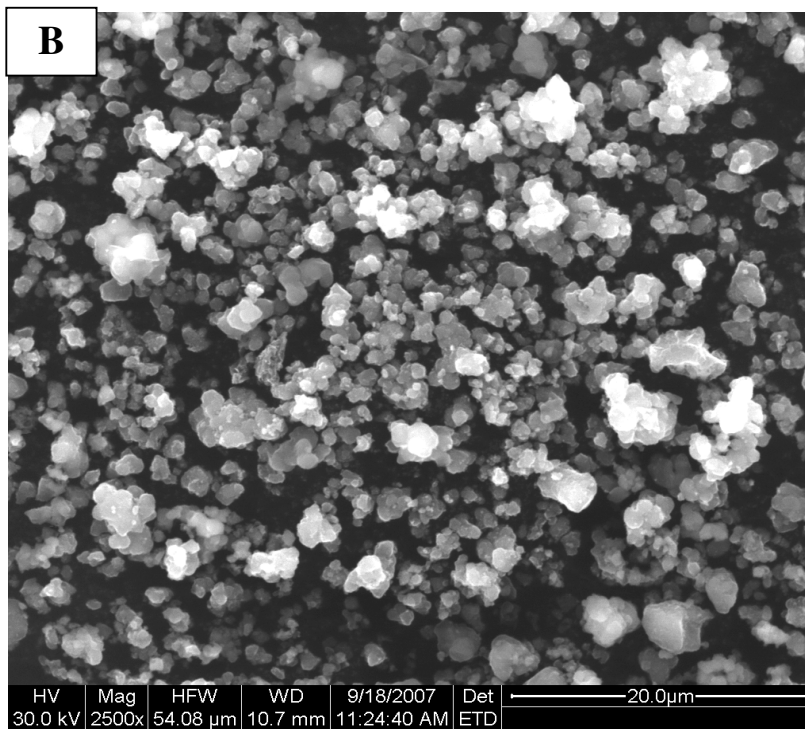
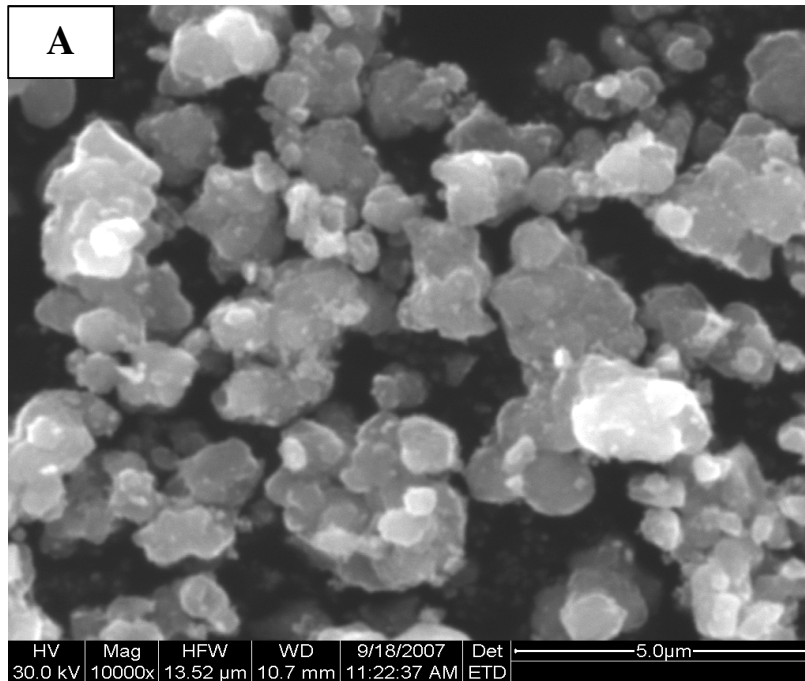


Fig. 4.4. SEM images of carbon-TiO₂ (STA30N66) (Refer Table 2.1, Chapter 2 for details of sample code)

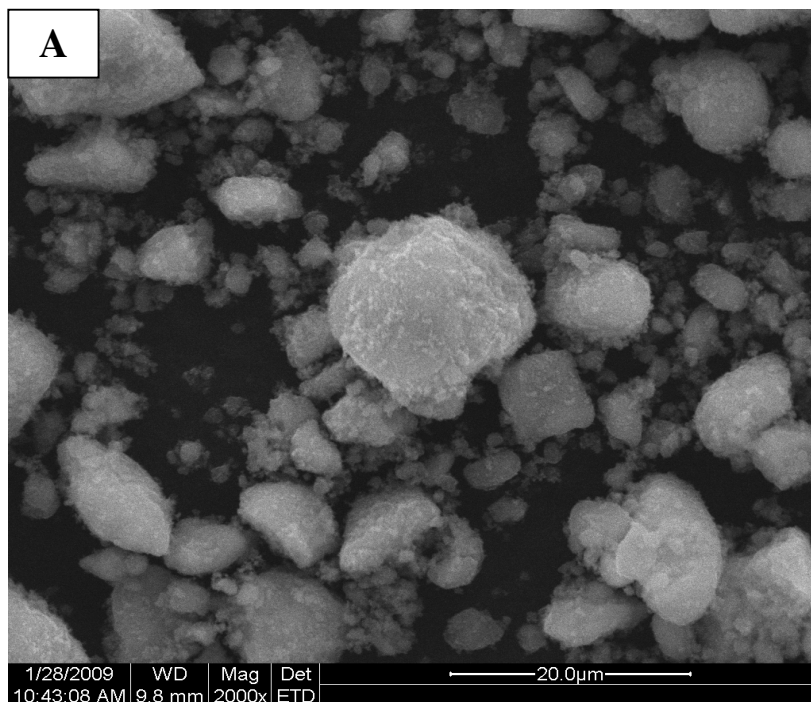


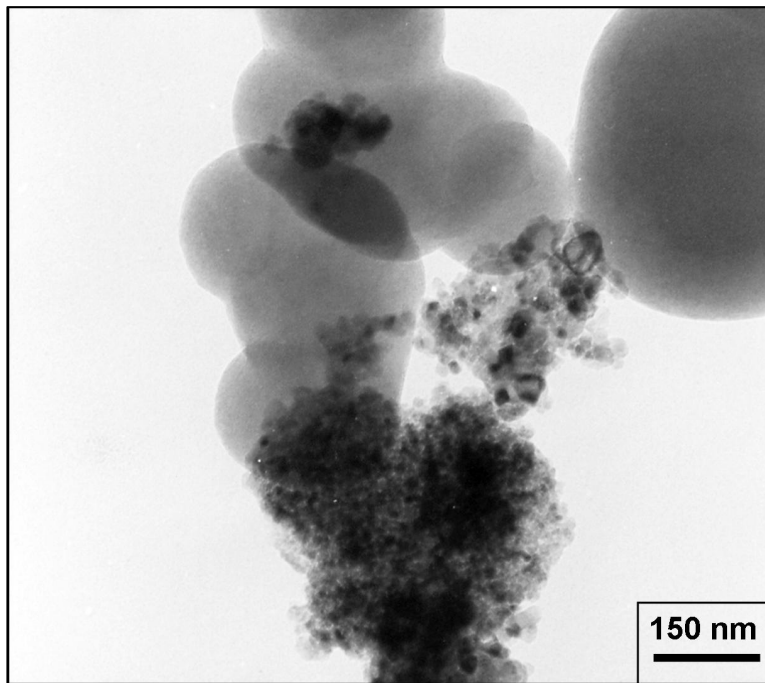
Fig. 4.5. SEM images of carbon-P25 TiO₂ (SDA370) (Refer Table 2.1, Chapter 2 for details of sample code)

4.2.4 TEM studies

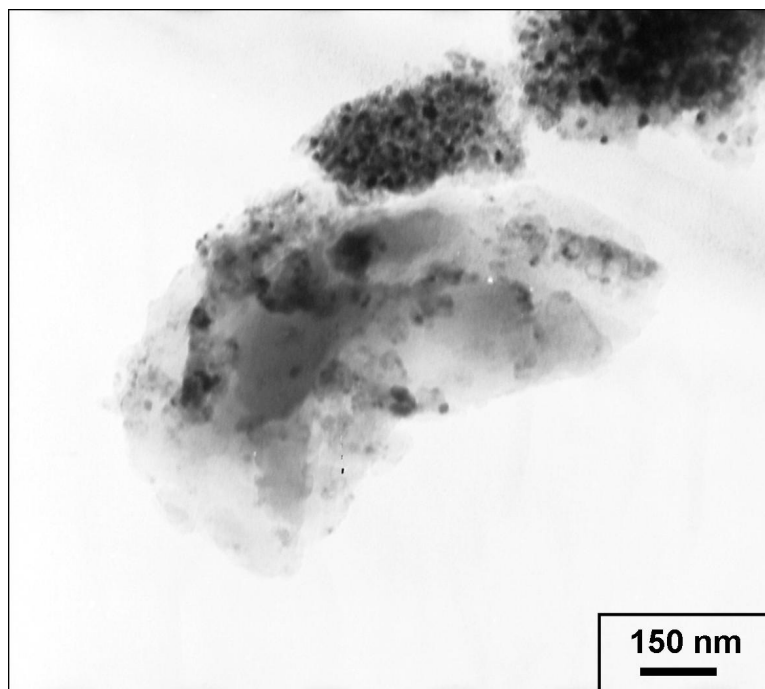
Transmission electron microscopic studies were carried out to find the particle size and the manner in which the carbon and TiO_2 exist in the prepared composite materials. TEM images of the carbon- TiO_2 samples from sucrose and TiCl_3 were given in Fig. 4.6. Similar to what was observed in the SEM images, aggregates of particles were observed in the TEM images.

The TiO_2 particles of size between 20-30 nm were found in the images in the case of the samples prepared from sucrose and TiCl_3 (STA30N66). The darker small particles were found to be TiO_2 and the large films were found to be carbon by EDX analysis. The TiO_2 particles were found to be embedded in a film of carbon and this shows that there is a very close existence of carbon and TiO_2 in the prepared catalysts.

In the case of carbon-Degussa P25 TiO_2 composite (SDA370) given in Fig. 4.7, the size of TiO_2 particles were found to be 50-60 nm, which is typical of Degussa P25 TiO_2 . In this case too, aggregates of TiO_2 particles were observed. In these composites, TiO_2 particles were found to be embedded in the carbon whereas many of TiO_2 particles exist as separate aggregates without any interaction with carbon. This shows that preparing TiO_2 and carbon together leads to better interaction between carbon and TiO_2 .

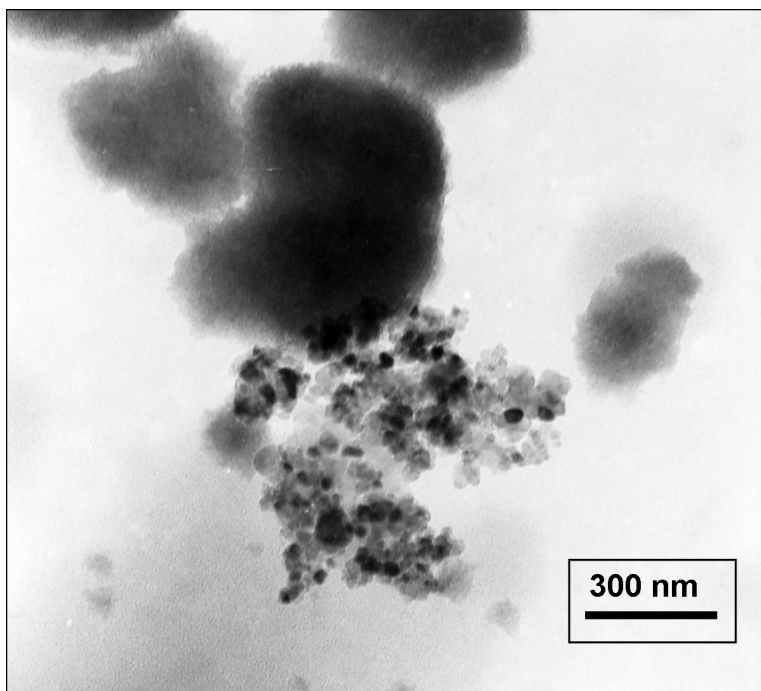


(a)

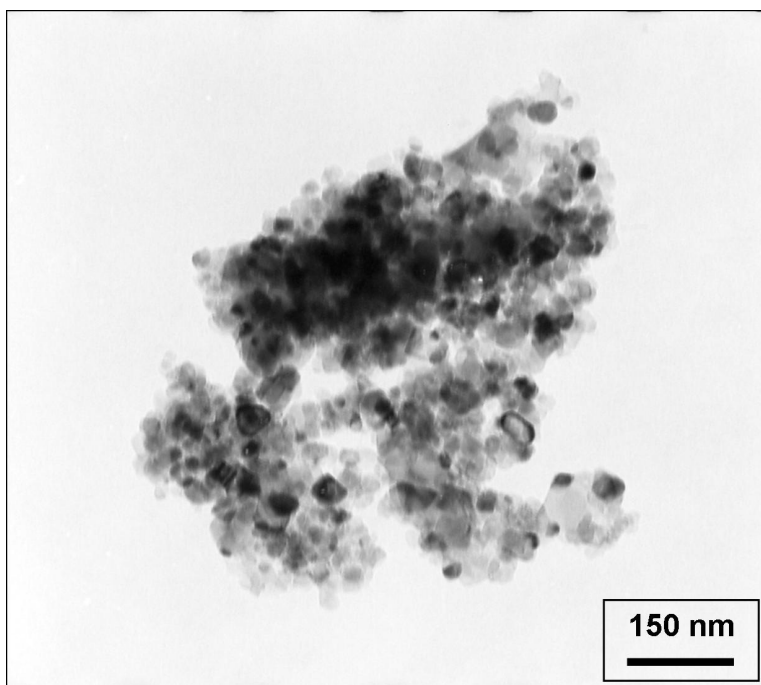


(b)

Fig. 4.6. TEM images of carbon-TiO₂ (STA30N66) (Refer Table 2.1, Chapter 2 for details of sample code)



(a)



(b)

Fig. 4.7. TEM images of carbon-P25 TiO₂ (SDA370) (Refer Table 2.1, Chapter 2 for details of sample code)

4.2.5 Diffuse reflectance UV-Visible spectral studies

4.2.5.1 Carbon-TiO₂ from TiCl₃

The diffuse reflectance UV-visible spectra of carbon-TiO₂ from TiCl₃ are given in Fig. 4.8. No significant difference was observed for samples calcined at different temperatures. Carbon having small bandgap of 1.4 eV, has absorption in the full UV - Visible spectrum. Moreover, there are no differences in the band gap (3.2 eV) energies during calcination at different temperatures. The absence of red shift means that doping of carbon is not taking place during the preparation process. Thus, any change in photocatalytic activity of the carbon-TiO₂ composite catalysts can only be attributed to the presence of carbon and TiO₂ being present together.

4.2.5.2 Carbon-P25 TiO₂

Fig. 4.9. shows the diffuse reflectance UV-visible spectra of carbon-P25 TiO₂ samples calcined at different temperatures. The UV-visible spectra of carbon-P25 TiO₂ samples calcined at various temperatures show a gradual increase in absorption in the UV region ($\lambda < 400\text{nm}$) with increase in calcination temperature. This is attributed to the decrease in the amount of carbon with increase in calcination temperature. Although carbon absorbs in the whole of UV-visible region, its absorption ability is lower than pure TiO₂ in the UV region. Degussa P25 TiO₂ showed higher absorption intensity in the UV region.

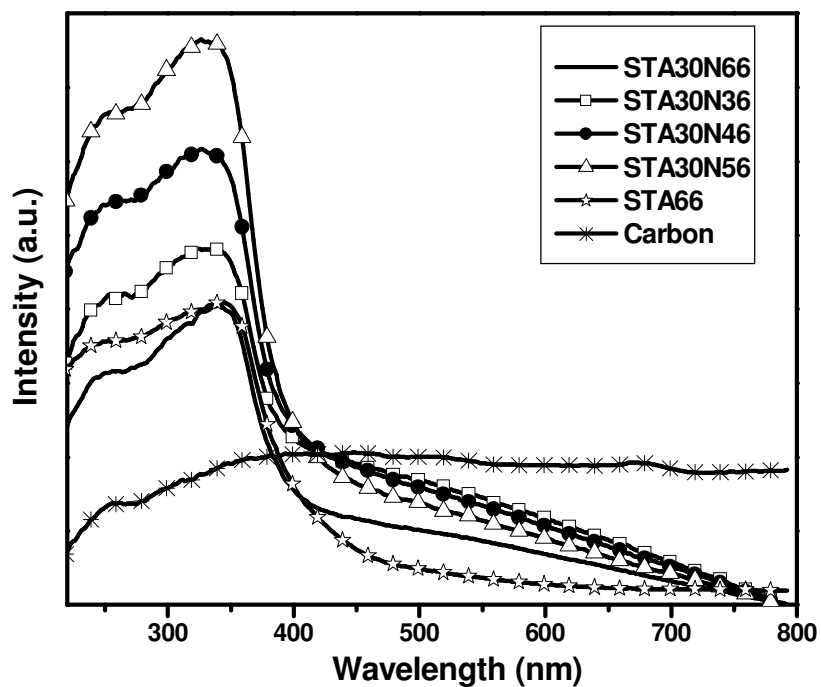


Fig. 4.8. Diffuse reflectance UV-visible spectra of carbon-TiO₂ from TiCl₃ (Refer Table 2.1, Chapter 2 for details of sample code)

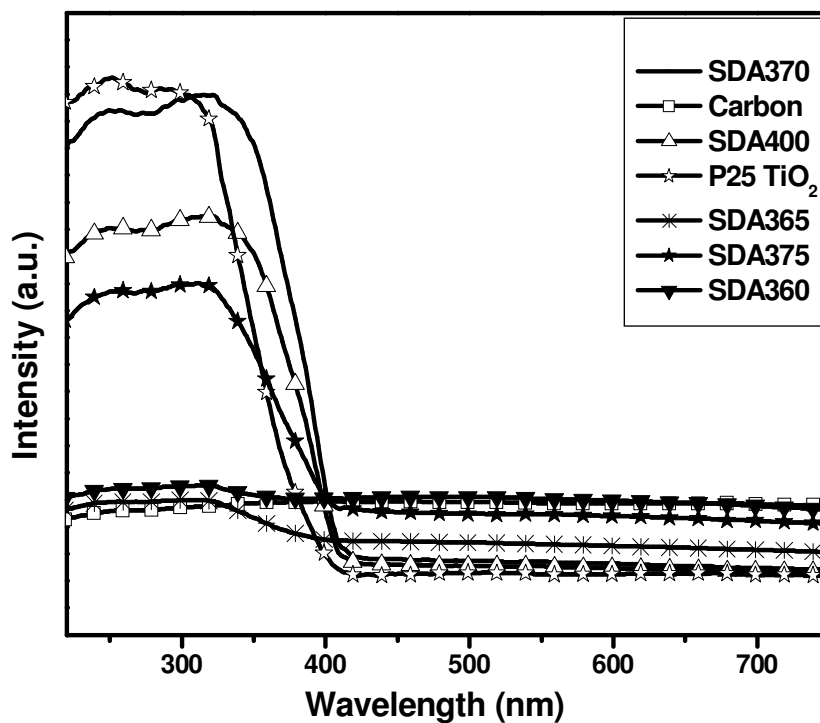


Fig. 4.9. Diffuse reflectance UV-visible spectra of carbon-P25 TiO₂ samples (Refer Table 2.1, Chapter 2 for details of sample code)

4.2.6 Photocatalytic experiments

4.2.6.1 Photocatalytic activity of carbon-TiO₂ from TiCl₃

The net decrease in the concentration of methylene blue under irradiation conditions is due to both the adsorption on the surface of the catalyst and the degradation by photocatalytic means. Hence, the net photocatalytic activity of the sample was calculated by subtracting the decrease in concentration of methylene blue in dark from that under irradiation. Table 4.1 shows the % carbon content, adsorption in dark and photocatalytic activities of the various samples. The results show a significant increase in photocatalytic activity in the case of carbon-TiO₂ composites compared to TiO₂. All the carbon-TiO₂ composite catalysts showed an increase in photocatalytic activity of at least 25 %. This increase in degradation of methylene blue shows that carbon plays a significant role in the photocatalytic degradation process.

It was observed that the adsorption in dark increases with increase in carbon content. The optimum carbon content was found to be 3 wt % (STA30N46). The lower activity of STA30N36 (5.4 % C) than STA30N46 (3.0 % C) can be attributed to the higher coverage of photoactive TiO₂ surface by carbon in the case of STA30N36. When coverage of carbon is high it prevents light from striking the TiO₂ surface, thereby preventing the formation of electrons and holes. The increase in the calcination temperature to 773 K leads to a decrease in activity due to the lowering of carbon content from 3.0 to 2.1 wt %. The increasing of calcination temperature to 873 K showed an additional decrease in activity due to the decrease in carbon content and formation of the photocatalytically lower active rutile phase.

Table 4.1. Photocatalytic activity and carbon content of the carbon-TiO₂ samples from TiCl₃ after 90 min irradiation

Sample code	wt % C	Decrease in methylene blue concentration (x 10 ⁻⁷ mol)		
		(Percentage decrease in concentration in brackets)		
		Irradiation	Dark (adsorption)	Photocatalysis (Irradiation – Dark)
STA66	NA	38.93 (34.0)	14.89 (13.0)	24.04 (21.0)
STA30N36	5.4	100.8 (88.0)	47.29 (41.3)	53.51 (46.7)
STA30N46	3.0	100.4 (87.7)	36.41 (31.8)	63.99 (55.9)
STA30N56	2.1	92.40 (80.7)	36.41 (31.8)	55.99 (48.9)
STA30N66	1.4	83.01 (72.5)	30.69 (26.8)	52.32 (45.7)

4.2.6.2 Photocatalytic activity of carbon-P25 TiO₂:

Photocatalytic studies for degradation of methylene blue using carbon-P25 TiO₂ composites showed improvement in activity compared to pure TiO₂ (Table 4.2). In this case, carbon-P25 TiO₂ (SDA370) showed only 10 % improvement in activity compared to pure TiO₂ (SDA400) prepared under similar conditions. Highest activity among the carbon-P25 TiO₂ samples was observed for the sample containing 0.5 % carbon. P25 TiO₂ which was directly used without treating with sucrose showed higher activity. The samples calcined at 633 K (SDA360) showed complete removal of methylene blue at 30 min both under irradiation and dark. This can be attributed to the higher amount of carbon present in this sample (C-13.4 %).

Table 4.2. Photocatalytic activity and carbon content of the carbon-TiO₂ samples from P25 TiO₂ after 90 min irradiation

Sample code	%	Decrease in methylene blue concentration (x 10 ⁻⁷ mol)		
		(Percentage decrease in concentration in brackets)		
		Irradiation	Dark (adsorption)	Photocatalysis (Irradiation – Dark)
SDA400	NA	63.20 (55.2)	10.76 (9.4)	52.44 (45.8)
P25 TiO ₂	NA	108.9 (95.1)	8.93 (7.8)	99.97 (87.3)
SDA360 (30 min)	13.4	112.7 (98.4)	112.2 (98.0)	0.50 (0.4)
SDA365	2.3	109.2 (95.4)	44.43 (38.8)	64.77 (56.6)
SDA370	0.5	103.6 (90.5)	29.20 (25.5)	74.40 (65.0)
SDA375	0.2	68.13 (59.5)	13.97 (12.2)	54.16 (47.3)

The comparison of the photocatalytic activity of the carbon-TiO₂ from TiCl₃ and carbon-P25 TiO₂ represents that the carbon-TiO₂ obtained by forming carbon and TiO₂ simultaneously in the same medium have higher activity than carbon prepared over commercial TiO₂. This improvement in activity can be attributed to the better interaction between carbon and TiO₂ when they were prepared together in addition to higher availability of the target molecules closer to the surface of the catalyst.

4.3 CONCLUSIONS

Carbon-TiO₂ composites were prepared by two different methods viz., (1) preparing carbon and TiO₂ together from sucrose and TiCl₃ and (2) preparing carbon over P25 TiO₂ using sucrose. By studying the amount of carbon from CHN analysis, it was found that a systematic variation in carbon content can be made by altering the calcination temperature. From TEM analysis, it was found that the carbon and TiO₂ have a better interaction in the method (1) than in the method (2). Diffuse reflectance UV-visible studies showed the absence of C doping in the samples, which indicates that any improvement in activity of carbon-TiO₂ samples can be attributed to the presence of their coexistence. Raman spectral studies have revealed the graphitic nature of the prepared carbon.

The comparison of the photocatalytic activity of the carbon and TiO₂ prepared together and carbon prepared over TiO₂ showed that the former method can improve the performance of the catalyst better than the latter. This can be attributed to larger co-existence of carbon and TiO₂ when they were prepared simultaneously. In addition carbon was playing a role of trapping the excited electrons as its Fermi level is of lower in energy compared to conduction band of TiO₂.

CHAPTER - 5

CHARACTERIZATION, PHOTOCATALYTIC AND ELECTROCHEMICAL STUDIES OF CdSnO₃ AND Cd₂SnO₄

5.1 INTRODUCTION

After the discovery of photocatalytic splitting of water using TiO₂ (Fujishima and Honda, 1972), considerable attempts have been made to produce hydrogen from water using solar light and semiconductor catalysts (Kato *et al.*, 2003). Photocatalysts are also equally exploited for the decontamination of polluted water since the method makes use of easily available solar energy (Blanco *et al.*, 2009; Ravelli *et al.*, 2009). Photocatalytic reactions are versatile since they can carry out both reduction and oxidation reactions simultaneously (Kamat, 2007). Various factors are hindering the efficiency of the photocatalytic processes. One of the factors is the recombination of the photoexcited electrons and holes which decreases the efficiency of the process. Photocatalysts with substantial activity like CdS suffer from photocorrosion where in they get oxidised by the holes created in their valence band upon excitation with light (Reber and Rusek, 1986). Another reason is the large bandgap of highly active photocatalysts like TiO₂. Solar light is composed of 7 % UV, 46 % visible and 47 % IR radiations respectively. Hence, practical solar photocatalytic applications require the catalyst to work on absorption of visible light.

Photocatalytic oxidation of organic pollutants is one of the Advanced Oxidation Processes (AOPs). The oxidation is carried out by the hydroxyl radicals created by the excited electrons and holes. These hydroxyl radicals can be created either by the

excited holes or the excited electrons depending on the potentials of the band edges of semiconductor. Hence, most of the semiconductors can be employed to degrade the pollutants on irradiation due to the creation of hydroxyl radicals.

On the other hand, the evolution of hydrogen from water is possible only by the reduction of H^+ ions by the excited electrons. The excited electrons need to be at a potential more negative (higher energy) than the hydrogen evolution reaction (0.0 V vs. NHE) to carry out these reactions. Hence, only semiconductors which have the conduction band position more negative than 0.0 V can carry out the hydrogen evolution reaction. Based on these points, a possible water splitting photocatalyst for hydrogen evolution should have a suitable bandgap to absorb light in the visible region and also a band potential suitable to reduce H^+ ions to H_2 (Viswanathan, 2003 & 2005).

The identification of a photocatalyst with higher quantum efficiency, long term stability and capable of functioning in UV and visible light still eludes the scientists even after nearly 40 years of research. Initial research during these years was focussed on TiO_2 and modifying TiO_2 to make it work using visible light (Fujishima *et al.*, 2000). Various approaches like doping with metal and non-metal ions, dye sensitization and coupling with lower bandgap semiconductors were considered (Notowny *et al.*, 2008; Zhang *et al.*, 2009) to make TiO_2 active in the visible light region. However, all these attempts have only yielded slight improvements in activity and have not yielded the desired results. Hence, recent attempts have been mostly focussed on identifying compounds with the desired properties rather than trying to modify TiO_2 (Kudo and Miseki, 2009; Maeda and Domen, 2010). These attempts

include studying the suitability of various materials for both pollutant degradation and water splitting reaction.

Various materials like $\text{Bi}_2\text{Fe}_4\text{O}_9$ (Sun *et al.*, 2009), CuInS_2 (Djellal *et al.*, 2009; Zhang *et al.*, 2009), SnWO_4 (Cho *et al.*, 2009), $(\text{SrTiO}_2)_{1-x}(\text{LaTiO}_2\text{N})_x$ (Luo *et al.*, 2008) have been studied as visible light photocatalysts. Among the various kinds of semiconductors like oxides, sulphides and nitrides, oxides are the most stable compounds. In addition, the preparation methods of oxides are easier and economical compared to the sulphides and nitrides. Oxide semiconductors contain valence bands composed of *d*-orbitals of metal ions and *p*-orbitals of oxide ions whereas the conduction bands are composed of *s*-orbitals and *p*-orbitals of metal ions. Materials containing elements with completely filled *d*-orbitals (d^{10}) have VB edge at higher energy and hence small bandgap (Sato *et al.*, 2001).

As both cadmium and tin have d^{10} configuration in their outer orbitals, oxides based on them are expected to have a smaller bandgap. Such compounds are expected to be active as visible light photocatalysts. CdSnO_3 and Cd_2SnO_4 are the well known oxides of cadmium and tin. Cd_2SnO_4 is being applied as transparent conducting oxide (TCO) in CdS/CdTe solar cells (Wu *et al.*, 1996; Zhou *et al.*, 2007). CdSnO_3 is also being studied as a sensor for ethanol, ammonia and butane (Liu *et al.*, 2005; Wang *et al.*, 2003; Zhang *et al.*, 1996).

Both CdSnO_3 and Cd_2SnO_4 exist in two phases. CdSnO_3 exists in orthorhombic and rhombohedral phases whereas Cd_2SnO_4 exists in orthorhombic and cubic phases. Different phases of the compounds are known to have completely different properties towards photocatalytic reactions. Hence, the properties of cadmium stannates studied

in this work are that of rhombohedral phase of CdSnO_3 and orthorhombic phase of Cd_2SnO_4 . Other phases of cadmium stannates namely orthorhombic phase of CdSnO_3 and cubic phase of Cd_2SnO_4 may have different photocatalytic properties.

The current work involves the preparation of single phase of CdSnO_3 and Cd_2SnO_4 and studying the photocatalytic activities of these catalysts using *p*-chlorophenol as a model pollutant. The studies were carried out both in the UV-visible and visible light and the degradation were monitored. Chemical Oxygen Demand (COD) analysis was performed to study the extent to which the *p*-chlorophenol was oxidized to CO_2 . Furthermore, the ability of these catalysts to split water to produce hydrogen was also examined. Impedance measurements were made on the prepared samples and the flatband potentials were determined from Mott-Schottky plots to find out their ability to evolve H_2 .

5.2 RESULTS AND DISCUSSION

5.2.1 X-ray diffraction studies

X-ray diffraction studies were carried out on the prepared powder samples to determine the phase purity of the samples. Fig. 5.1 shows the XRD pattern of the prepared CdSnO_3 and it was found to be matching with that of rhombohedral CdSnO_3 phase (JCPDS No. 880287). The peaks were sharp indicating the highly crystalline nature of the powders (Presence of peaks other than CdSnO_3 was not observed in the XRD patterns). From the XRD patterns of the prepared Cd_2SnO_4 shown in Fig. 5.2, it was found to be pure orthorhombic phase (JCPDS No. 801467).

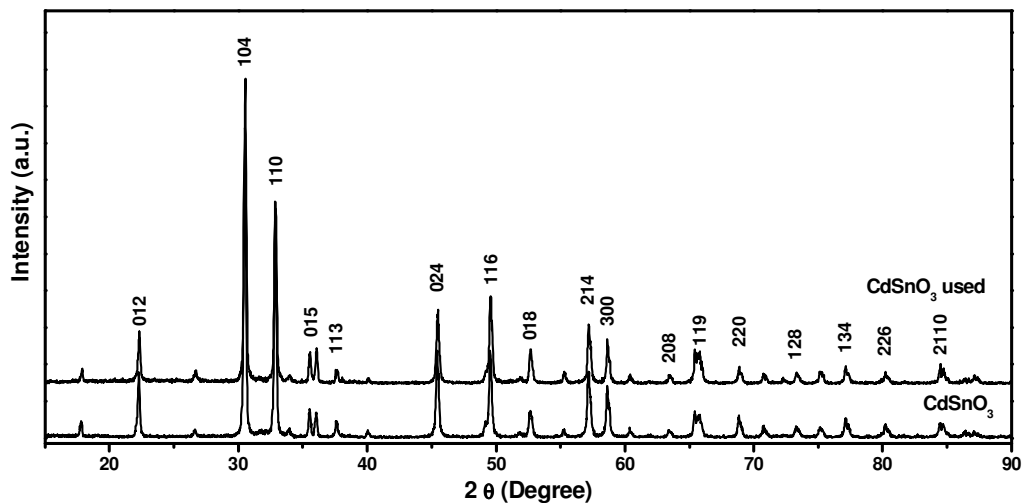


Fig. 5.1. X-ray diffraction patterns of CdSnO₃ before and after using for photocatalytic degradation of *p*-chlorophenol reaction under UV-visible irradiation

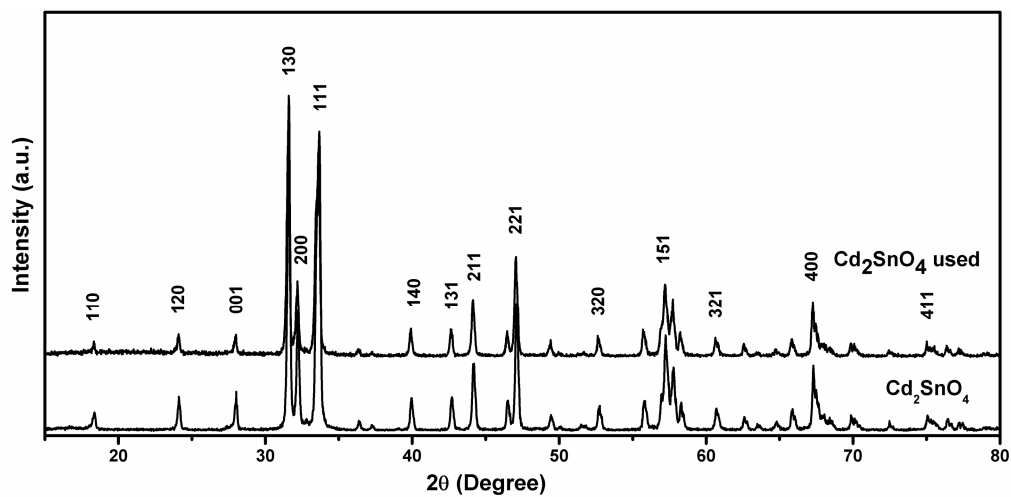


Fig. 5.2. X-ray diffraction patterns of Cd₂SnO₄ before and after using for photocatalytic degradation of *p*-chlorophenol reaction under UV-visible irradiation

Crystallite sizes (D) of the samples were calculated using the Debye-Scherrer equation, $D = \frac{0.89\lambda}{\beta \cos \theta}$ where λ is the wavelength of the radiation used (1.54 nm for Cu K α), β is the full width at half maximum (FWHM) and θ is the diffraction angle. The θ and FWHM values were converted from degrees to radians for the calculation of crystallite size. Crystallite sizes of CdSnO₃ and Cd₂SnO₄ calculated from the XRD pattern based on Debye-Scherrer equation were found to be 45 nm and 47 nm respectively.

XRD patterns of the both CdSnO₃ (Fig. 5.1) and Cd₂SnO₄ (Fig. 5.2) were recorded after the photocatalytic degradation studies of *p*-chlorophenol under UV-visible light irradiation. It was observed that there were no new peaks or changes in intensity of the peaks in the case of samples used for the photocatalytic reactions. This shows that the catalyst was stable under the conditions of the photocatalytic measurements.

5.2.2 Diffuse Reflectance UV-visible spectral studies

The diffuse reflectance UV-visible spectrum of CdSnO₃ is given in Fig. 5.3. The CdSnO₃ powders (cream in colour) showed absorption mostly in the UV region. The absorption onset was at 415 nm. This corresponds to a bandgap of 3.0 eV. In the case of Cd₂SnO₄ (Fig. 5.4), the sample was bright yellow in colour and the absorption onset was observed at 532 nm corresponding to a bandgap value of 2.3 eV. These bandgap values are in agreement with the previously reported values for CdSnO₃ and Cd₂SnO₄ (Fard *et al.*, 1983). UV-visible DR spectrum of Cd₂SnO₄ and CdSnO₃ were taken after using for the photocatalytic degradation reaction of *p*-chlorophenol under

UV-visible irradiation. Both CdSnO_3 (Fig. 5.3) and Cd_2SnO_4 (Fig. 5.4) did not show any change in absorption compared to the unused samples. This showed that both CdSnO_3 and Cd_2SnO_4 were stable and retained their absorption properties under the conditions of photocatalytic measurements.

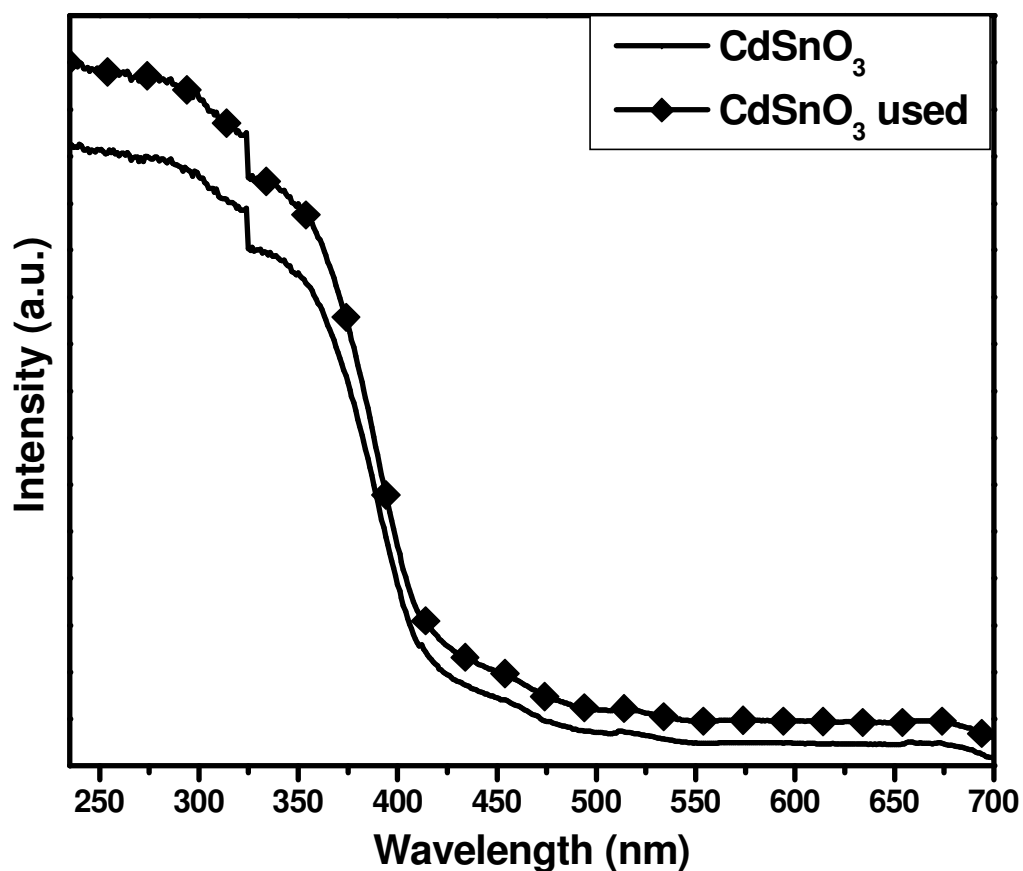


Fig. 5.3. Diffuse reflectance UV-visible spectra of CdSnO_3 before and after using for photocatalytic degradation of *p*-chlorophenol reaction under UV-visible irradiation

5.2.3 Scanning Electron Microscopic (SEM) analysis

Scanning Electron Microscopic (SEM) images of CdSnO_3 , given in Fig. 5.5 revealed particles with sizes ranging from 0.5 μm to 5 μm . There seems to be a very large

distribution of particle sizes and the particles are in an agglomerated state. In addition, the particles look like flakes and don't seem to have any uniform shape. On the other hand, images of Cd_2SnO_4 (Fig. 5.6) showed agglomerates of smaller particles having uniform size. The sizes of the particles were around $0.5 \mu\text{m}$ and seem to have an oval shape and their agglomerates have resulted in large masses with pores.

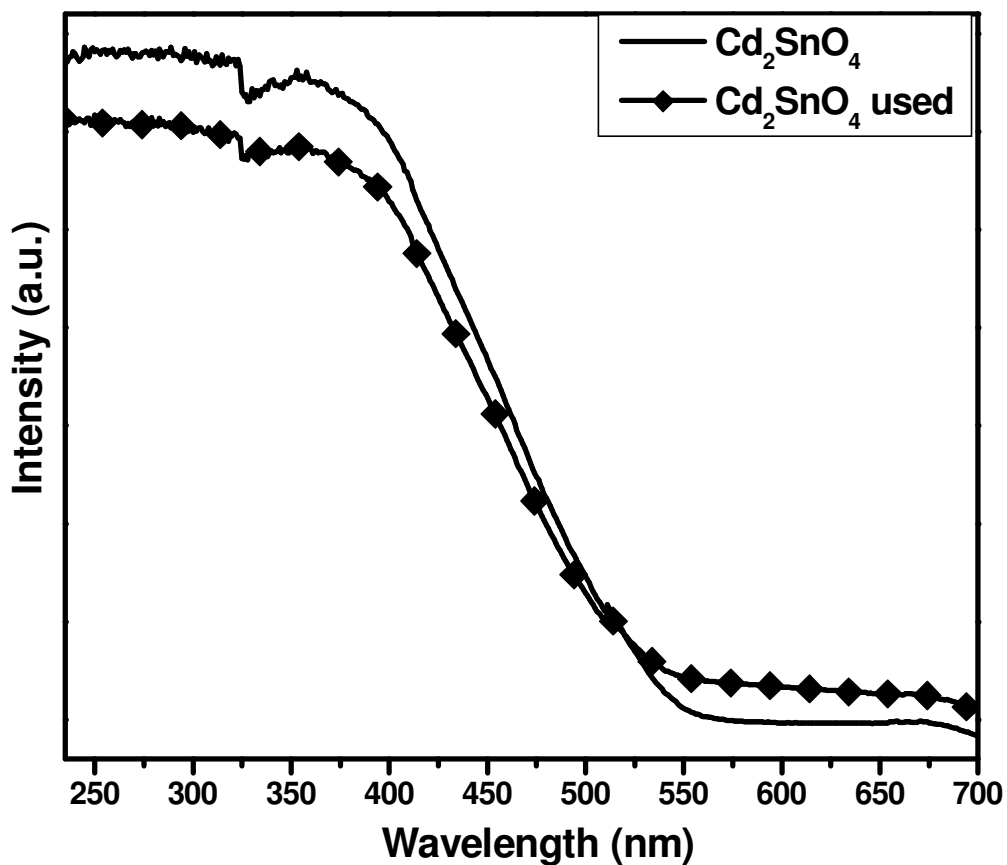


Fig. 5.4. Diffuse reflectance UV-visible spectra of Cd_2SnO_4 before and after using for photocatalytic degradation of *p*-chlorophenol reaction under UV-visible irradiation

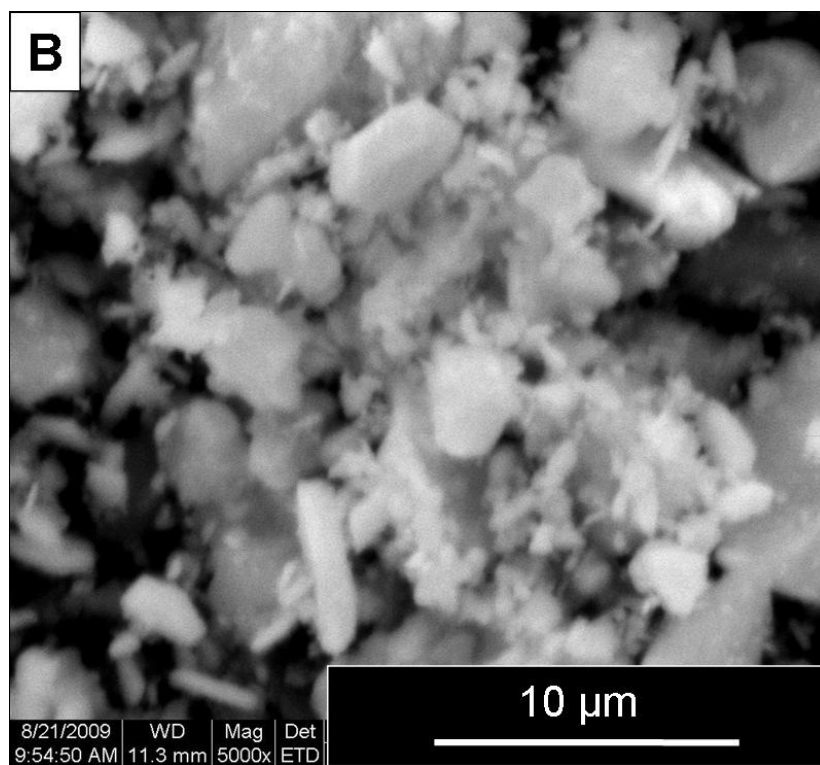
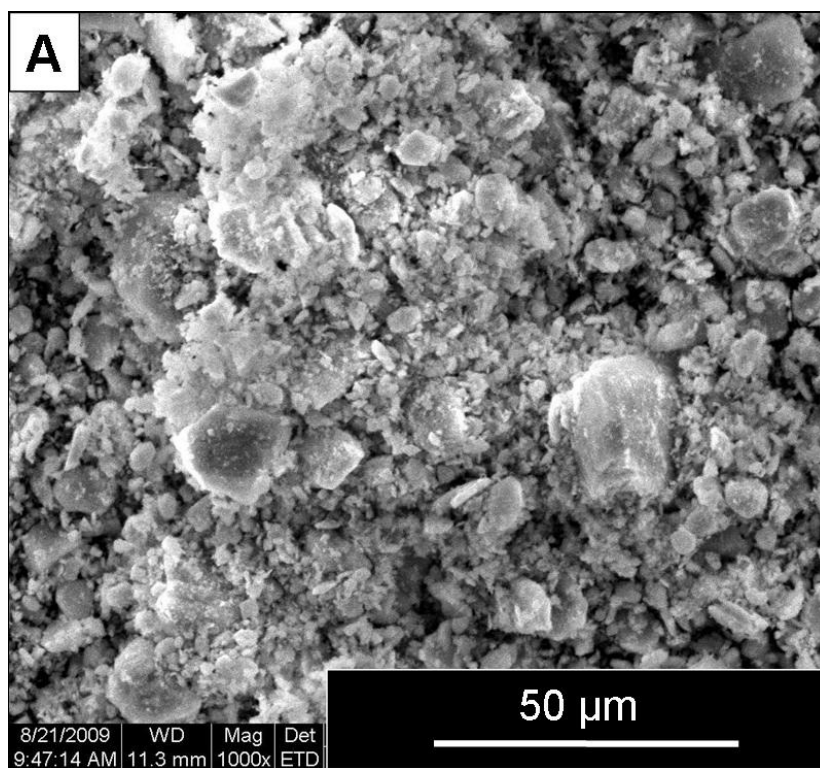


Fig. 5.5. SEM images of rhombohedral CdSnO_3 (A) 1000 magnification and (B) 5000 magnification

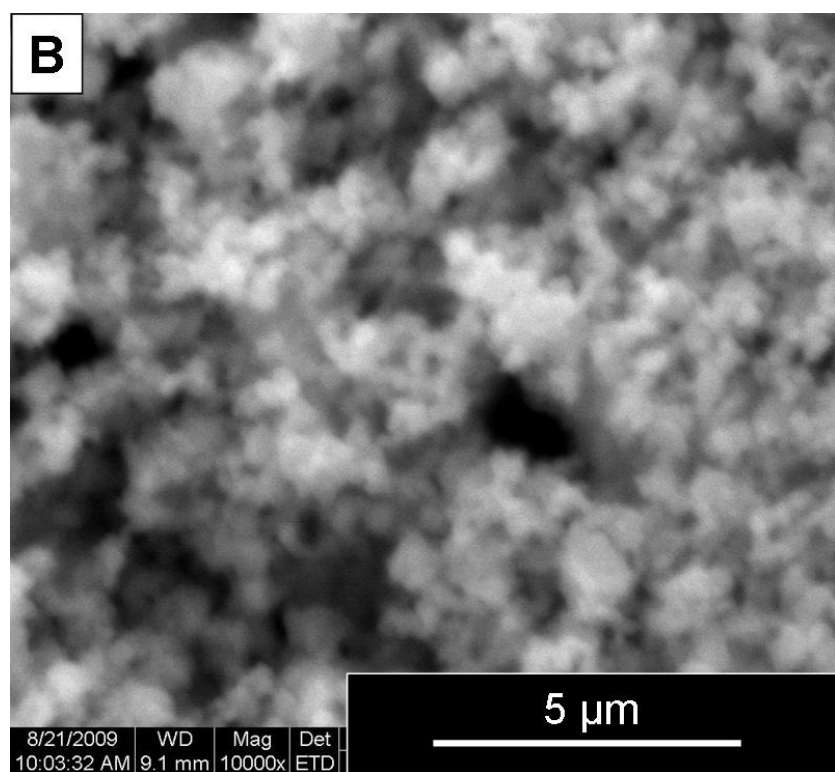
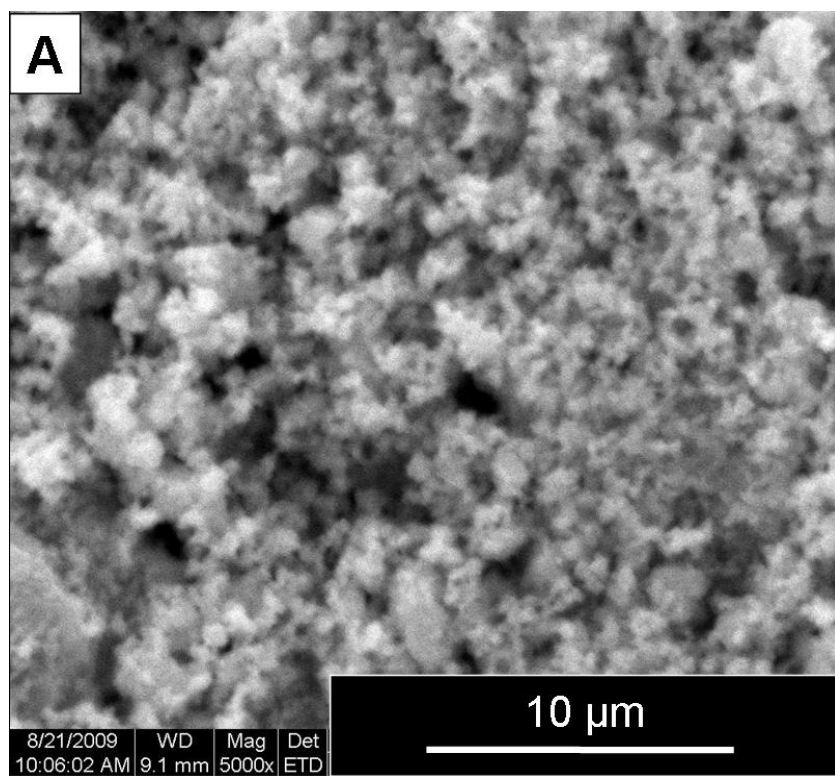


Fig. 5.6. SEM images of orthorhombic Cd_2SnO_4 (A) 5000 magnification and (B) 10000 magnification

5.2.4 Mott-Schottky analysis

Electrochemical impedance spectroscopy (EIS) is an effective tool for probing the features of surface-modified electrodes and was further employed to analyze the semiconducting properties of the cadmium stannate electrodes. The flat-band potential (E_{fb}) is the potential value which must be applied to the semiconductor electrode, relative to the reference electrode, to flatten the band bending due to the difference in the Fermi levels between the electrode and electrolyte. Generally, the E_{fb} values were determined by measuring the capacitance (C_{SC}) of the electrode/electrolyte interface at different electrode potentials (V) using the Mott-Schottky equation. The system's capacitance, C was then calculated by fitting the obtained values using the equivalent circuit shown in Fig. 5.7. The Mott-Schottky plots were linear in the potential range from 0 to + 0.9 V vs. Ag/AgCl.

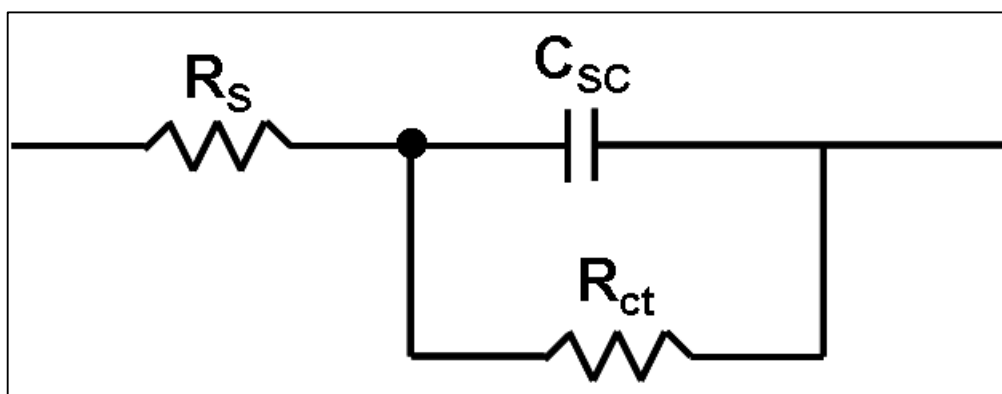


Fig. 5.7. Equivalent circuit used for curve fitting of $CdSnO_3$ and Cd_2SnO_4 (R_s , solution resistance; C_{sc} , space charge capacitance; R_{ct} , charge transfer resistance)

According to the Mott-Schottky analysis, the space charge capacitance, C_{sc} of the doped semiconductor in the depletion zone, valid under biasing conditions, is expressed as

$$\frac{1}{C_{sc}^2} = \frac{2}{e\epsilon\epsilon_0 N_D} \left(U - E_{fb} - \frac{k_B T}{e} \right)$$

where e is the electronic charge, N_D is the dopant (donor) density, ϵ_0 is the permittivity of free space, ϵ the dielectric constant of the anodic film, E_{fb} is the flat band potential, and k_B is the Boltzmann constant. In the case of a linear MS plot, the flat band potential can be readily determined from the x -intercept when $\frac{1}{C_{sc}^2} = 0$. The flat band potentials for the Cd_2SnO_4 and $CdSnO_3$ (Figs. 5.8 and 5.9) were found to be 0.31 V and 0.23 V vs. Ag/AgCl electrode respectively.

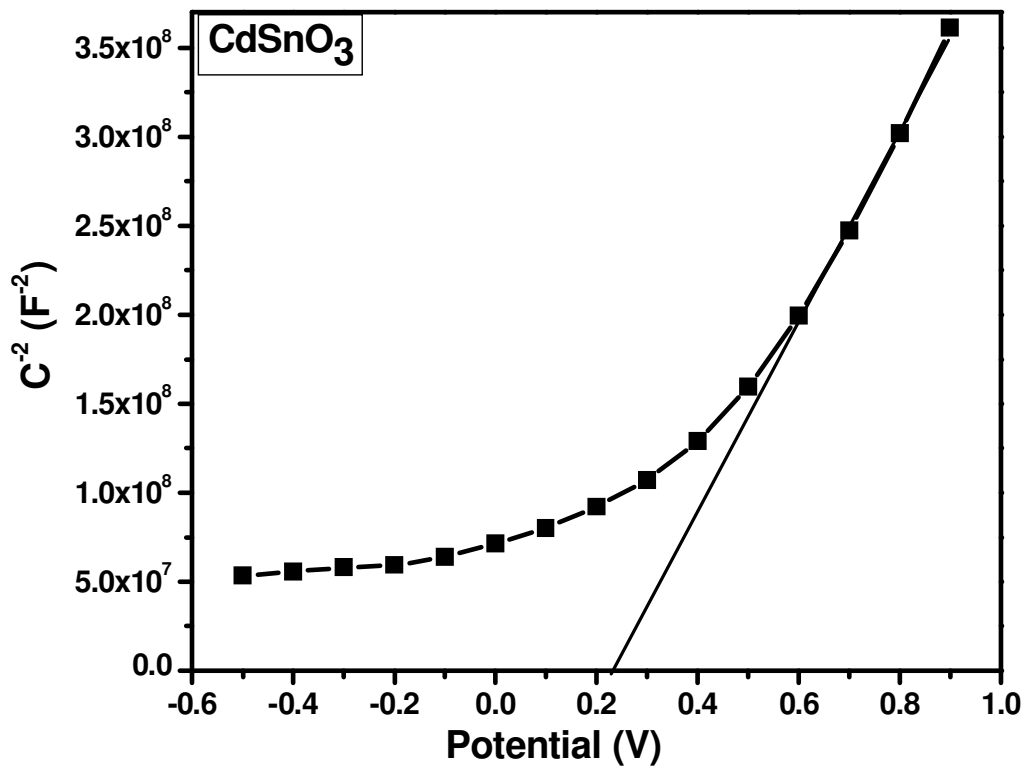


Fig. 5.8. Mott-Schottky plot of rhombohedral $CdSnO_3$ film coated on Ti sheets measured in 0.5 M Na_2SO_4 (pH 7.0) electrolyte under dark conditions in the frequency range of 10^{-2} to 10^5 Hz with amplitude of 5 mV.

This corresponds to 0.51 V and 0.43 V vs. NHE for Cd_2SnO_4 and CdSnO_3 respectively. For a semiconductor to reduce H^+ ions by photocatalytic means, it should have its conduction band potential at an energy higher than 0.0 V ($E_{\text{H}_2/2\text{H}^+}^0 = 0$). As both CdSnO_3 and Cd_2SnO_4 have positive flat band potential values, they will not be able to evolve hydrogen by photosplitting water.

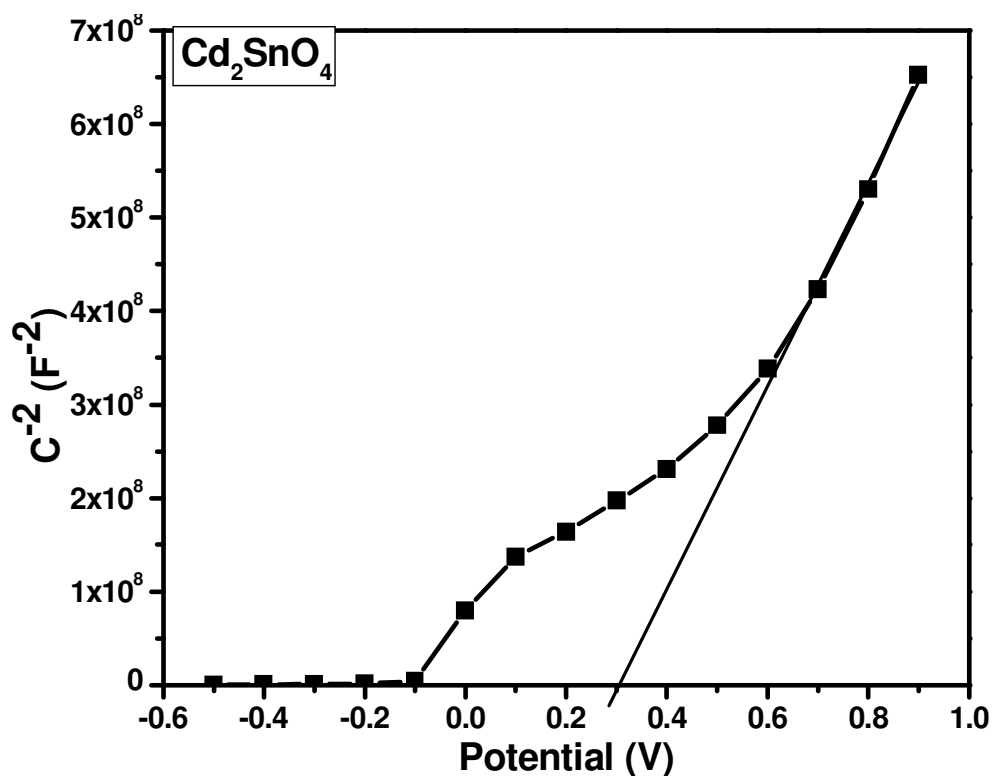


Fig. 5.9. Mott-Schottky plot of orthorhombic Cd_2SnO_4 film coated on Ti sheets measured in 0.5 M Na_2SO_4 (pH 7.0) electrolyte under dark conditions in the frequency range of 10^{-2} to 10^5 Hz with amplitude of 5 mV.

5.2.5 Photocatalytic degradation of *p*-chlorophenol studies

Photocatalytic activities of the cadmium stannates were studied using *p*-chlorophenol as the model pollutant. The activity was studied using a mercury lamp, where light of

wavelength 200-800 nm was used to irradiate the catalyst. In addition, experiments were also carried out with visible light ($\lambda > 420$ nm) alone. The photocatalytic degradation of *p*-chlorophenol for CdSnO₃ and Cd₂SnO₄ are given in Table 5.1. The results showed that CdSnO₃ was capable of degrading 94.5 % of *p*-chlorophenol in UV-Visible light whereas CdSnO₃ was inactive in visible light. This is well in agreement with the diffuse reflectance UV-Visible spectrum of CdSnO₃, where in no absorption in the visible region is observed. However, Cd₂SnO₄ was found to be active in both UV-Visible and visible light. The activity of Cd₂SnO₄ in UV-Visible light was significantly higher than that in visible light. The higher activity in UV-Visible light compared to that of the visible light might be due to the additional photons of UV light in addition to visible light.

Table 5.1. Percentage decrease in the concentration of *p*-chlorophenol using cadmium stannates as photocatalyst estimated by UV-Visible spectrophotometry and COD analysis

	CdSnO ₃		Cd ₂ SnO ₄	
	UV-Visible	Visible	UV-Visible	Visible
% Degradation based on absorbance	94.5	0.0	75.8	24.9
% Decrease in COD	86.6	0.0	68.4	18.7

5.2.6 Chemical Oxygen Demand (COD) analysis

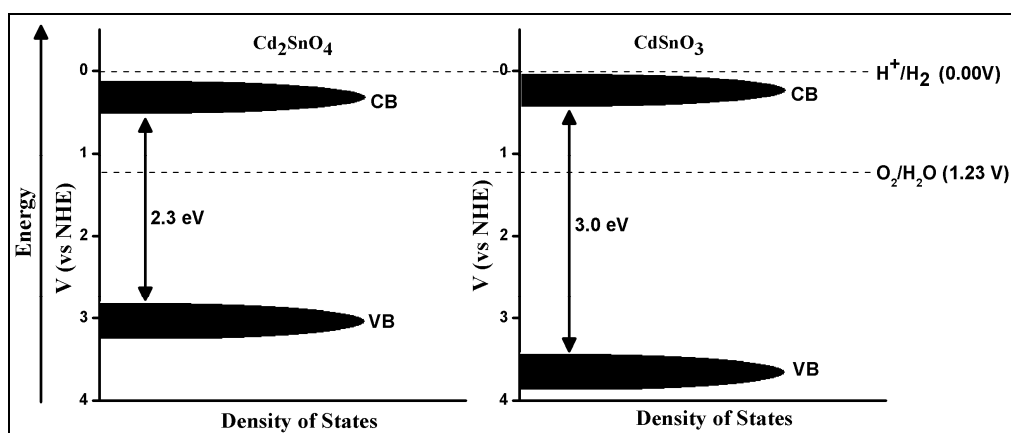
Absorbance of *p*-chlorophenol at 223 nm is due to the functional groups. Any change in functional groups without the ring opening will lead to a decrease in absorbance at

223 nm. Various degradation products of 4-chlorocatechol, hydroquinone and benzoquinone have comparably smaller absorption than *p*-chlorophenol at 223 nm. Thus the change in absorbance at 223 nm is not an exact measure of the degradation of *p*-chlorophenol (Kang *et al.*, 1999; Titus *et al.*, 2004). In order to confirm the complete degradation of *p*-chlorophenol, samples from the photocatalytic studies were analysed for their Chemical Oxygen Demand (COD). COD gives the amount of species which can be oxidized in the sample taken. Hence, decrease in COD is a measure of complete oxidation of the *p*-chlorophenol. COD of the blank solution was also analyzed to eliminate the interference due to the species other than *p*-chlorophenol. The results obtained based on COD analysis were given in Table 5.1. These results showed a considerable deviation from the decrease in concentration based on COD and absorbance measurements. Another interesting observation was that the percent deviations in COD from absorbance results were higher in case of samples with low photocatalytic activity. In the case of samples with higher photocatalytic activity, the deviations were less. This is due to the fact that it is easier to oxidize the intermediate compounds compared to the difficult step of opening the aromatic ring by oxidation (Kang *et al.*, 1999; Titus *et al.*, 2004).

5.2.7 Photocatalytic water splitting studies

In order to find out the hydrogen production abilities of the cadmium stannates, photocatalytic water splitting studies were carried out. In these studies, a mixture of water and methanol was used so that methanol will get oxidized by the holes from the valence band. Hence, only hydrogen evolution will happen by the reduction of H⁺ by the electrons from the valence band, and the volume of evolved gas can be easily determined. As we have mentioned earlier in Mott-Schottky plot studies, these

catalysts have their conduction band potentials lower in energy than the hydrogen evolution potentials. Hence they will not be able to evolve hydrogen. During the photocatalytic hydrogen evolution experiments no gas evolution was observed on CdSnO_3 and Cd_2SnO_4 . No gas was evolved during both UV-Visible and visible light irradiation. These results of the hydrogen evolution studies were in agreement with band potentials determined by the Mott-Schottky plots (as both CdSnO_3 and Cd_2SnO_4 did not evolve hydrogen during the irradiation of the catalysts). Scheme 5.1 illustrates the band positions of CdSnO_3 and Cd_2SnO_4 with respect to hydrogen and oxygen evolution potentials.



Scheme 5.1. Schematic diagram of band positions (vs. NHE) of CdSnO_3 and Cd_2SnO_4 with respect to hydrogen and oxygen evolution potentials.

5.3 CONCLUSIONS

The essential conclusions that follow from this study include

- i) Rhombohedral CdSnO_3 and orthorhombic Cd_2SnO_4 prepared by co-precipitation method showed bandgaps of 3.0 and 2.3 eV respectively.

- ii) Photocatalytic degradation of *p*-chlorophenol studies showed that both catalysts were active in UV-Visible radiation whereas, only Cd₂SnO₄ was found to be photoactive in visible radiation ($\lambda > 420$ nm).
- iii) Mott-schottky plots showed flat band potentials of 0.43 and 0.51 V (vs. NHE) for CdSnO₃ and Cd₂SnO₄ respectively.
- iv) Water splitting studies showed no hydrogen evolution in accordance with measured flat band potentials.

CHAPTER – 6

CHARACTERIZATION AND CO OXIDATION ACTIVITY OF Au/TiO₂

6.1 INTRODUCTION

Different allotropic forms of a compound exhibit variations in their properties. One of the compounds which display such a behaviour is TiO₂. The three different allotropic forms of TiO₂ namely anatase, rutile (both tetragonal) and brookite (orthorhombic) have different photocatalytic properties because of the variation in the band gaps (Koelsch *et al.*, 2002; Paola *et al.*, 2009; Park *et al.*, 2009). The band gaps of anatase, brookite and rutile are 3.05, 3.26 and 2.98 eV respectively. In addition, the potential of the bottom of the conduction band of anatase, rutile and brookite are at -0.45, -0.46 and -0.37 V vs. NHE respectively. The variation in the photocatalytic properties of these allotropic forms of TiO₂ have been explained successfully based on the above points.

Another research area where TiO₂ has been widely used is as support for Au nanoparticle in CO oxidation. It is also known that brookite and anatase transform to the rutile phase at 1073 K and 1188 K respectively. Structurally brookite is loose (unit cell volume 257.4 Å³, JCPDS file no. 761936) compared to anatase (136.2 Å³ JCPDS file no 894921) and rutile (62.1 Å³, JCPDS file no. 894920), while the surface enthalpy follows the order rutile (2.2 ± 0.2 J m⁻²) > brookite (1.0 ± 0.2 J m⁻²) > anatase (0.4 ± 0.2 J m⁻²) (Ranade *et al.*, 2002). These variations in the properties of

the allotropic forms are expected to influence the catalytic activity, when they are used as support for gold.

Meanwhile, gold which was considered as catalytically inactive has been found to be active when present in nanometer sized particles (Haruta *et al.*, 1987). Gold when supported on reducing supports is active towards oxidation of CO (Haruta, 1997). Nanoparticles of gold (of same size) were supported on different oxides and studied for the catalytic oxidation of CO. Among TiO₂, Al₂O₃, CeO₂, ZnO, SiO₂, ZrO₂, and Co₃O₄ as supports TiO₂, Co₃O₄ and Al₂O₃ were found to be the most active (Comotti *et al.*, 2006; Weiher *et al.*, 2006; Wolf and Schuth, 2002). Comotti *et al.*, (2006) have reported the CO oxidation activity of samples prepared by colloidal deposition method, where pre-synthesized gold nanoparticles of uniform size were deposited on different supports like TiO₂, Al₂O₃, ZnO and ZrO₂. According to their report, the activity followed the order TiO₂ > Al₂O₃ > ZnO > ZrO₂ and the support played a significant role in deciding the CO oxidation activity of the catalyst.

There are other factors which have been reported to influence the catalytic activity. They are the size of the gold particles, oxidation state (cationic sites) of gold species (Guzman and Gates, 2004; Wu *et al.*, 2002), and the preparation method (Fu *et al.*, 2005; Haruta, 2002; Lopez *et al.*, 2004; Manzoli *et al.*, 2003; Valden *et al.*, 1998). In addition, uncoordinated step and corner atoms (Lopez and Norskov, 2002; Meyer *et al.*, 2004; Mills *et al.*, 2002; Mavrikakis *et al.*, 2000), metal-support interface area (Bond and Thompson, 2001; Haruta, 1997; Pietron *et al.*, 2002; Schubert *et al.*, 2001), and the charge transfer from the support to the metal (Fu *et al.*, 2003; Sanchez *et al.*, 1999) are also reported to influence the activity.

Most of the CO oxidation studies were carried out using anatase and rutile phases of TiO₂ as support for Au and the results indicated that anatase was a better support than rutile. Further, the thermal stability of rutile supported catalyst was less compared to that of anatase. Studies using brookite as support for gold were not carried out extensively so far.

Recently, it was reported that the brookite phase was more active towards CO oxidation than anatase and rutile forms of TiO₂ (Yan *et al.*, 2004 and 2005). In addition, the brookite phase as support was described to be more stable at higher temperatures than anatase and rutile forms of TiO₂. The observed thermal stability of brookite was attributed to the better ability of the brookite to prevent the sintering of the gold nanoparticles compared to the anatase and rutile forms of TiO₂. However, the report by Yan *et al.*, (2004 and 2005) was based on the results from the deposition-precipitation method, where in the support considerably influenced the particle size and shape of the particles of Au. This resulted in different sizes and shapes of gold particles on different supports though they were prepared by the same method. It was reported by Wolf and Schuth (2002) that, for samples prepared by deposition-precipitation method, the activity towards CO oxidation followed the order Co₃O₄ > TiO₂ > Al₂O₃ > ZrO₂ >> SiO₂. In this report, the gold loadings were different for the different catalysts. In addition, for a particular support, the best catalyst was obtained by varying the pH of deposition of Au.

One of the reasons mentioned for this difference in catalytic activity with different supports was the point of zero charge (PZC) of the catalysts. It was mentioned by Wolf and Schuth (2002) that irrespective of the nature of the support, activity of the catalysts can be modified by changing the preparation conditions (like pH) depending

on the PZC of the support as long as the PZC is in range of 6-9. Furthermore, the reproducibility of the results from catalysts prepared by deposition-precipitation was not good. With the different sizes and shapes of gold on different supports, the variation in the activity of the different catalysts cannot be attributed specifically to the interaction between the support and gold. The number of active sites on the gold particles will be different with different sizes and shapes of gold particles. In such a case, the difference in activity of gold due to its interaction with the support cannot be studied.

There are various methods which were adopted to prepare supported gold catalysts. Among them, deposition-precipitation, co-precipitation and phosphine grafting were found to give highly active catalysts whereas conventional deposition methods like wet impregnation, electrostatic adsorption led to catalysts with least activity (Arena *et al.*, 2006). Among the various methods described for the preparation of supported gold nanoparticles described, deposition precipitation methods were reported to yield highly active catalysts (Arena *et al.*, 2006; Dimitratos *et al.*, 2006; Grisel *et al.*, 2000). Deposition-precipitation method gave better catalysts than those prepared by impregnation, chemical reduction, co-precipitation, incipient wetness and combustion methods. However, in samples prepared by deposition precipitation method, the sizes of gold particles on different supports are not always uniform and hence a study of the influence of the support on the catalytic activity is difficult.

In consideration of all these aspects catalysts in the present study were prepared by sol deposition method where gold particles with same size and shaped were prepared separately and then deposited on the support. This method leads to uniform sizes of gold nanoparticles irrespective of the nature of the support. Furthermore, this method

leads to uniform weight loading of gold on the various supports. This will make comparison of the influence of the support on the catalytic activity easier. Comotti *et al.*, (2006) observed that even though the particle sizes of gold were the same, the gold particles have different types of faceting on different supports. With the catalysts prepared by this method, the difference in activity can be attributed solely to the interaction between the support and the gold.

The issues on which the literature is silent are: (i) Is brookite also similar to anatase as a support for metals? (ii) If it were to be so, how does the brookite-metal interaction differ from that of anatase or rutile-metal interaction? (iii) If brookite-metal interaction were to be responsible for the retardation of agglomeration of metal particles, then what will be the effect of brookite on bigger metallic particles? and (iv) has the method of preparation of brookite plays any role in the properties exhibited by the systems developed?

In order to obtain appropriate clues to these questions, brookite and gold supported on brookite were prepared by two different methods namely sol deposition method and deposition-precipitation (DP) method as adopted by Yan *et al.*, (2004 and 2005). Similar gold loadings were maintained on both sol deposition and deposition-precipitation methods. Both P25 and brookite were used as supports for gold to study the influence of the support. The catalytic activity towards CO oxidation was measured under similar condition for both the catalysts.

The difference in catalytic activity before and after calcination of the various samples can be used to find out their thermal stability. In the present study, the thermal stability of the brookite, P25 (anatase + rutile) as well as another TiO₂ (mixture of

anatase and brookite) has also been studied by measuring the activity of the catalyst before and after calcination of the catalyst at higher temperature (673 K) in air.

6.2 RESULTS

6.2.1 X-ray diffraction studies

Anatase phase of TiO₂ (JCPDS file no. 894921) has its diffraction peaks at 2 θ values of 25.4, 37.9, 38.6, 48.2, 54.0, 55.2, 62.8, 70.5, and 75.2. Brookite phase of TiO₂ (JCPDS file no. 761936) will give diffraction peaks at 2 θ values of 25.3, 30.8, 36.2, 37.2, 40.1, 42.3, 49.0, 49.1, 54.3, 55.1 and 62.0. X-ray diffraction analysis shows the presence of 100 % brookite TiO₂ phase in case of BRT4 (Fig. 6.1). 55 % anatase TiO₂ and 45 % brookite TiO₂ were observed in the case of BRT3 samples (Fig. 6.1). BET surface area analyses of BRT4 and BRT3 showed the specific surface area to be 114 m²/g and 197 m²/g respectively (Table 6.1). BET analysis of BRT3 shows a Type V isotherm indicating mesoporous nature of BRT3.

In order to study the changes in the crystallinity and phase composition of the catalysts, XRD measurements were made for the catalysts before and after the catalytic measurements. XRD patterns of Au/BRT4 samples (Fig. 6.2) show the peaks corresponding to both Au (JCPDS No. 893697) and brookite TiO₂ in both the used and fresh catalysts. Peaks corresponding to brookite TiO₂ in the used sample remained the same in intensity as that in the fresh sample. No additional peaks corresponding to other phases of TiO₂ were observed in XRD patterns of the used sample. However, the peaks corresponding to gold show a considerable increase in

intensity in used catalyst. This increase in intensity can be clearly observed in the 111 and 200 peaks of Au.

From the XRD patterns of the Au/P25 sample (Fig. 6.3), it can be observed that no peaks corresponding to gold were observed in both the used and fresh sample. This lack of Au peaks may be due to the uniform distribution of gold nanoparticles throughout the surface of P25 TiO₂. Peaks corresponding to anatase and rutile were observed, which is in agreement with the composition of P25 TiO₂ given by the manufacturers. Furthermore, no additional peaks corresponding to other phases of TiO₂ were observed in the sample used for the catalytic measurements.

Table 6.1. Surface area and crystalline phase composition of the various supports

Sample	Specific surface area (m ² /g)	Crystalline phase		
		% Anatase	% Brookite	% Rutile
BRT4	114	-	100	-
BRT3	197	55	45	-
Degussa P25	49*	75*	-	25*

* - values given by the manufacturer

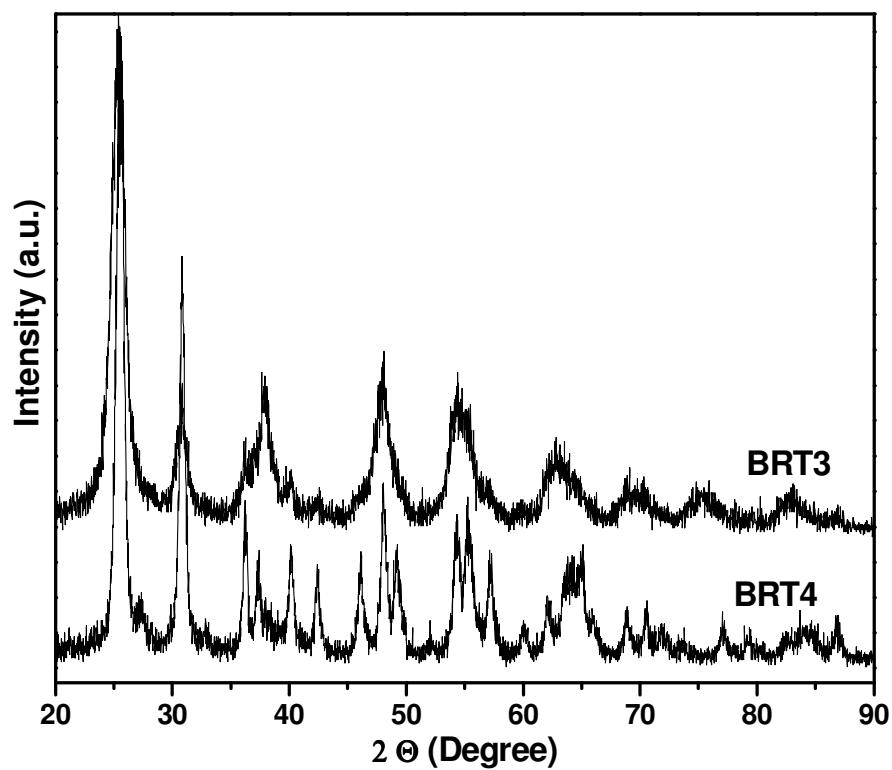


Fig. 6.1. XRD patterns of BRT4 and BRT3 samples

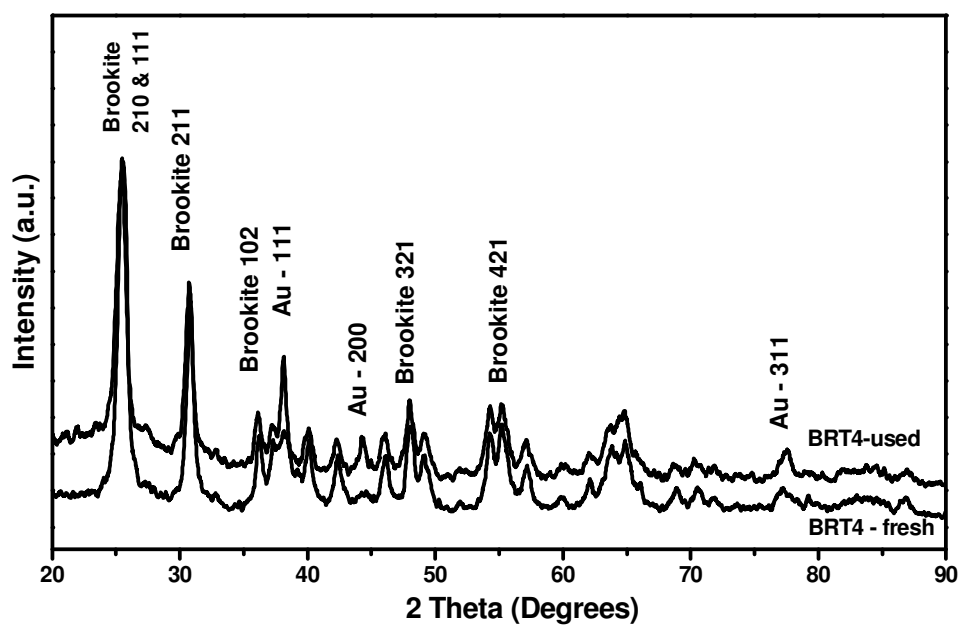


Fig. 6.2. XRD patterns of Au/BRT4 catalysts before and after catalytic measurements

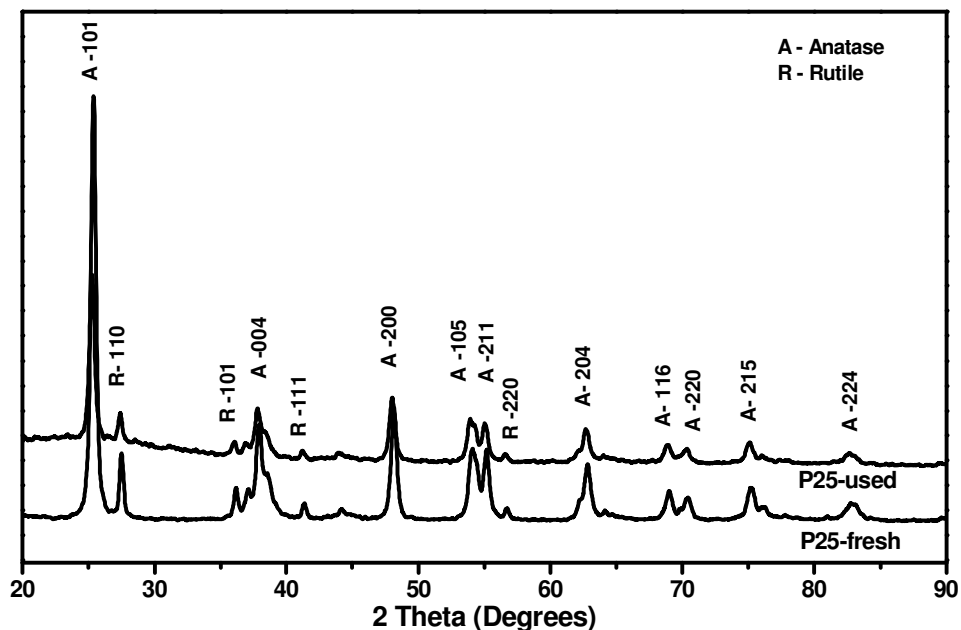


Fig. 6.3. XRD patterns of Au/P25 catalysts before and after catalytic measurements

6.2.2 Inductively coupled plasma – optical emission spectroscopy analysis

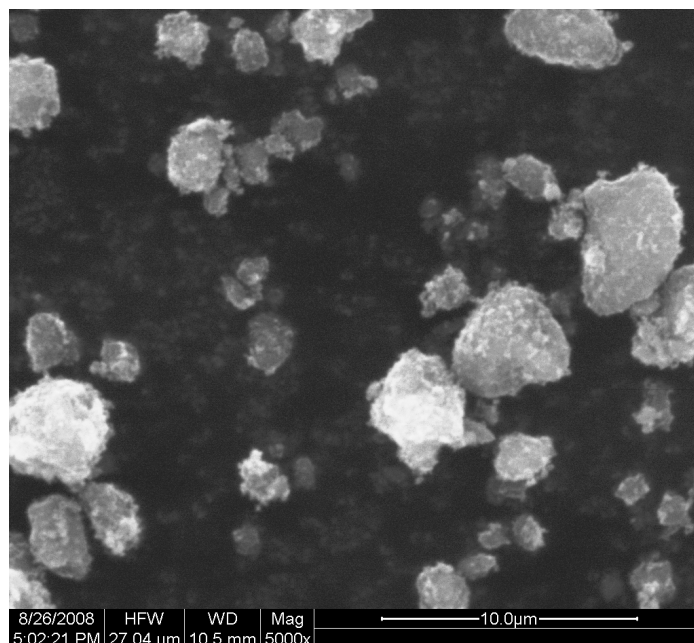
Inductively coupled plasma – optical emission spectroscopic (ICP-OES) analysis was carried out to find out the actual amount of gold loaded on TiO_2 . The ICP analysis data for gold loading on the catalysts are given in Table 6.2. For the sol derived samples, all the gold was loaded on TiO_2 surface. The observed loading by ICP is slightly higher than the calculated loading which may be due to experimental errors. For the deposition-precipitation (DP) derived samples, the gold loading is 2.2 wt % for both P25 and BRT4 samples.

Table 6.2. Calculated and actual loading of gold by ICP analysis for the various Au/TiO₂ samples

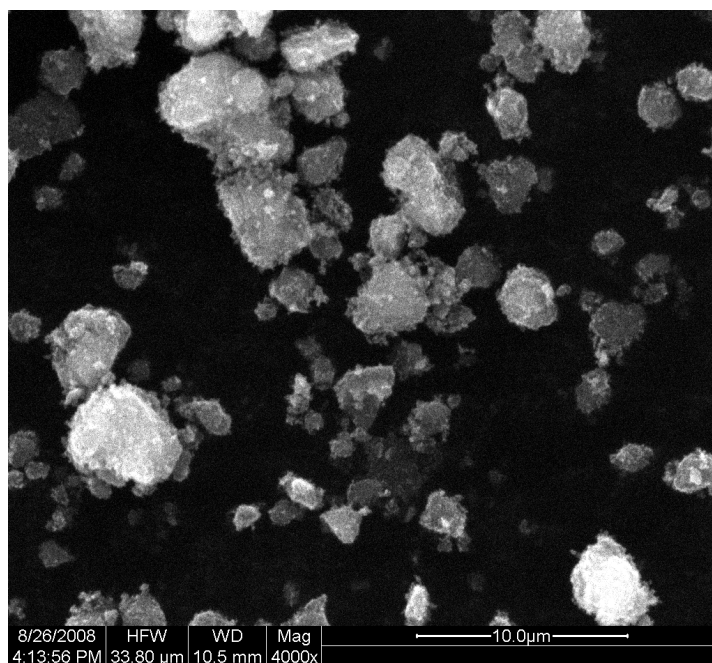
Catalyst	Expected Au loading (%)	% Au loading based on ICP
Au/BRT4-Sol	2.0	2.22
Au/P25-Sol	2.0	2.15
Au/BRT3-Sol	2.0	2.22
Au/BRT4-DP	2.2	Not available
Au/P25-DP	2.2	Not available

6.2.3 Scanning Electron Microscopy analysis:

SEM images of the Au/BRT4 and Au/P25 catalysts prepared by sol deposition method are given in Fig. 6.4 and Fig 6.5 respectively. The size of gold particle is too small to be identified by SEM analysis. Overall the images show highly agglomerated particles with porous structure. The agglomerates in the fresh state were of 1-5 μm in size. The sizes of the aggregates were larger in the catalysts used for the reaction especially in the case of Au/P25 samples. This can be attributed to the hydraulic pressing of the catalysts before using for the catalytic reaction.

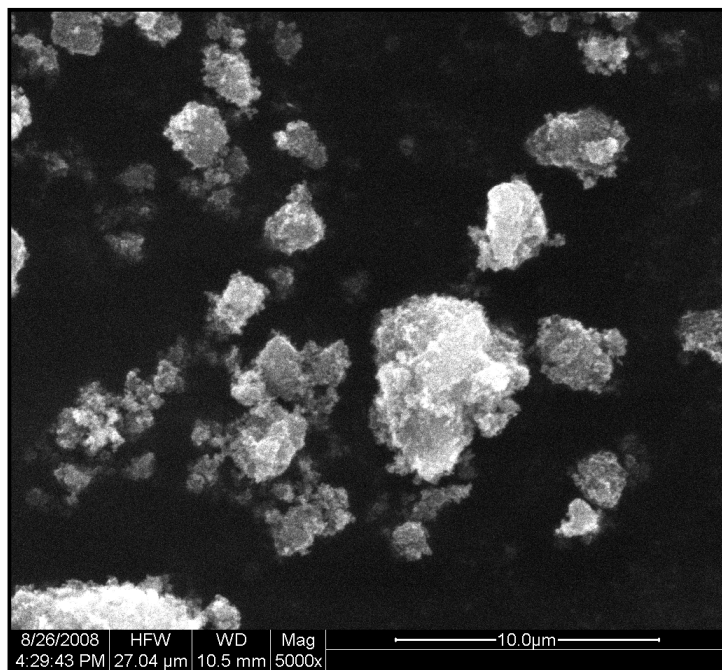


(a)

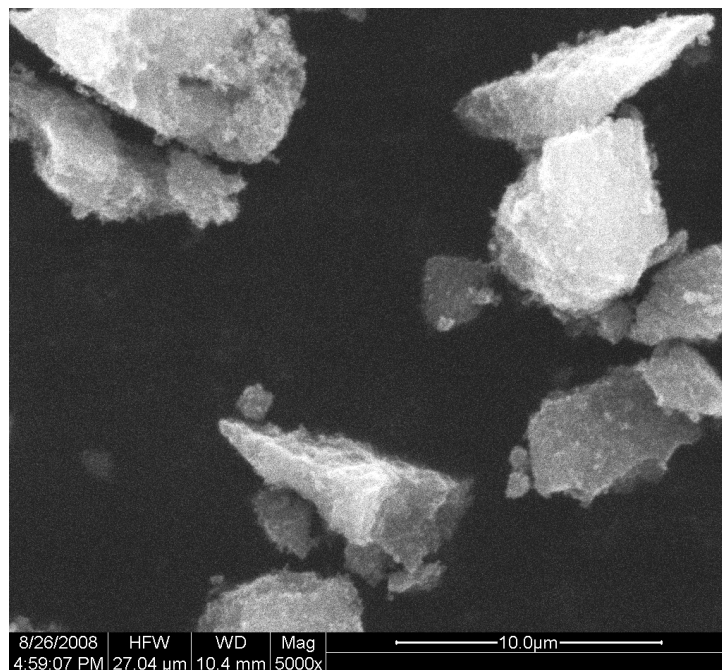


(b)

Fig. 6.4. SEM images of Au/TiO₂ catalysts prepared by sol method (a) Au/BRT4-fresh and (b) Au/BRT4-after reaction



(a)



(b)

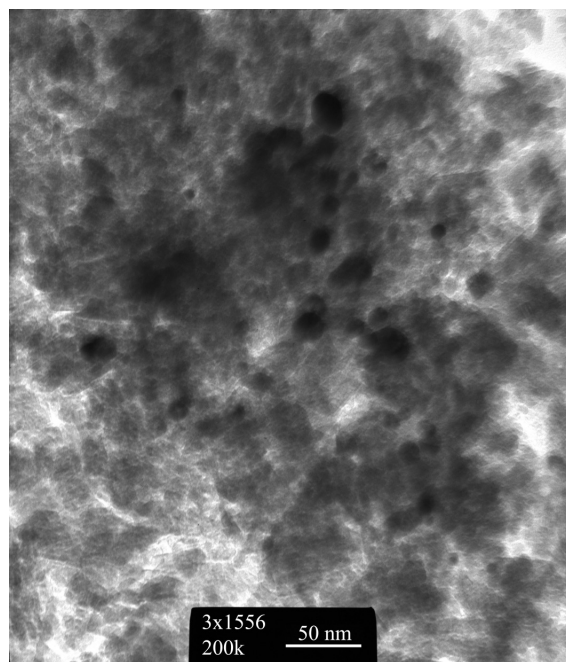
Fig. 6.5. SEM images of Au/TiO₂ catalysts prepared by sol method (a) Au/P25-fresh and (b) Au/P25- after reaction

6.2.4 Transmission Electron Microscopy analysis:

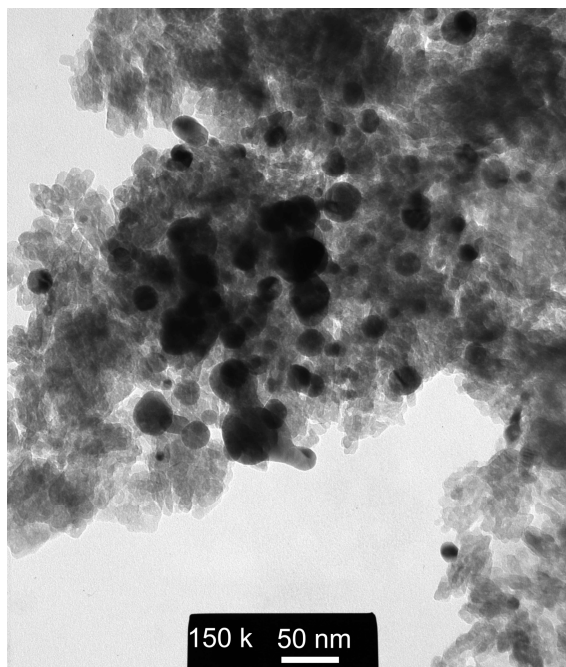
TEM images of the Au/BRT4 and Au/P25 samples prepared by sol method are given in Fig. 6.6 and Fig. 6.7 respectively. The particle size distribution of the Au/BRT4 and Au/P25 samples prepared by sol method are shown in Fig. 6.8 and Fig 6.9 respectively. The fresh Au/TiO₂ samples of both BRT4 and P25 show particle sizes in the range of 6 to 24 nm. The maximum numbers of particles are in the range of 13 to 18 nm. The average particle sizes of the fresh and used samples are given in Table 6.3. The average sizes of the gold particles in the fresh state were 15.2 and 15.1 nm in the case of Au/BRT4 and Au/P25 respectively. In the case of Au/BRT4-sol samples, sintering of the particles was observed in the case of samples used for the oxidation of CO. The size of the Au on BRT4 increases from 15.2 nm to 17.0 nm after the reaction. In the case of Au/P25 samples no such increase in particle size was observed after the reaction. The particle sizes in this case were 15.1 nm and 15.0 nm for the fresh and used samples respectively. This shows that gold particles on TiO₂ prepared by sol method are comparatively more stable against sintering on P25 TiO₂ compared to pure brookite.

Table 6.3. Average Au particle size from various sol derived Au/TiO₂ samples

Catalyst	Average size (nm)	(No. of particles studied)
Au/BRT4-fresh	15.2	56
Au/BRT4-used	17.0	167
Au/P25-fresh	15.1	59
Au/P25-used	15.0	149

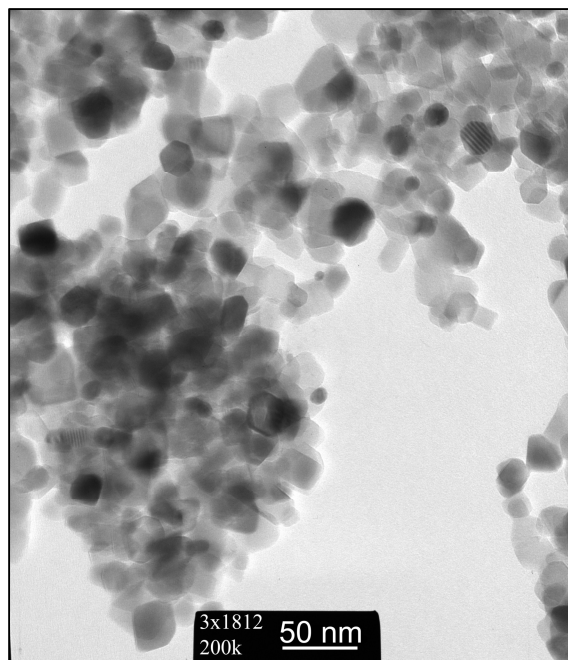


(a)

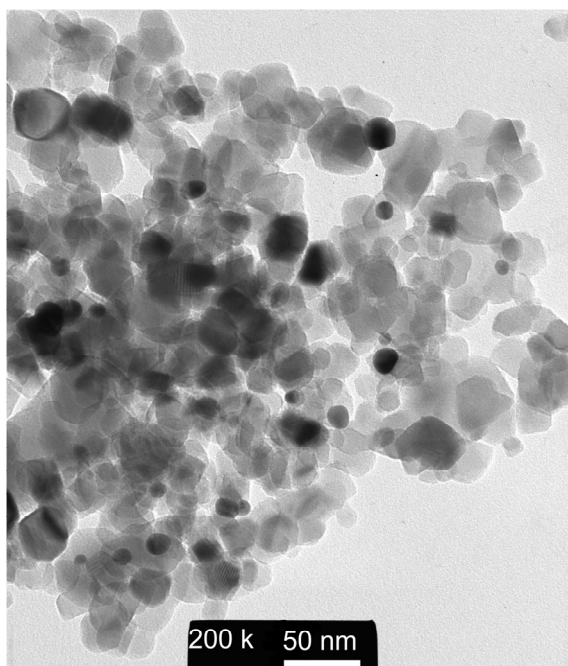


(b)

Fig. 6.6. TEM images of Au/BRT4 samples prepared by sol method (A) fresh and (B) after reaction

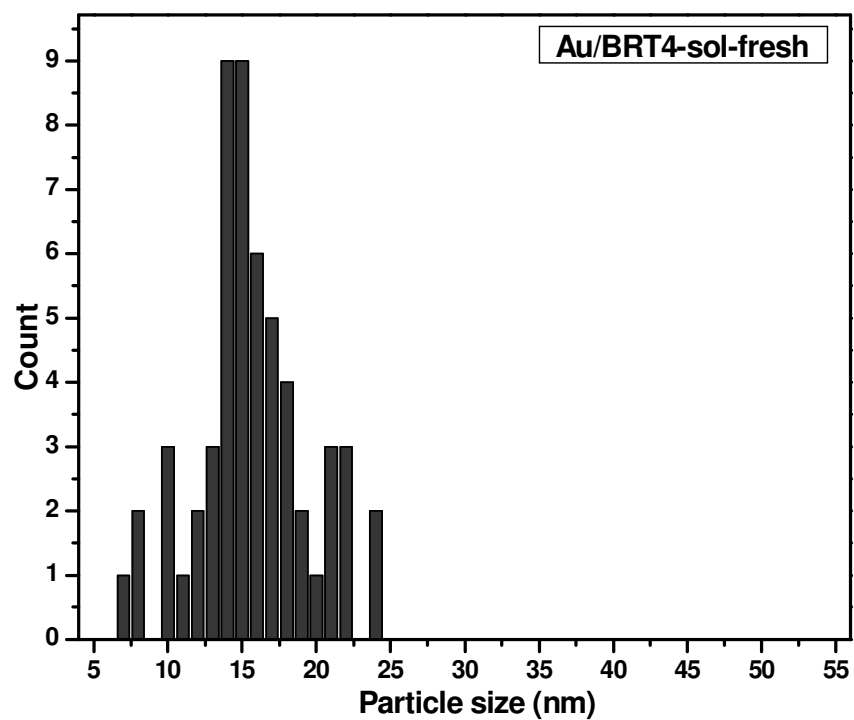


(a)

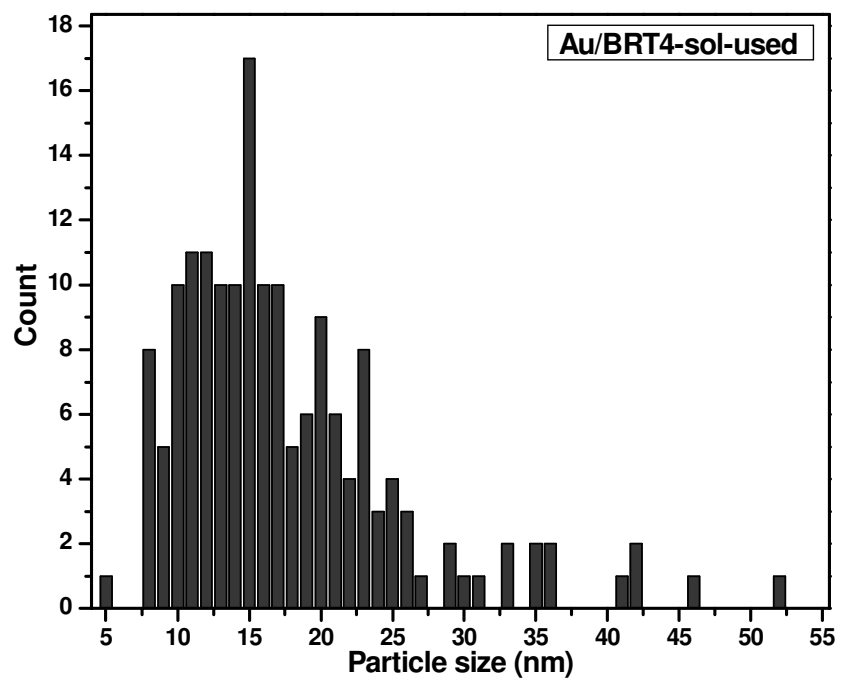


(b)

Fig. 6.7. TEM images of Au/P25 samples prepared by sol method (a) fresh and (b) after reaction

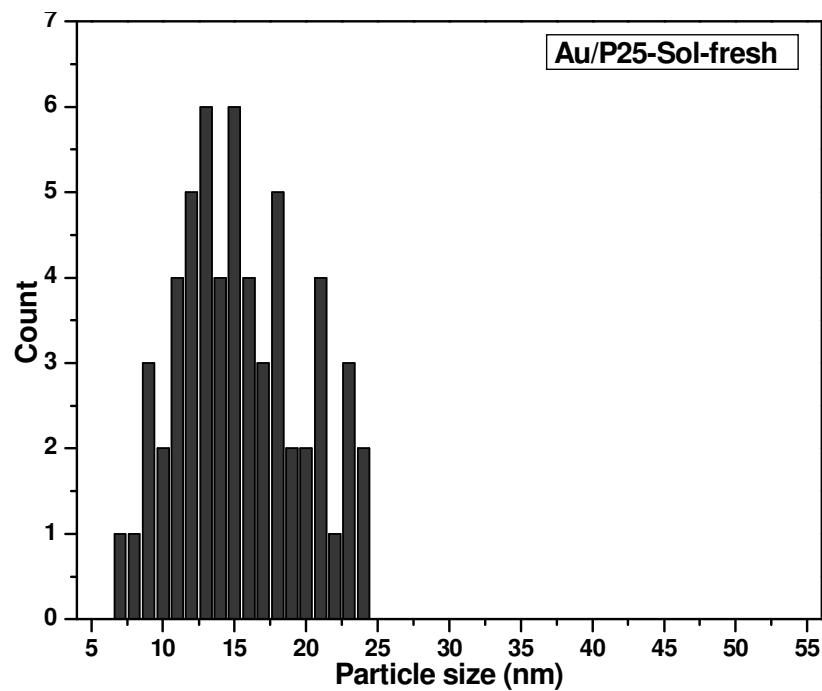


(a)

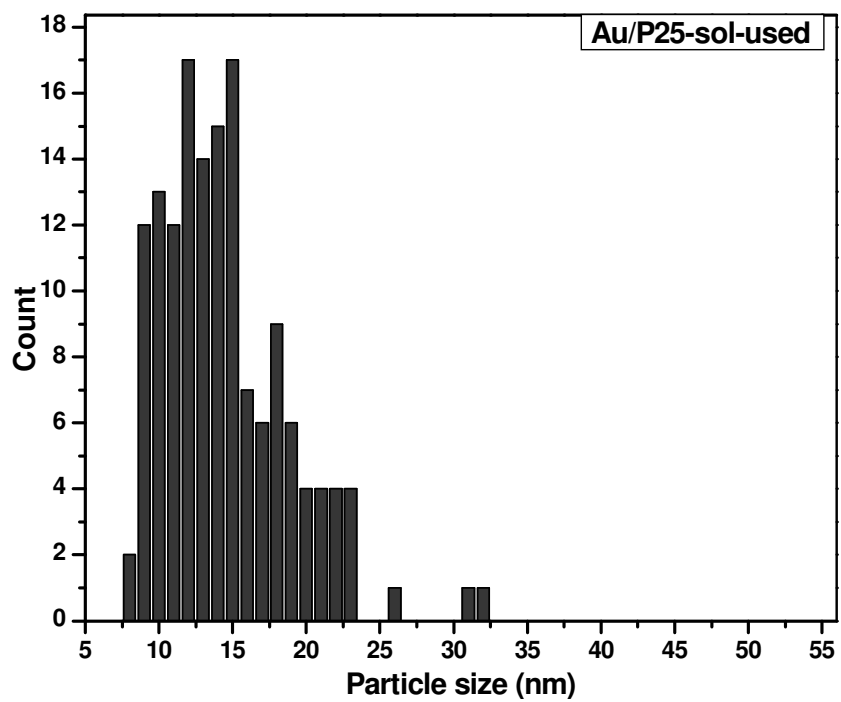


(b)

Fig. 6.8. Au particle size distribution in Au/BRT4 catalysts prepared by sol method (a) fresh (b) after reaction



(a)



(b)

Fig. 6.9. Au particle size distribution in the various Au/P25 catalysts prepared by sol method (a) fresh and (b) after reaction

6.2.5 Diffuse reflectance UV-Visible spectra of samples prepared by sol deposition

Diffuse reflectance UV-Visible spectra of the sol derived Au/TiO₂ samples are given in Fig. 6.10. All the samples show absorption at 550 nm which corresponds to the surface plasmon band of gold nanoparticles.

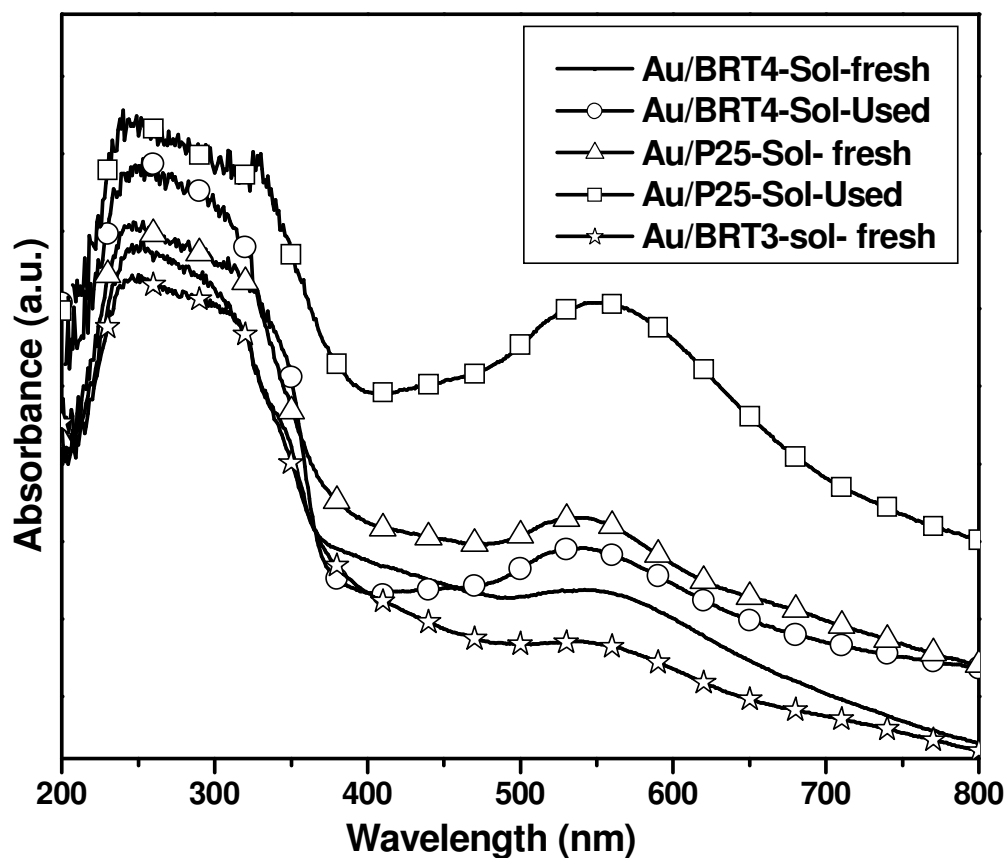


Fig. 6.10. Diffuse reflectance UV-Visible spectra of sol derived Au/TiO₂ samples

6.2.6 Activity of samples prepared by sol deposition for the oxidation of CO

A set of % CO conversion curves for sol derived Au/TiO₂ samples are given in Fig. 6.11. The temperature at which 50 % conversion is achieved, has been considered as

an accurate measure of the catalytic activity for CO oxidation. The temperature of 50 % conversion, T_{50} for CO oxidation is achieved at 298 K, 353 K and 378 K for the fresh Au/P25, Au/BRT3 and Au/BRT4 respectively. The CO oxidation results for the samples calcined at 673 K in O_2 showed that the T_{50} is attained at 298 K, 363 K and 403 K for Au/P25, Au/BRT3 and Au/BRT4 respectively. From this, it is clear that the activity of Au/P25 TiO_2 remains the same after calcination in oxygen whereas; there is a considerable decrease (25 K) in activity in the case of Au/BRT4 and a moderate decrease (10 K) in the case of Au/BRT3 after calcination in oxygen.

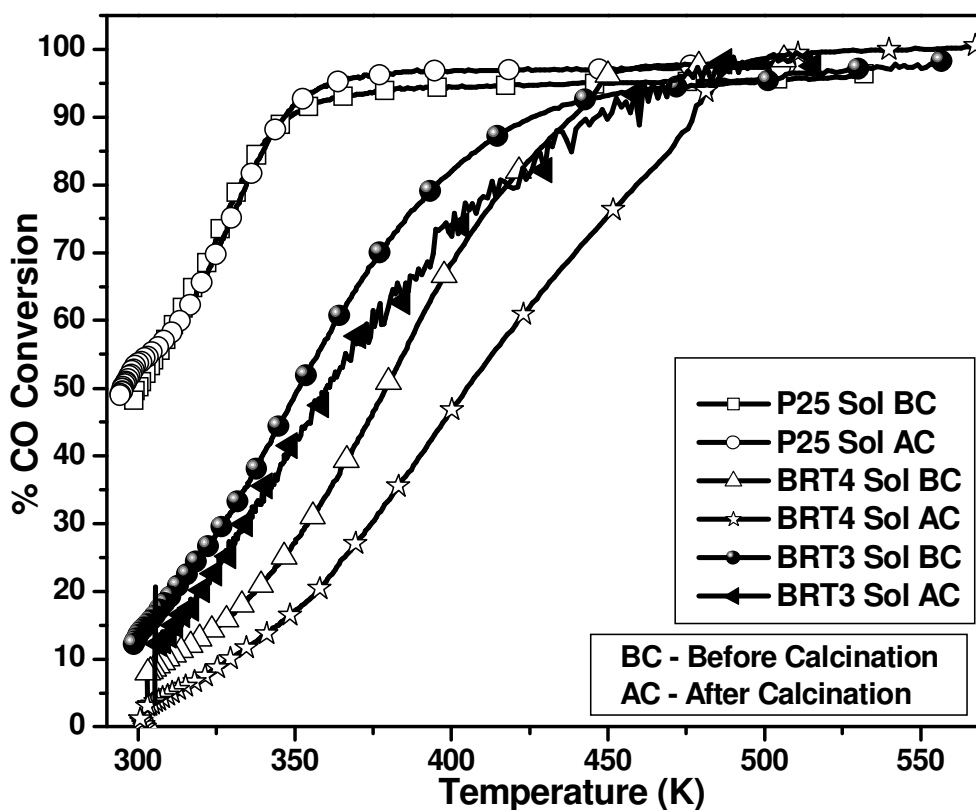


Fig. 6.11. CO oxidation activity of various Au/ TiO_2 samples prepared by sol method before and after calcination in O_2

6.2.7 Activity of samples prepared by deposition precipitation for the oxidation of CO

The % CO conversion curves for the Au/TiO₂ samples prepared by DP method are given in Fig 6.12. The temperature of 50 % conversion T₅₀ is achieved at 343 K and 440 K for the Au/BRT4 and Au/P25 samples before calcination respectively. Further, the catalytic activity was measured after calcining the samples in O₂ atmosphere at 673 K. The results showed a T₅₀ of 392 K and 440 K for Au/BRT4 and Au/P25 respectively. From the results it is clear that the activity of Au/BRT4 has decreased considerably after calcination at 673 K where as the activity of P25 remained unchanged after calcination.

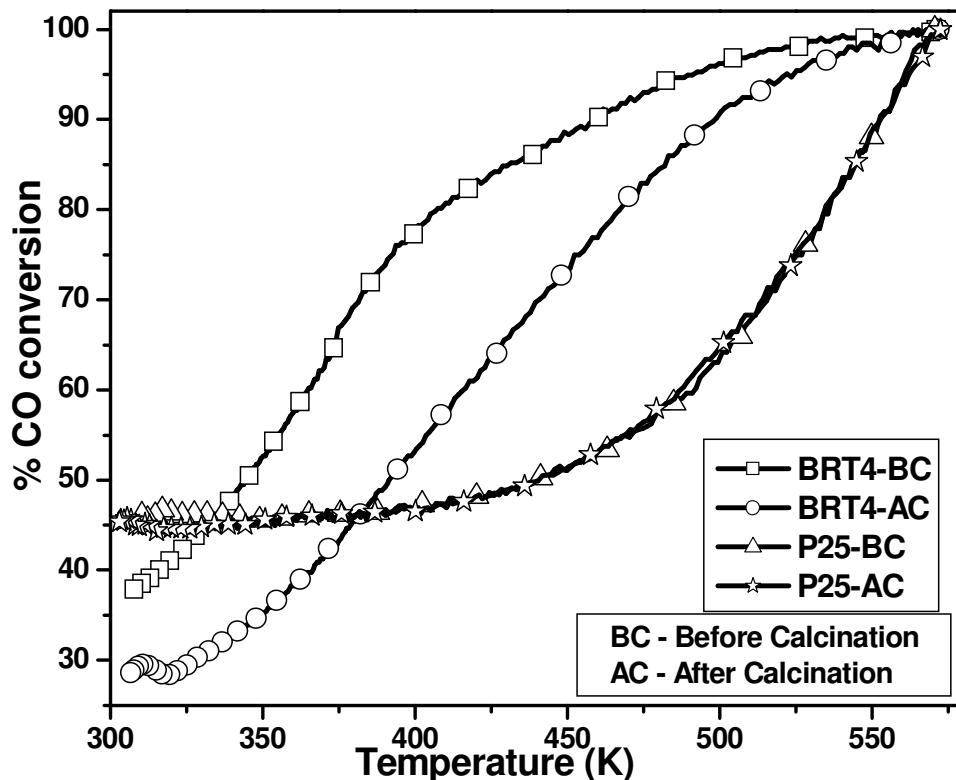


Fig. 6.12. CO oxidation activity of various Au/TiO₂ samples prepared by DP method before and after reduction in H₂

6.3 DISCUSSION

From the CO oxidation activity results on the catalysts prepared by deposition-precipitation and sol deposition methods described, the following three important observations are made. (i) Au/Brookite is more active than Au/P25 in catalysts prepared by deposition-precipitation method (ii) Reverse trend is observed (Au/P25 was more active than the Au/Brookite) when the catalysts were prepared by the sol deposition method and (iii) In both the methods, Au/Brookite shows a considerable decrease in activity after calcination whereas, Au/P25 shows absolute stability when treated at higher temperatures. Establishing the reasons behind the observations mentioned will be interesting and help in understanding and improving the CO oxidation activity of the various catalysts.

6.3.1 Explanation for the decrease in activity of brookite after calcination

It is clear from the results that the thermal stability of Au/brookite is very low compared to P25 TiO₂ and BRT3. Literature report showed an increase in activity after calcining the samples in air, which was attributed to the presence of the organic protecting agents, which were getting removed on calcination in air (Comotti *et al.*, 2006). However, in the present study, a decrease in activity after calcination, that too only in the case of brookite, was observed (The preparation method adopted here also involved the organic protecting agents in both P25 and BRT4 samples). Furthermore, the decrease in activity in the case of BRT4 was observed in the case of samples prepared by deposition-precipitation method as well, where protecting agents were

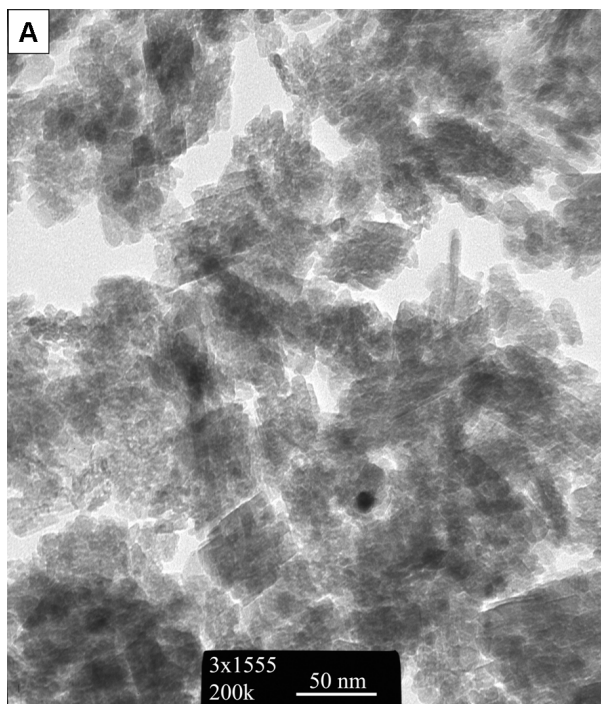
not used. This shows that the decrease in activity is due to the property of the support and not due to the preparation method adopted.

One of the ways by which the decrease in catalytic activity of Au/BRT4 can be explained is the change in the oxidation state of the gold. But none of the reports in the literature show any change in the oxidation state of gold after calcining the catalyst in air at higher temperature (Comotti *et al.*, 2006). This shows that the observed decrease in activity cannot be attributed to the change in the oxidation state of the gold. Decrease in activity was also observed when there is an increase in the particle size of the gold particles. The XRD results of the Au/BRT4 samples (Fig.6.2) before and after reaction show an increase in intensity of the peaks corresponding to gold. This can be attributed to the agglomeration of the gold particles after the catalytic measurements, whereas in Au/P25 samples (Fig. 6.3) such an observation is not made. The absence of peaks for gold in Au/P25 is attributed to the uniform distribution of the gold over P25. The non-appearance of gold peaks after the catalytic measurements led us to assume that there is no considerable agglomeration of gold particles taking place in Au/P25 during the calcination or the catalytic measurements.

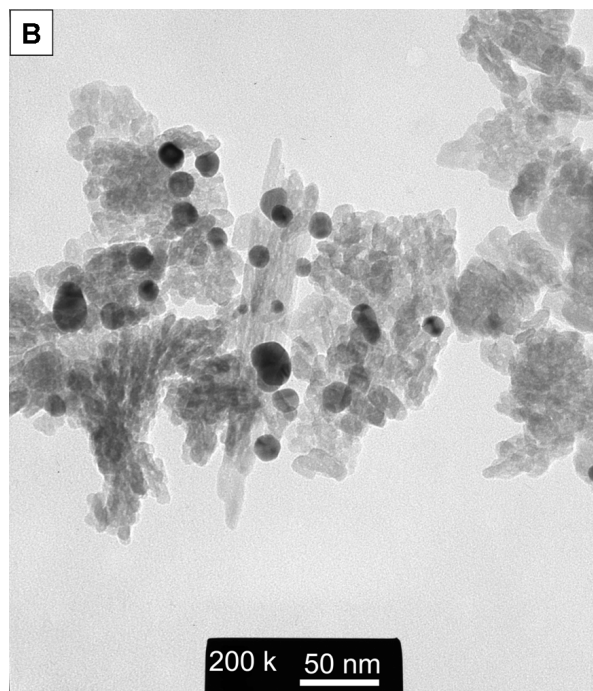
Another important observation is the lack of any change in the intensity of the peaks corresponding to brookite TiO_2 in Au/BRT4 while the intensity of Au peaks has increased. This shows that the crystallite size of brookite remained the same after the catalytic measurements. Since there is no change in the crystalline phase of the TiO_2 , the decrease in activity of Au/BRT4 can be attributed to the increase in gold particle size.

The TEM images (Fig. 6.6) also show a considerable increase in the particle size of gold in the case of Au/BRT4. The average particle size of gold (Table. 6.3) in Au/BRT4 increased from 15.2 to 17.0 nm after catalytic measurement whereas the particle size of Au in Au/P25 remain unchanged at 15.0 nm. The particle size distributions charts (Fig. 6.8 and 6.9) show the overall trend in particle sizes. It can also be observed from TEM (Fig. 6.6 and Fig. 6.13) that the brookite particles are well defined after calcination whereas before calcination they are present as agglomerates of finer particles.

The question which still remains unanswered is why gold is agglomerating while supported on brookite TiO_2 ? One possible reason for this observation will be the agglomeration of brookite particles, which in turn leads to agglomeration of the gold nanoparticles supported on them. It was reported that the surface energy plays a major role in determining the ability of the nanoparticles to avoid sintering at higher temperatures (Finnegan *et al.*, 2007; Majzlan *et al.*, 2000; McHale *et al.*, 1997). $\alpha\text{-Al}_2\text{O}_3$ is a thermodynamically stable phase at room temperature and pressure conditions. However, attempts to synthesize it in nanoscale always resulted in the formation of $\gamma\text{-Al}_2\text{O}_3$. Further, $\gamma\text{-Al}_2\text{O}_3$ can maintain a surface area of $150 \text{ m}^2 \text{ g}^{-1}$ at 1073 K whereas $\alpha\text{-Al}_2\text{O}_3$ sinters to $50 \text{ m}^2 \text{ g}^{-1}$ at the same temperature. The observed results were explained on the basis of the surface energies of $\alpha\text{-Al}_2\text{O}_3$ and $\gamma\text{-Al}_2\text{O}_3$.



(a)



(b)

Fig. 6.13. TEM images of Au/BRT4 prepared by sol deposition method (a) before and (b) after catalytic measurements

The surface energies were calculated by measuring the heats of adsorption of H₂O on the surface of alumina. At surface area lower than 125 m²g⁻¹, α-Al₂O₃ has a lower surface energy than γ-Al₂O₃. When the surface area exceeds 125 m²g⁻¹, the surface energies of α-Al₂O₃ and γ-Al₂O₃ were found to be 2.67 Jm⁻² and 1.67 Jm⁻² respectively. These values are in agreement with the theoretically simulated surface energies for the various planes of α-Al₂O₃ and γ-Al₂O₃ which were found to be in the range of 2.0 to 8.4 Jm⁻² and 0.8 to 2.5 Jm⁻² respectively (Blonski and Garofalini, 1995). Measurements of surface areas after heating at various temperatures showed that at temperatures greater than 773 K surface area of α-Al₂O₃ drops sharply whereas, the surface area of α-Al₂O₃ remains the same up to 1173 K. Thus, it was explained that the surface energy differences thermodynamically stabilize γ-Al₂O₃ over α-Al₂O₃ at higher temperatures, leading to sintering of α-Al₂O₃. Further, this explains the preferential formation of γ-Al₂O₃ over α-Al₂O₃ in the nanoscale.

On the basis of these results by McHale *et al.*, (1997), similar explanation for the agglomeration of brookite particles by comparison of the surface energies of anatase, brookite and rutile can be offered. Anatase, brookite and rutile phases of TiO₂ have surface energy values of (0.4 ± 0.2 Jm⁻²), (1.0 ± 0.2 Jm⁻²) and (2.2 ± 0.2 Jm⁻²) respectively (Ranade *et al.*, 2002). In the present study, the maximum decrease in the catalytic activity was observed in the case of Au/BRT4 (25 K) followed by Au/BRT3 (10 K) and Au/P25 showing no change. BRT4 which is 100 % brookite has a higher surface area (114 m²g⁻¹) than P25 (49 m²g⁻¹) which is (75 % anatase + 25 % rutile). When calcined at 673 K, the brookite (surface energy ~ 1.0 Jm⁻²) particles sinter more than the P25 (anatase + rutile) because of their higher surface energy. Even though P25 contains rutile, which has a higher surface energy (~ 2.2 Jm⁻²) than brookite, it

doesn't show any sintering as it is already having a very low surface area ($49 \text{ m}^2\text{g}^{-1}$). Reports show that 100 % rutile sinters rapidly when used at room temperatures (Ho and Yeung, 2007). This shows that the surface energy plays an important role in the thermal stability of the catalysts. Another report where sol deposition method was adopted show similar thermal stabilities for anatase and rutile. P25 showed better thermal stability than anatase and rutile (Comotti *et al.*, 2007). In this case, the specific surface area values of anatase, rutile and P25 were 327, 108 and $47 \text{ m}^2\text{g}^{-1}$ respectively. Hence, the similar thermal stabilities of anatase and rutile can be attributed to the higher surface area of anatase, which is thrice that of rutile. The TEM investigations also revealed considerable agglomeration of gold and TiO_2 in the case of rutile, whereas Au/Anatase showed considerable sintering of the support only. P25 showed no sintering of the support and the sintering of gold particles is similar to that of anatase. Thus, it can be concluded that brookite sinters far more than P25 both due to its higher surface area and surface energy. The thermal stability of Au/BRT3 (55 % anatase + 45 % brookite) further supports the above explanation. The decrease in catalytic activity in the case of Au/BRT3 (55 % anatase and 45 % brookite) can be attributed to the presence of brookite and higher surface area ($197 \text{ m}^2\text{g}^{-1}$).

The sintering of the support in turn leads to the agglomeration of the gold particles. In addition, some of the brookite in an effort to reduce its surface area can migrate over the gold particles. It is being reported that the corner/edge sites of the gold (Chiorino *et al.*, 2009; Lopez and Norskov, 2002; Mavrikakis *et al.*, 2000; Meyer *et al.*, 2004; Mills *et al.*, 2002) and gold-support interface are the active centres in the oxidation of CO (Bond and Thompson, 2001; Guzzi *et al.*, 2009; Haruta, 1997; Haruta *et al.*, 1992; Liu *et al.*, 2003; Pietron *et al.*, 2002; Schubert *et al.*, 2001). Both

the migration of the support over gold and the sintering of either the gold or the support can lead to a decrease in the gold-support interface, thereby decreasing the CO oxidation activity. This explains the observed trends in the CO oxidation activities of the various catalysts after calcination at 673 K.

6.3.2 Explanation for the higher activity of brookite in DP method:

The results of the catalytic measurements carried out show that in the present study, Au/P25 is more active in the sol deposition method, whereas, Au/BRT4 in the deposition-precipitation method. There are many reports which show that one method of deposition of gold gives a better catalytic activity than the other (Arena *et al.*, 2006; Dimitratos *et al.*, 2006; Grisel *et al.*, 2000). Previous studies of CO oxidation activity of different phases of TiO₂ were carried out using P25, anatase and rutile. In one case where the gold was loaded by deposition-precipitation method, the results showed that anatase had higher catalytic activity among rutile, anatase and P25 TiO₂ (75 % anatase + 25 % rutile) in spite of them having similar surface area values (Ho and Yeung, 2007). Further, the thermal stability of anatase was better than the other two supports. When the catalysts were prepared by sol deposition method, the anatase and rutile showed similar activity, while P25 showed slightly higher activity (Comotti *et al.*, 2007). In this case, the thermal stabilities of anatase and rutile were almost the same, where as P25 showed better thermal stability.

One reason which has been widely believed to be responsible for the variation in activity among supports is the point of zero charge (PZC). Comotti *et al.*, (2006) have reported the catalytic activity of gold sols deposited on different supports. The catalytic activity followed the order TiO₂ > Al₂O₃ > ZnO > ZrO₂. The PZC of TiO₂,

ZrO₂, γ -Al₂O₃ and ZnO are 6-7, 6-7, 9 and 11 respectively. This shows that the PZC of the support does not play a significant role in deciding the catalytic activity of the catalyst. The fresh gold sols when observed through TEM contained particles of spherical shape. When the gold particles are deposited on the various supports like TiO₂, ZrO₂, Al₂O₃ and ZnO, the shape of the particles change. This is significant since the change in shape means different number of Au atoms present at the corners and edges for different supports. The Au atoms present at the corners and edges were reported to be active sites (Bondzie *et al.*, 1999; Lopez *et al.*, 2004; Mavrikakis *et al.*, 2000; Valden *et al.*, 1998). Further, the ability of the support to get reduced and the ability to store oxygen do not play any role in being a good support for gold. It was found that Al₂O₃ which is difficult to reduce and has a low ability to store oxygen than ZnO is more active than ZnO (Comotti *et al.*, 2006).

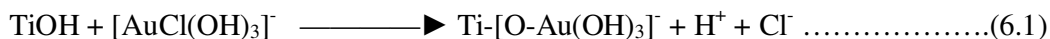
Based on the literature reports discussed above and the results obtained in the present study, it seems that the catalytic activity of the supported gold catalysts depends on various factors. Some of them are (i) nature of the support (ii) method by which gold is deposited (gold species involved) (ii) nature of bonding or interaction between the support and gold. A generalized explanation for the trends observed in the various literature reports is not possible because of the various factors involved. Further, for all the scientific explanations given so far, there exists an unexplained interaction between the support and the metal. The metal support interaction has not been explained so far in a generalized way, based on a few properties of the support and metal.

Another important property of the support that has not been considered in detail so far in the literature is their band energy positions and bandgaps. In the case of TiO₂, as

reported earlier, the three allotropic forms have different bandgaps and band energy positions. The band gaps of anatase, brookite and rutile are 3.05, 3.26 and 2.98 eV respectively. The conduction band energy positions of anatase, brookite and rutile are -0.45, -0.46 and -0.37 V vs. NHE respectively. Valence band energy positions of anatase, brookite and rutile are +2.6, +2.8 and 2.61 V vs. NHE respectively (Paola *et al.*, 2009). The interaction or charge transfer between the support and the metal depends on their respective energy positions. As such there are two possibilities for electron transfer in this case. First, if the Fermi level of gold is lower in energy than the valence band of TiO₂, the electron can be transferred from TiO₂ to gold. Second, if the Fermi level of gold is higher in energy than the conduction band of TiO₂, then the electron transfer from gold to TiO₂ is feasible. The Fermi energy of bulk gold is located at 1.00 V vs. NHE whereas for an Au₁₂ cluster, the Fermi energy is located at 1.54 V vs. NHE (Sankaran and Viswanathan, 2006). However, in this case, neither of the above mentioned two situations exists. Hence, it seems electron transfer is not possible both ways, either from TiO₂ to gold or from gold to TiO₂.

As it has been discussed earlier, the literature reports show that the anatase is in general the best support among the various allotropic forms of TiO₂. This is applicable to most of the methods of deposition of gold over TiO₂. This is due to the unexplained favourable interaction between the gold and anatase compared to rutile. Based on this, when the catalysts are prepared by the sol deposition method as in the present study, the catalytic activity is found to be proportional to the amount of anatase present in the support. This is due to the fact that the gold particles were prepared in solution and then they were bound to the various supports with the help of the organic molecules. In this case, only the general interaction between the support and gold dominates, thereby anatase gives the best result.

However, during the deposition-precipitation method, the deposition is different where negative ions are getting deposited on the surface of the support and there is regular bonding between the support and the gold species. The mechanism of deposition precipitation is as follows (Zanella *et al.*, 2005)



An explanation based on the PZC of the material is also not possible in this case. The PZCs of P25, anatase, brookite and rutile are 6.0, 5.88, 5.72 and 5.36 respectively. At pH above the PZC the surface of the supports will be negatively charged. At the pH 8 where the deposition-precipitation was carried out, the surfaces of P25, anatase and brookite will be negatively charged. The negative charge on the surface will follow the order rutile > brookite > anatase > P25. Thus there will be more repulsion between the surface and the gold species in brookite than P25. Based on this, brookite should give a catalyst with lower activity. However, the trend observed is the reverse of that. Hence, an explanation based on the PZC of the support is not possible in this case (Kosmulski, 2002; Moreau and Bond, 2007; Roessler *et al.*, 2002). Another possible explanation is based on the Ti-O bond distances of the various supports. As the $[\text{AuCl}(\text{OH})_3]^-$ binds to TiO_2 as $\text{Ti}-[\text{O}-\text{Au}(\text{OH})_3]^-$ the interaction between the TiO_2 support and the gold depends on the strength of the Ti-O bond. The Ti-O bond lengths of the various phases of TiO_2 crystal are given in Table 6.4 (Park *et al.*, 2009).

Table 6.4: Ti-O bond distances of the various allotropic forms of TiO₂

TiO ₂ phase	Ti-O bond distance (Å)
Anatase	1.92 – 1.95
Brookite	1.87 – 2.04
Rutile	1.91 – 1.94

Based on the Ti-O bond length among the various allotropic forms of TiO₂, the strongest interaction with the gold ([AuCl(OH)₃]⁻) species in DP method is expected in the case of brookite. This suggests the possible reasons behind the observed higher activity of brookite compared to anatase or rutile in samples prepared by the DP method. Further more, Li *et al.*, (2008) have calculated the bond distances of brookite (210) and anatase (101) surfaces using density functional theory calculations. In addition, they have calculated the adsorption energies due to the interaction of Ti-O bond with H₂O and HCOOH. The results show that the brookite has shorter Ti-O bond distances and these differences significantly change the reactivity toward adsorption of various molecules, and most importantly, generate highly active sites at the junction between different structural units on brookite TiO₂ (210). The brookite (210) and anatase (101) have similar structural building blocks and the various Ti-O bond distances for anatase (101) are 1.835, 1.854 and 2.021 Å. In the same order the Ti-O bond distances in brookite (210) are 1.817, 1.842 and 1.949/1.973 Å. The adsorption energies for H₂O and HCOOH are 1.02 and 1.12 eV for brookite (210) whereas those for anatase (101) are 0.71 and 0.91 eV respectively. These results suggest that brookite TiO₂, with its smaller Ti-O bond distances can interact more effectively compared to anatase in cases where the Ti-O bond is involved. Such a

strong interaction of brookite with the gold particle will lead to the formation of the following active sites (i) gold-support perimeter interface and/or (ii) faceting of the gold particles leading to step and edge sites, which in turn can lead to higher catalytic activity.

6.4 CONCLUSIONS

Au supported on brookite and P25 TiO₂ were prepared by deposition-precipitation and sol deposition methods. Au/P25 was found to be more active when prepared by sol deposition method whereas Au/brookite showed better activity in case of samples prepared by deposition-precipitation method. Au/brookite prepared by both the methods showed a decrease in the activity after calcination at higher temperature. Decrease in the activity of Au/Brookite upon calcination is due to its higher surface enthalpy which leads to agglomeration of brookite and its migration over Au. Higher activity of brookite in DP method is due to better interaction between depositing species ([AuCl(OH)₃]⁻) and brookite because of smaller Ti-O bond distance.

CHAPTER 7

SUMMARY AND CONCLUSIONS

In this study, CeO₂ modified TiO₂ catalysts were prepared by co-precipitation method in the presence of polymer. CeO₂ loading on TiO₂ was varied from 0.25 % to 9.0 %. XRD patterns showed the presence of cubic phase of CeO₂ and anatase phase of TiO₂. Rutile phase of TiO₂ was observed at smaller loadings of CeO₂ on TiO₂. TEM images showed particle sizes distributed from 10-50 nm, with an average particle size of 25 nm. UV-visible spectra of CeO₂ modified TiO₂ showed red shifts up to 50 nm compared to TiO₂. Studies on the photocatalytic degradation of methylene blue under UV light irradiation showed that CeO₂ modified TiO₂ were more active than TiO₂ and CeO₂. Studies under visible light ($\lambda > 420$ nm) irradiation showed that CeO₂ modified TiO₂ samples were more active than CeO₂, whereas TiO₂ was inactive. The optimum loading of CeO₂ was found to be 1.0 % for photocatalytic studies under both UV and visible irradiation. Studies carried out in dark on the adsorption of methylene blue on the catalysts showed that TiO₂ had three times more adsorption capacity than CeO₂. The band positions of CeO₂ and TiO₂ in energy scale were calculated and it was found that CeO₂ has its conduction band at a potential suitable for transferring electrons to the CB of TiO₂. In spite of the suitable band gap and band position, CeO₂ is less active in visible light due to the high recombination and poor adsorption of methylene blue. Mechanism of CeO₂ modified TiO₂ in visible light, involves the absorption of visible light by CeO₂ and transfer to the CB of TiO₂ which in turn will be utilized for the degradation reactions. Higher activity of CeO₂

modified TiO₂ in UV light was due to the decrease in recombination of charge carriers because of the easy redox nature of Ce⁴⁺/Ce³⁺ couple.

Carbon-TiO₂ composites were prepared by two different methods namely (i) preparing carbon and TiO₂ together from sucrose and TiCl₃ and (ii) preparing carbon over P25 TiO₂ using sucrose. Varying amounts of carbon were loaded on TiO₂ by altering the temperature of calcination of the samples. Raman spectra confirmed the graphitic nature of the carbon and CHN elemental analysis was used to measure the amount of carbon loading. From the TEM images, it can be seen that the carbon and TiO₂ have a better interaction in method (i) than in method (ii). Diffuse reflectance UV-visible spectra showed no red shift in absorption onset for carbon-TiO₂ samples. This implies that doping of carbon into the lattice of TiO₂ is not taking place and any improvement in activity is due to the coexistence of carbon and TiO₂.

Studies on the photocatalytic degradation of methylene blue under UV-visible irradiation showed improvement in activity in carbon-TiO₂ samples, irrespective of the amount of carbon. The observed enhancement in activity could be attributed to larger availability of target molecules (methylene blue) near the surface of the photocatalyst because of the higher adsorption capacity of carbon. Moreover, carbon was playing a role of trapping the excited electrons as its Fermi level was lower in energy compared to the conduction band of TiO₂. In addition, the improvement in activity of carbon-TiO₂ composites compared to TiO₂ was higher in the case of samples prepared by the method (i) than by the method (ii). This could be attributed to the better interaction between carbon and TiO₂ when they were prepared simultaneously.

Rhombohedral CdSnO_3 and orthorhombic Cd_2SnO_4 were prepared by coprecipitation method. CdSnO_3 and Cd_2SnO_4 were found to have bandgaps of 3.0 and 2.3 eV, respectively from the Diffuse Reflectance UV-visible spectral studies. Studies of photocatalytic degradation of *p*-chlorophenol showed that CdSnO_3 was more active than Cd_2SnO_4 under UV-visible light irradiation whereas only Cd_2SnO_4 is active in visible light ($\lambda > 420$ nm) irradiation. The observed photocatalytic activities were in agreement with the UV-visible absorption onset of the catalysts. Percentage photocatalytic degradation based on the COD measurements was slightly lower than percentage degradation based on the UV-visible absorbance measurements.

Flat band potentials of the catalyst were determined from the Mott-Schottky plots based on the electrochemical impedance measurements. CdSnO_3 and Cd_2SnO_4 have flat band potentials of 0.43 and 0.51 V (vs. NHE) respectively. Studies on photocatalytic evolution of hydrogen showed no activity, which was in accordance with the determined flat band potentials.

Nanoparticles of gold were deposited on brookite (BRT4) and P25 TiO_2 by two methods namely (i) sol deposition and (ii) deposition precipitation. Studies on the oxidation of carbon monoxide showed that Au/P25 was more active when prepared by sol deposition method whereas Au/BRT4 has a higher activity in case of samples prepared by deposition precipitation method. After calcination at higher temperature, Au/BRT4 showed a decrease in activity whereas the activity of Au/P25 remained unchanged.

Decrease in activity of Au/BRT4 upon calcination was attributed to the higher surface enthalpy of brookite which leads to its agglomeration at higher temperatures. Higher

activity of Au/BRT4 in samples prepared by DP method, was attributed to the better interaction between the depositing species ($[\text{AuCl}(\text{OH})_3]^-$) and brookite, owing to its smaller Ti-O bond distance.

REFERENCES

1. **Andreozzi, R., V. Caprio, A. Insola and R. Marotta** (1999) Advanced oxidation processes (AOP) for water purification and recovery. *Catalysis Today*, **53**, 51-59.
2. **Ao, Y., J. Xu, D. Fu, X. Shen and C. Yuan** (2008) Low temperature preparation of anatase TiO₂-activated carbon composite film. *Appl. Surf. Sci.*, **254**, 4001-4006.
3. **Arena, F., P. Famulari, G. Trunfio, G. Bonura, F. Frusteri and L. Spadaro** (2006) Probing the factors affecting structure and activity of the Au/CeO₂ system in total and preferential oxidation of CO. *Appl. Catal. B-Environ.*, **66**, 81-91.
4. **Asahi, R., T. Morikawa, T. Ohwaki, K. Aoki and Y. Taga** (2001) Visible-light photocatalysis in nitrogen-doped titanium oxides. *Science*, **293**, 269-271.
5. **Bassekhouad, Y., N. Chaoui, M. Trzpit, N. Ghazzal, D. Robert and J.V. Weber** (2006) UV-Vis versus visible degradation of Acid Orange II in a coupled CdS/TiO₂ semiconductors suspension. *J. Photoch. Photobio., A*, **183**, 218-224.
6. **Berger, T., M. Sterrer, O. Diwald, E. Knozinger, D. Panayotov, T.L. Thompson and J.T. Yates** (2005) Light-induced charge separation in anatase TiO₂ particles. *J. Phys. Chem. B*, **109**, 6061-6068.
7. **Bethke G.K. and H.H. Kung** (2000) Selective CO oxidation in a hydrogen-rich stream over Au/ γ -Al₂O₃ catalysts. *Appl. Catal. A-Gen.*, **194**, 43-53.
8. **Blanco, J., S. Malato, P.F. Ibanez, D. Alarcon, W. Gernjak and M.I. Maldonado** (2009) Review of feasible solar energy applications to water processes. *Renew. Sust. Energ. Rev.*, **13**, 1437-1445.
9. **Block, M. and D. Hanrahan** (2009) *World's worst polluted places report 2009*, Blacksmith Institute, New York.
10. **Blonski, S. and S.H. Garofalini** (1995) Molecular dynamics simulations of α -alumina and γ -alumina surfaces. *Surf. Sci.*, **295**, 263-274.
11. **Bocuzzi, F., A. Chiorino, M. Manzoli, D. Andreeva and T. Tabakova** (1999) FTIR study of the low-temperature water-gas shift reaction on Au/Fe₂O₃ and Au/TiO₂ catalysts. *J. Catal.*, **188**, 176-185.
12. **Bond, G.C. and D.T. Thompson** (2001) Gold-catalysed oxidation of carbon monoxide. *Gold Bull.*, **33**, 41-51.

13. **Bond, G.C., P.A. Sermon, G. Webb, D.A. Buchanan and P.B. Wells** (1973) Hydrogenation over supported gold catalysts. *J. Chem. Soc., Chem. Commun.*, 444b-445.
14. **Bondzie, V. A., S.C. Parker and C.T. Campbell** (1999) Oxygen adsorption on well-defined gold particles on TiO₂(110). *J. Vac. Sci. Technol. A*, **17**, 1717-1720.
15. **Bott, A.W.** (1998) Electrochemistry of semiconductors. *Current Separations*, **17:3**, 87
16. **Brown M., A. Green, G. Cohn and H. Andersen** (1960) Purifying hydrogen by selective oxidation of carbon monoxide. *Ind. Eng. Chem.*, **52**, 841-844.
17. **Cameiro, J.O., V. Teixeira, A. Portinha, A. Magalhaes, R. Newton and P. Coutinho** (2007) Iron-doped photocatalytic TiO₂ sputtered coatings on plastics for self-cleaning applications. *Mat. Sci. Eng. B-Adv.*, **138**, 144-150.
18. **Carrettin, S., P. Concepcion, A. Corma, J.M.N. Lopez and V.F. Puentes** (2004) Nanocrystalline CeO₂ increases the activity of Au for CO oxidation by two orders of magnitude. *Angew. Chem. Int. Ed.*, **43**, 2538-2540.
19. **Chang, J.T., Y.F. Lai and J.L. He** (2005) Photocatalytic performance of chromium or nitrogen doped arc ion plated-TiO₂ films. *Surf. Coat. Technol.*, **200**, 1640-1644.
20. **Chen, D., D. Yang, Q. Wang and Z. Jiang** (2006) Effects of boron doping on photocatalytic activity and microstructure of titanium dioxide nanoparticles. *Ind. Eng. Chem. Res.*, **45**, 4110-4116.
21. **Chen, F., J. Zhao and H. Hidaka** (2003) Adsorption factor and photocatalytic degradation of dye-constituent aromatics on the surface of TiO₂ in the presence of phosphate anions. *Res. Chem. Intermediat.*, **29**, 733-748.
22. **Chiorino, A., M. Manzoli, F. Menegazzo, M. Signoretto, F. Vindigni, F. Pinna and F. Boccuzzi** (2009) New insight on the nature of catalytically active gold sites: Quantitative CO chemisorption data and analysis of FTIR spectra of adsorbed CO and of isotopic mixtures. *J. catal.*, **262**, 169-176.
23. **Cho, I., C.H. Kwak, D.W. Kim, S. Lee and K.S. Hong** (2009) Photophysical, photoelectrochemical, and photocatalytic properties of novel SnWO₄ oxide semiconductors with narrow band gaps. *J. Phys. Chem. C*, **113**, 10647-10653.
24. **Chuan, X.Y., M. Hirano and M. Ingaki** (2004) Preparation and photocatalytic performance of anatase-mounted natural porous silica, pumice, by hydrolysis under hydrothermal conditions. *Appl. Catal. B-Environ.*, **51**, 255-260.

25. **Clesceri, L.S., A.E. Greenberg and A.D. Eaton** (Ed.), (1998) *Standard Methods for the Examination of Water and Waste Water*, 20th Edition, Washington, Part 5000, pp. 14-15.
26. **Colls, J.** (2002) *Air pollution 2nd Ed*, Clay's Library of Health and Environment, London, pp. 40.
27. **Comotti, M., C. Weidenthaler, W. Li and F. Schuth** (2007) Comparison of gold supported catalysts obtained by using different allotropic forms of titanium dioxide *Topics catal.*, **44**, 275-284.
28. **Comotti, M., W. Li, B. Spliethoff and F. Schuth** (2006) Support effect in high activity gold catalysts for CO oxidation. *J. Am. Chem. Soc.*, **128**, 917-924.
29. **Cordero, T., J. Chovelon, C. Duchamp, C. Ferronato and J. Matos** (2007) Surface nano-aggregation and photocatalytic activity of TiO₂ on H-type activated carbons. *Appl. Catal. B-Environ.*, **73**, 227-235.
30. **Costello, C. K., M.C. Kung, H.S. Oh, Y. Wang and H.H. Kung** (2002) Nature of the active site for CO oxidation on highly active Au/ γ -Al₂O₃ *Appl. Catal., A-Gen.*, **232**, 159-168.
31. **Cullity, B.D.** (1971) *Elements of X-ray diffraction*. Addison-Wesley, Massachusetts.
32. **Date, M., Y. Ichihashi, T. Yamashita, A. Chiorino, F. Boccuzzi and M. Haruta** (2002) Performance of Au/TiO₂ catalyst under ambient conditions. *Catal. Today*, **72**, 89-94.
33. **DeCicco, J. and M. Thomas** (1999) *Green guide to cars & trucks: model year 1999* American Council for an Energy-Efficient Economy, Washington, D.C., pp.93.
34. **Devi, L. G., N. Kottam, S. G. Kumar and K. E. Rajashekhara** (2010) Preparation, characterization and enhanced photocatalytic activity of Ni²⁺ doped titania under solar light. *Cent. Eur. J. Chem.*, **8**, 142-148.
35. **Devi, L. G., S. G. Kumar, B. N. Murthy and N. Kottam** (2009) Influence of Mn²⁺ and Mo⁶⁺ dopants on the phase transformations of TiO₂ lattice and its photocatalytic activity under solar illumination. *Catal. Commun.*, **10**, 794-798.
36. **Dimitratos, N., A. Villa, C.L. Bianchi, L. Prati and M. Makkee** (2006) Gold on titania: Effect of preparation method in the liquid phase oxidation. *Appl. Catal. A-Gen.*, **311**, 185-192.
37. **Djellal, L., S. Omeiri, A. Bouguelia and M. Trari** (2009) Photoelectrochemical hydrogen-evolution over *p*-type chalcopyrite CuInSe₂. *J. Alloy Compd.*, **476**, 584-589.

38. **Domen, K., J. Yoshimura, T. Sekine, A. Tanaka and T. Onishi** (1990) A novel series of photocatalysts with an ion-exchangeable layered structure of niobate. *Catal. Lett.*, **4**, 339–343.
39. **Doong, R. A., C. H. Chen, R. A. Maithreepala and S. M. Chang** (2001) The influence of pH and cadmium sulfide on the photocatalytic degradation of 2-chlorophenol in titanium dioxide suspensions. *Water Res.*, **35**, 2873-2880.
40. **Douy, A. and P. Odier** (1989) The polyacrylamide gel: A novel route to ceramic and glassy oxide powders. *Mater. Res. Bull.*, **24**, 1119-1126.
41. **Dunnill, C. W., Z. A. Aiken, A. Kafizas, J. Pratten, M. Wilson, D. J. Morgan and I. P. Parkin** (2009) White light induced photocatalytic activity of sulfur-doped TiO₂ thin films and their potential for antibacterial application. *J. Mater. Chem.*, **19**, 8747-8754.
42. **Dvoranova, D., V. Brezova, M. Mazur and M. A. Malati** (2002) Investigations of metal-doped titanium dioxide photocatalysts. *Appl. Catal. B-Environ.*, **37**, 91-105.
43. **Ebina, Y. N. Sakai and T. Sasaki** (2005) Photocatalyst of lamellar aggregates of RuO_x-loaded perovskite nanosheets for overall water splitting. *J. Phys. Chem. B*, **109**, 17212–17216.
44. **Engel, T. and G. Ertl** (1978) A molecular beam investigation of the catalytic oxidation of CO on Pd (111). *J. Chem. Phys.*, **69**, 1267-1281.
45. **Engel, T. and G. Ertl** (1979) Elementary steps in the catalytic oxidation of carbon monoxide on platinum metals. *Adv. Catal.*, **28**, 1-78.
46. **Fard, F. G., C.A. Hogarth and D.H. Waters** (1983) The diffuse reflectance spectra of mono-cadmium and di-cadmium stannates. *J. Mater. Sci. Lett.*, **2**, 505-510.
47. **Farhataziz, A. and B. Ross** (1977) Selective specific rates of reactions of transients in water and aqueous solutions. Part III. Hydroxyl radical and perhydroxyl radical and their radical ions, *Natl. Stand. Ref. Data Ser.*, USA National Bureau of Standards, Notre Dame, **59**, 22-67.
48. **Fenton, H.J.H.** (1894) Oxidation of tartaric acid in the presence of iron. *J. Chem. Soc. Trans.*, **65**, 899-910.
49. **Fetterolf, M.L., H.V. Patel and J.M. Jennings** (2003) Adsorption of methylene blue and acid blue 40 on titania from aqueous solution. *J. Chem. Eng. Data*, **48**, 831-835.
50. **Finnegan, M. P., H. Zhang and J.F. Banfield** (2007) Phase stability and transformation in titania nanoparticles in aqueous solutions dominated by surface energy. *J. Phys. Chem. C*, **111**, 1962-1968.

51. **Fox, M. A., C.C. Chen and B. A. Lindig** (1982) Transients generated upon photolysis of colloidal titanium dioxide in acetonitrile containing organic redox couples. *J. Am. Chem. Soc.*, **104**, 5828-5829.
52. **Fox, M.A. and M. T. Dulay** (1993) Heterogeneous photocatalysis. *Chem. Rev.*, **93**, 341-357.
53. **Fu, L., N.Q. Wu, J.H. Yang, F. Qu, D.L. Johnson, M.C. Kung, H.H. Kung and V.P. Dravid** (2005) Direct Evidence of Oxidized Gold on Supported Gold Catalysts. *J. Phys. Chem. B*, **109**, 3704-3706.
54. **Fu, Q., H. Saltsburg and M.F. Stephanopoulos** (2003) Active nonmetallic Au and Pt species on ceria-based water-gas shift catalysts. *Science*, **301**, 935-938.
55. **Fujishima, A. and K. Honda** (1972) Electrochemical photolysis of water at a semiconductor electrode. *Nature*, **238**, 37-38.
56. **Fujishima, A., T.N. Rao and D.A Tryk** (2000) Titanium dioxide photocatalysis. *J. Photochem. Photobiol. C: Rev.*, **1**, 1-21.
57. **Fujishima, A., X. Zhang and D. A. Tryk** (2008) TiO₂ photocatalysis and related surface phenomena. *Surf. Sci. Rep.*, **63**, 515-582.
58. **Geng, Q., Q. Guo, C. Cao and L. Wang** (2008) Investigation into nanoTiO₂/ACSPCR for decomposition of aqueous hydroquinone. *Ind. Eng. Chem. Res.*, **47**, 2561-2568.
59. **Glaze, W.H. and J.W. Kang** (1989) Advanced oxidation processes. Description of a kinetic model for the oxidation of hazardous materials in aqueous media with ozone and hydrogen peroxide in a semibatch reactor. *Ind. Eng. Chem. Res.*, **28**, 1573-1580.
60. **Gouvea, C.A.K., F. Wypych, S. G. Moraes, N. Duran, N. Nagata and P. P. Zamora** (2000) Semiconductor-assisted photocatalytic degradation of reactive dyes in aqueous solution. *Chemosphere*, **40**, 433-440.
61. **Grisel, R.J.H., P.J. Kooyman and B.E. Nieuwenhuys** (2000) Influence of the preparation of Au/Al₂O₃ on CH₄ oxidation activity. *J. Catal.*, **191**, 430-437.
62. **Grisel, R.J.H. and B.E. Nieuwenhuys** (2001) Selective oxidation of CO, over supported Au catalysts. *J. Catal.*, **199**, 48-59.
63. **Grunwaldt, J. D. and A. Baiker** (1999) Gold/Titania interfaces and their role in carbon monoxide oxidation. *J. Phys. Chem. B*, **103**, 1002-1012.
64. **Grunwaldt, J. D., M. Maciejewski, O.S. Becker, P. Fabrizioli and A. Baiker** (1999) Comparative study of Au/TiO₂ and Au/ZrO₂ catalysts for low-temperature CO oxidation. *J. Catal.*, **186**, 458-469.

65. **Guczi, L., A. Beck and K. Frey** (2009) Role of promoting oxide morphology dictating the activity of Au/SiO₂ catalyst in CO oxidation. *Gold Bull.*, **42**, 5-12.
66. **Guzman, J. and B.C. Gates** (2004) Catalysis by supported gold: Correlation between catalytic activity for CO oxidation and oxidation states of gold. *J. Am. Chem. Soc.* **126**, 2672-2673.
67. **Haber, F. and J. Weiss** (1934) The catalytic decomposition of hydrogen peroxide by iron salts. *Proc. R. Soc. Lond. A*, **147**, 332-351.
68. **Haruta, M.** (1997) Size- and support-dependency in the catalysis of gold. *Catal. Today*, **36**, 153-166.
69. **Haruta, M.** (2002) Catalysis of gold nanoparticles deposited on metal oxides. *Cattech*, **6**, 102-115.
70. **Haruta, M. N. Yamada, T. Kobayashi and S. Iijima** (1989) Gold catalysts prepared by coprecipitation for low-temperature oxidation of hydrogen and of carbon monoxide. *J. Catal.*, **115**, 301-309.
71. **Haruta, M., S. Tsubota, T. Kobayashi, H. Kageyama, M.J. Genet and B. Delmon** (1993) Low-temperature oxidation of CO over gold supported on TiO₂, α -Fe₂O₃, and Co₃O₄. *J. Catal.*, **144**, 175-192.
72. **Haruta, M., T. Kobayashi, H. Sano and N. Yamada** (1987) Novel Gold catalysts for the oxidation of Carbon monoxide at a temperature far Below 0 °C. *Chem. Lett.*, **16**, 405-408.
73. **Hitoki, G., A. Ishikawa, T. Takata, J.N. Kondo, M. Hara and K. Domen** (2002) Ta₃N₅ as a novel visible light-driven photocatalyst ($\lambda < 600$ nm). *Chem. Lett.*, **31**, 736-737.
74. **Hitoki, G., T. Takata, J.N. Kondo, M. Hara, H. Kobayashi and K. Domen** (2002) An oxynitride, TaON, as an efficient water oxidation photocatalyst under visible light irradiation ($\lambda \leq 500$ nm). *Chem. Commun.*, 1698-1699.
75. **Ho, K.Y. and K.L. Yeung** (2007) Properties of TiO₂ support and the performance of Au/TiO₂ catalyst for CO oxidation reaction. *Gold Bull.*, **40**, 15-30.
76. **Ho, W., and J.C. Yu** (2006) Sonochemical synthesis and visible light photocatalytic behavior of CdSe and CdSe/TiO₂ nanoparticles. *J. Mol. Catal. A-Chem.*, **247**, 268-274.
77. **Ho, W., J. C. Yu and S. Lee** (2006) Low-temperature hydrothermal synthesis of S-doped TiO₂ with visible light photocatalytic activity. *J. Solid State Chem.*, **179**, 1171-1176.

78. **Ho, W., J. C. Yu, J. Lin, J. Yu and P. Li** (2004) Preparation and photocatalytic behavior of MoS₂ and WS₂ nanocluster sensitized TiO₂. *Langmuir*, **20**, 5865-5869.
79. **Hoigne, J.** (1998) Chemistry of aqueous ozone and transformation of pollutants by ozone and advanced oxidation processes, in: J. Hrubec (Ed.), *The Handbook of Environmental Chemistry, vol. 5, part C, Quality and Treatment of Drinking Water, Part II*, Springer, Berlin Heidelberg.
80. **Hoigne, J., and H. Bader** (1983) Rate constants of reaction of ozone with organic and inorganic compounds in water. Part II. Dissociating organic compounds, *Water Res.*, **17**, 185-194.
81. **Hossain, F.M., G.E. Murch, L. Sheppard and J. Nowotny** (2007) *Ab initio* electronic structure calculation of oxygen vacancies in rutile titanium dioxide. *Solid State Ionics*, **178**, 319-325.
82. **Howe, R.F. and M. Gratzel** (1985) EPR observation of trapped electrons in colloidal titanium dioxide. *J. Phys. Chem.*, **89**, 4495-4499.
83. **Hu, X., T. Zhang, Z. Jin, J. Zhang, W. Xu, J. Yan, J. Zhang, L. Zhang and Y. Wu** (2008) Fabrication of carbon-modified TiO₂ nanotube arrays and their photocatalytic activity. *Mater. Lett.*, **62**, 4579-4581.
84. **Huang, H., D. Li, Q. Lin, W. Zhang, Y. Shao, Y. Chen, M. Sun and X. Fu** (2009) Efficient degradation of benzene over LaVO₄/TiO₂ nanocrystalline heterojunction photocatalyst under visible light irradiation. *Environ. Sci. Technol.*, **43**, 4164-4168.
85. **Huang, Y., W. Ho, S. Lee, L. Zhang, G. Li and J. C. Yu** (2008) Effect of carbon doping on the mesoporous structure of nanocrystalline titanium dioxide and its solar-light-driven photocatalytic degradation of NO_x. *Langmuir*, **24**, 3510-3516.
86. **Huang, Y., W. Ho, Z. Ai, X. Song, L. Zhang and S. Lee** (2009) Aerosol-assisted flow synthesis of B-doped, Ni-doped and B-Ni-codoped TiO₂ solid and hollow microspheres for photocatalytic removal of NO. *Appl. Catal. B-Environ.*, **89**, 398-405.
87. **Hurum, D.C., A.G. Agrios, K.A. Gray, T. Rajh and M.C. Thurnauer** (2003) Explaining the enhanced photocatalytic activity of Degussa P25 mixed-phase TiO₂ using EPR. *J. Phys. Chem. B*, **107**, 4545-4549.
88. **Igarashi, H., H. Ushida, M. Suzuki, Y. Sasaki and M. Watanabe** (1997) Removal of carbon monoxide from hydrogen-rich fuels by selective oxidation over platinum catalyst supported on zeolite. *Appl. Catal. A-Gen.*, **159**, 159-169.
89. **Ihara, T., M. Miyoshi, M. Ando, S. Sugihara and Y. Iriyama** (2001) Preparation of a visible-light-active TiO₂ photocatalyst by RF plasma

treatment. *J. Mater. Sci.*, **36**, 4201-4207.

90. **Irie, H., S. Washizuka and K. Hashimoto** (2006) Hydrophilicity on carbon-doped TiO₂ thin films under visible light. *Thin Solid Films*, **510**, 21-25.
91. **Irie, H., Y. Watanabe and K. Hashimoto** (2003) Nitrogen-concentration dependence on photocatalytic activity of TiO_{2-x}N_x powders. *J. Phys. Chem. B*, **107**, 5483-5486.
92. **Iwasaki, M., M. Hara, H. Kawada, H. Tada and S. Ito** (2000) Cobalt ion-doped TiO₂ photocatalyst response to visible light. *J. Colloid Interf. Sci.*, **224**, 202-204.
93. **Izumi, Y., T. Itoi, S. Peng, K. Oka and Y. Shibata** (2009) Site structure and photocatalytic role of sulphur or nitrogen-doped titanium oxide with uniform mesopores under visible light. *J. Phys. Chem. C*, **113**, 6706-6718.
94. **Janus, M., M. Inagaki, B. Tryba, M. Toyoda and A.W. Morawski** (2006) Carbon-modified TiO₂ photocatalyst by ethanol carbonization. *Appl. Catal. B-Environ.*, **63**, 272-276.
95. **Jones, I.Z., R.A. Bennett and M. Bowker** (1999) CO oxidation on Pd(110): a high-resolution XPS and molecular beam study. *Surf. Sci.*, **439**, 235-248.
96. **Justicia, I., P. Ordejon, G. Canto, J.L. Mozos, J. Fraxedas, G.A. Battiston, R. Gerbasi and A. Figueras** (2002) Designed self-doped titanium oxide thin films for efficient visible-light photocatalysis. *Adv. Mater.*, **14**, 1399-1402.
97. **Kahlich, M.J., A. Gasteiger and R.J. Behm** (1997) Kinetics of the selective CO oxidation in H₂-rich gas on Pt/Al₂O₃. *J. Catal.*, **171**, 93-105.
98. **Kahlich, M.J., A. Gasteiger and R.J. Behm** (1999) Kinetics of the selective low-temperature oxidation of CO in H₂-rich gas over Au/ α -Fe₂O₃. *J. Catal.*, **182**, 430-440.
99. **Kamat, P. V.** (2007) Meeting the clean energy demand: Nanostructure architectures for solar energy conversion. *J. Phys. Chem. C*, **111**, 2834-2860.
100. **Kaneco, M. and I. Okura** (2002) *Photocatalysis: Science and Technology*. Springer-Verlag, Berlin.
101. **Kang, M. G., H.E. Han and K.J. Kim** (1999) Enhanced photodecomposition of 4-chlorophenol in aqueous solution by deposition of CdS on TiO₂. *J. Photochem. Photobiol. A: Chem.*, **125**, 119-125.
102. **Kato, H. and A. Kudo** (2001) Water splitting into H₂ and O₂ on alkali tantalate photocatalysts ATaO₃ (A = Li, Na, and K). *J. Phys. Chem. B*, **105**, 4285-4292.

103. **Kato, H., K. Asakura and A. Kudo** (2003) Highly efficient water splitting into H₂ and O₂ over Lanthanum-doped NaTaO₃ photocatalysts with high crystallinity and surface nanostructure. *J. Am. Chem. Soc.*, **125**, 3082-3089.
104. **Kikuchi, H., M. Kitano, M. Takeuchi, M. Matsuoka, M. Anpo and P.V. Kamat** (2006) Extending the photoresponse of TiO₂ to the visible light region: photoelectrochemical behavior of TiO₂ thin films prepared by the radio frequency magnetron sputtering deposition method. *J. Phys. Chem. B*, **110**, 5537-5541.
105. **Kim, D.H., H.S. Hong, S.J. Kim, J.S. Song and K.S. Lee** (2004) Photocatalytic behaviors and structural characterization of nanocrystalline Fe-doped TiO₂ synthesized by mechanical alloying. *J. Alloys Comp.*, **375**, 259-264.
106. **Kiwi, J., C. Pulgarin, P. Peringer and M. Gratzel** (1993) Beneficial effect of homogeneous photo-Fenton pretreatment upon the biodegradation of anthraquinone sulfonate in wastewater treatment. *Appl. Catal. B: Environ.*, **3**, 85-99.
107. **Klosek, S. and Raftery, D.** (2002) Visible light driven V-doped TiO₂ photocatalyst and its photooxidation of ethanol. *J. Phys. Chem. B*, **105**, 2815-2819.
108. **Koelsch, M., S. Cassaignon, J.F. Guillemoles and J.P. Jolivet** (2002) Comparison of optical and electrochemical properties of anatase and brookite TiO₂ synthesized by the sol-gel method. *Thin solid films*, **403**, 312-319.
109. **Kolthoff, I.M., P.J. Elving and E.B. Sandell** (1963) *Treatise on analytical chemistry, Part II, Vol 8*, Interscience publishers, New York.
110. **Kongkanand, A. and P. V. Kamat** (2007) Electron storage in single wall carbon nanotubes. Fermi level equilibration in semiconductor-SWCNT suspensions. *ACS Nano*, **1**, 13-21.
111. **Kosmulski, M.** (2002) The significance of the difference in the point of zero charge between rutile and anatase. *Adv. Colloid Interfac.*, **99**, 255-264.
112. **Kudo, A. and I. Mikami** (1998) New In₂O₃(ZnO)_m photocatalysts with laminal structure for visible light-induced H₂ or O₂ evolution from aqueous solutions containing sacrificial reagents. *Chem. Lett.*, **27**, 1027-1028.
113. **Kudo, A. and Y. Miseki** (2009) Heterogeneous photocatalyst materials for water splitting. *Chem. Soc. Rev.*, **38**, 253-278.
114. **Landsberg, P.T.** (1991) *Recombination in Semiconductors*. Cambridge University Press, Cambridge.
115. **Lee, D.H., J.G. Park, K.J. Choi, H.J. Choi and D.W. Kim** (2008) Preparation of brookite-type TiO₂/Carbon nanocomposite electrodes for application to Li ion batteries. *Eur. J. Inorg. Chem.* **2008**, 878-882.

116. **Li, B., X. Z. Li and K.W. Cheah**, (2005) Photocatalytic activity of Neodymium ion doped TiO₂ for 2-Mercaptobenzothiazole degradation under visible light irradiation. *Environ. Chem.*, **2**, 130-137.
117. **Li, D., H. Haneda, N. K. Labhsetwar, S. Hishita and N. Ohashi** (2005) Visible-light-driven photocatalysis on fluorine-doped TiO₂ powders by the creation of surface oxygen vacancies. *Chem. Phys. Lett.*, **401**, 579-584.
118. **Li, F., Y. Jiang, M. Xia, M. Sun, B. Xue, D. Liu and X. Zhang** (2009) Effect of the P/Ti ratio on the visible-light photocatalytic activity of P-doped TiO₂. *J. Phys. Chem. C*, **113**, 18134–18141.
119. **Li, F.B., X.Z. Li and K.W. Cheah** (2005) Photocatalytic activity of Neodymium ion doped TiO₂ for 2-mercaptobenzothiazole degradation under visible light irradiation. *Environ. Chem.*, **2**, 130-137.
120. **Li, F.B., X.Z. Li, C.H. Ao, S.C. Lee and M.F. Hou** (2005a) Enhanced photocatalytic degradation of VOCs using Ln³⁺-TiO₂ catalysts for indoor air purification. *Chemosphere* **59**, 787-800.
121. **Li, F.B., X.Z. Li, M.F. Hou, K.W. Cheah and W.C.H. Choy** (2005b) Enhanced photocatalytic activity of Ce³⁺-TiO₂ for 2-mercaptobenzothiazole degradation in aqueous suspension for odour control. *Appl. Catal. A-Gen.*, **285**, 181-189.
122. **Li, M., S. Zhou, Y. Zhang, G. Chen and Z. Hong** (2008) One-step solvothermal preparation of TiO₂/C composites and their visible-light photocatalytic activities. *Appl. Surf. Sci.*, **254**, 3762-3766.
123. **Li, W., X. Gong, G. Lu and A. Selloni** (2008) Different reactivities of TiO₂ polymorphs: Comparative DFT calculations of water and formic acid adsorption at anatase and brookite TiO₂ surfaces. *J. Phys. Chem. C*, **112**, 6594-6596.
124. **Li, Y., M. Ma, S. Sun, W. Yan and Y. Ouyang** (2008) Preparation of TiO₂-carbon surface composites with high photoactivity by supercritical pretreatment and sol-gel processing *Appl. Surf. Sci.*, **254**, 4154-4158.
125. **Lin, L., W. Lin, Y. Zhu, B. Zhao and Y. Xie** (2005) Phosphor-doped titania - a novel photocatalyst active in visible light. *Chem. Lett.*, **34**, 284-285.
126. **Liu, B., L. Wen and X. Zhao** (2007) The photoluminescence spectroscopic study of anatase TiO₂ prepared by magnetron sputtering. *Mater. Chem. Phys.*, **106**, 350-353.
127. **Liu, B., X. Zhao, N. Zhang, Q. Zhao, X. He and J. Feng** (2005) Photocatalytic mechanism of TiO₂-CeO₂ films prepared by magnetron sputtering under UV and visible light. *J. Surf. Sci.*, **595**, 203-211.

128. **Liu, G., H. G. Yang, X. Wang, L. Cheng, J. Pan, G. Q. M. Lu and H. M. Cheng** (2009a) Visible light responsive nitrogen doped anatase TiO₂ sheets with dominant {001} facets derived from TiN. *J. Am. Chem. Soc.*, **131**, 12868-13182.
129. **Liu, G., X. Wang, Z. Chen, H. M. Cheng and G. Q. M. Lu** (2009b) The role of crystal phase in determining photocatalytic activity of nitrogen doped TiO₂. *J. Colloid. Interf. Sci.*, **329**, 331-338.
130. **Liu, G., Y. Zhao, C. Sun, F. Li, G. Q. Lu and H. M. Cheng** (2008) Synergistic effects of B/N doping on the visible-light photocatalytic activity of mesoporous TiO₂. *Angew. Chem. Int. Edit.*, **47**, 4516-4520.
131. **Liu, H. and L. Gao** (2004) Codoped rutile TiO₂ as a new photocatalyst for visible light irradiation. *Chem. Lett.*, **33**, 730-731.
132. **Liu, Y. L., Y. Xing, H.F. Yang, Z.M. Liu, Y. Yang, G.L. Shen and R.Q. Yu** (2005) Ethanol gas sensing properties of nano-crystalline cadmium stannate thick films doped with Pt. *Anal. Chim. Acta*, **527**, 21-26.
133. **Liu, Z.P., X.Q. Gong, J. Kohanoff, C. Sanchez and P. Hu** (2003) Catalytic role of metal oxides in gold-based catalysts: A first principles study of co oxidation on TiO₂ supported Au. *Phys. Rev. Lett.*, **91**, 266102 (1-4).
134. **Lo, S.C., C. F. Lin, C. H. Wu and P.H. Hsieh** (2004) Capability of coupled CdSe/TiO₂ for photocatalytic degradation of 4-chlorophenol. *J. Hazard. Mater.*, **114**, 183-190.
135. **Lopez, N. and J. Norskov** (2002) Catalytic CO oxidation by a gold nanoparticle: A density functional study. *J. Am. Chem. Soc.*, **124**, 11262-11263.
136. **Lopez, N., J.K. Norkov, T.V.W. Janssens, A. Carlsson, A. P. Molina, B.S. Clausen and J.D. Grunwaldt** (2004) The adhesion and shape of nanosized Au particles in a Au/TiO₂ catalyst. *J. Catal.*, **225**, 86-94.
137. **Lopez, N., T.V.W. Janssens, B.S. Clausen, Y. Xu, M. Mavrikakis, T. Bligaard and J.K. Norskov** (2004) On the origin of the catalytic activity of gold nanoparticles for low-temperature CO oxidation. *J. Catal.*, **223**, 232-235.
138. **Lundgren, E., J. Gustafson, A. Resta, J. Weissenrieder, A. Mikkelsen, J.N. Andersen, L. Köhler, G. Kresse, J. Klikovits, A. Biederman, M. Schmid and P. Varga** (2005) The surface oxide as a source of oxygen on Rh (111). *J. Elec. Spec. Rel. Phenom.*, **144**, 367-372.
139. **Luo, W., Z. Li, X. Jiang, T. Yu, L. Liu, X. Chen, J. Ye and Z. Zou** (2008) Correlation between the band positions of (SrTiO₃)_{1-x} (LaTiO₂N)_x solid solutions and photocatalytic properties under visible light irradiation. *Phys. Chem. Chem. Phys.*, **10**, 6717-6723.

140. **Madhavi, S. and W. Tim** (2007) Degradation of methylene blue by three-dimensionally ordered macroporous titania. *Environ. Sci. Technol.*, **41**, 4405-4409.
141. **Maeda, K. and K. Domen** (2010) Solid solution of GaN and ZnO as a stable photocatalyst for overall water splitting under visible light. *Chem. Mater.*, **22**, 612-623.
142. **Maeda, K., M. Eguchi, W.J. Youngblood and T.E. Mallouk**, (2008) Niobium oxide nanoscrolls as building blocks for dye-sensitized hydrogen production from water under visible light irradiation. *Chem. Mater.*, **20**, 6770-6778.
143. **Maeda, M. and T. Watanabe** (2006) Visible light photocatalysis of nitrogen-doped titanium oxide films prepared by plasma-enhanced chemical vapour deposition. *J. Electrochem. Soc.*, **153**, C186-C189.
144. **Majzlan, J., A. Navrotsky and W.H. Casey** (2000) Surface enthalpy of boehmite. *Clay. Clay. Miner.*, **48**, 699-707.
145. **Manzoli, M., A. Chiorino and F. Boccuzzi** (2003) FTIR study of nanosized gold on ZrO₂ and TiO₂. *Surf. Sci.*, **532**, 377-382.
146. **Mavrikakis, M., P. Stoltze and J.K. Norskov** (2000) Making gold less noble. *Catal. Lett.*, **64**, 101-106.
147. **McClure, S. M. and D. W. Goodman** (2009) New insights into catalytic CO oxidation on Pt-group metals at elevated pressures. *Chem. Phys. Lett.*, **469**, 1-13.
148. **McHale, J. M., A. Auroux, A.J. Perrotta and A. Navrotsky** (1997) Surface energies and thermodynamic phase stability in nanocrystalline aluminas. *Science*, **277**, 788-791.
149. **McIntosh, D. and G.A. Ozin** (1976) Direct synthesis using gold atoms. Monodioxygen gold, Au (O₂). *Inorg. Chem.*, **15**, 2869-2871.
150. **Meyer, R., C. Lemire, S. Shaikhutdinov and H.J. Freund** (2004) Surface chemistry of catalysis by gold. *Gold Bull.*, **37**, 72-124.
151. **Mills, G., M.S. Gordon and H. Metiu** (2002) The adsorption of molecular oxygen on neutral and negative Au_n clusters (*n* = 2-5). *Chem. Phys. Lett.*, **359**, 493-499.
152. **Mishra, V.S., V.V. Mahajani and J.B. Joshi** (1995) Wet air oxidation. *Ind. Eng Chem. Res.*, **34**, 2-48.
153. **Miyauchi, M., A. Nakajima, K. Hashimoto and T. Watanabe** (2000) A highly hydrophilic thin film under 1 μW/cm² UV illumination. *Adv. Mater.*, **12**, 1923-1927.

154. **Moreau, F. and G.C. Bond** (2007) Influence of the surface area of the support on the activity of gold catalysts for CO oxidation. *Catal. Today*, **122**, 215-221.
155. **Morikawa, T., Y. Irokawa and T. Ohwaki** (2006) Enhanced photocatalytic activity of TiO_{2-x}N_x loaded with copper ions under visible light irradiation. *Appl. Catal. A-Gen.*, **314**, 123-127.
156. **Munuera, G., J.P. Espinoa, A. Fernandez, P. Malet and A.R.G. Elipe** (1990) TiO₂ corrosion during water photocleavage using Rh/TiO₂ suspensions. *J. Chem. Soc. Faraday T. 1*, **86**, 3441-3445.
157. **Murray, C. and A. Lopez** (2002), *The World Health Report 2002, Annex to Table 9*, pp 224, World Health Organization, Geneva.
158. **Nakamura, R., T. Tanaka and Y. Nakato** (2004) Mechanism for visible light responses in anodic photocurrents at N-doped TiO₂ film electrodes. *J. Phys. Chem. B*, **108**, 10617-10620.
159. **Neumann, B., P. Bogdanoff, H. Tributsch, S. Sakthivel and H. Kisch** (2005) Electrochemical mass spectroscopic and surface photovoltage studies of catalytic water photooxidation by undoped and carbon-doped titania. *J. Phys. Chem. B*, **109**, 16579-16586.
160. **Nolan, M., S.C. Parker and G.W. Watson** (2006) Reduction of NO₂ on ceria surfaces. *J. Phys. Chem. B*, **110**, 2256-2262.
161. **Notowny, M. K., L.R. Sheppard, T. Bak and J. Notowny** (2008) Defect chemistry of Titanium Dioxide. Application of defect engineering in processing of TiO₂-based photocatalysts. *J. Phys. Chem. C*, **112**, 5275-5300.
162. **Ochiai, T., K. Nakata, T. Murakami, A. Fujishima, Y. Yao, D. A. Tryk and Y. Kubota** (2010) Development of solar-driven electrochemical and photocatalytic water treatment system using a boron-doped diamond electrode and TiO₂ photocatalyst. *Water Res.*, **44**, 904-910.
163. **Oh, S.H. and R.M. Sinkevitch** (1993) Carbon monoxide removal from hydrogen-rich fuel cell feed streams by selective catalytic oxidation. *J. Catal.*, **142**, 254-262.
164. **Ohno, T., M. Akiyoshi, T. Umebayashi, K. Asai, T. Mitsui and M. Matsumura** (2004) Preparation of S-doped TiO₂ photocatalysts and their photocatalytic activities under visible light. *Appl. Catal. A-Gen.*, **265**, 115-121.
165. **Ohno, T., T. Mitsui and M. Matsumura** (2003) Photocatalytic activity of S-doped TiO₂ photocatalyst under visible light. *Chem. Lett.*, **32**, 364-365.
166. **Ollis, D. and H. Al-Ekabi** (1993) *Photocatalytic purification of water and air*. Elsevier, New York.
167. **Oloman, C., M. Matte and C. Lum** (1991) Electronic conductivity of graphite fiber fixed-bed electrodes, *J. Electrochem. Soc.*, **138**, 2330-2334.

168. **Osterloh, F.E.** (2008) Inorganic materials as catalysts for photochemical splitting of water. *Chem. Mater.*, **20**, 35–54.
169. **Overbury, S. H., L.O. Soto, H.G. Zhu, B. Lee, M.D. Amiridis and S. Dai** (2004) Comparison of Au catalysts supported on mesoporous titania and silica: Investigation of Au particle size effects and metal-support interactions. *Catal. Lett.*, **95**, 99-106.
170. **Ozer, N.** (2001) Optical properties and electrochromic characterization of sol-gel deposited ceria films. *Sol. Energ. Mater. Sol. C.*, **68**, 391-400.
171. **Pal, A., S. Shah and S. Devi** (2007) Synthesis of Au, Ag and Au–Ag alloy nanoparticles in aqueous polymer solution. *Colloid. Surface. A*, **302**, 51-57.
172. **Pan, C., X. Li, F. Wang and L. Wang** (2008) Synthesis of bismuth oxide nanoparticles by the polyacrylamide gel route *Ceram. Int.*, **34**, 439-441.
173. **Paola, A. D., M. Bellardita, R. Ceccato, L. Palmisano and F. Parrino** (2009) Highly active photocatalytic TiO₂ powders obtained by thermohydrolysis of TiCl₄ in water. *J. Phys. Chem. C*, **113**, 15166-15174.
174. **Park, J.H., S. Kim and A.J. Bard** (2006) Novel carbon-doped TiO₂ nanotube arrays with high aspect ratios for efficient solar water splitting. *Nano Lett.*, **6**, 24-28.
175. **Park, J.Y., C. Lee, K.W. Jung and D. Jung** (2009) Structure related photocatalytic properties of TiO₂. *Bull. Korean. Chem. Soc.*, **30**, 402-404.
176. **Park, O.K. and Y.S. Kang** (2005) Preparation and characterization of silica-coated TiO₂ nanoparticle. *Colloid. Surface. A*, **257**, 261-265.
177. **Parra, R. S., I. H. Perez, M. E. Rincon, S. L. Ayala and M. C. R. Ahumada** (2003) Visible light-induced degradation of blue textile azo dye on TiO₂/CdO–ZnO coupled nanoporous films. *Sol. Energ. Mat. Sol. C.*, **76**, 189-199.
178. **Patsalas, P., S. Logothetidis, L. Sygellou and S. Kennou** (2003) Structure-dependent electronic properties of nanocrystalline cerium oxide films. *Phys. Rev. B*, **68**, 35104(1-13).
179. **Pavasupree, S., Y. Suzuki, S.P. Art and S. Yoshikawa** (2005) Preparation and characterization of mesoporous TiO₂–CeO₂ nanopowders respond to visible wavelength. *J. Solid State Chem.*, **178**, 128-134.
180. **Peiro, A.M., C. Colombo, G. Doyle, J. Nelson, A. Mills and J.R. Durrant** (2006) Photochemical reduction of oxygen adsorbed to nanocrystalline TiO₂ films: A transient absorption and oxygen scavenging study of different TiO₂ preparations. *J. Phys. Chem B*, **110**, 23255-23263.
181. **Pelaez, M., A. A. de la Cruz, E. Stathatos, P. Falaras and D. D. Dionysiou** (2009) Visible light-activated N-F-codoped TiO₂ nanoparticles for the

- photocatalytic degradation of microcystin-LR in water. *Catal. Today*, **144**, 19-25.
182. **Pichat, P., M.N. Mozzanega and H. Courbon** (1987) Investigation of the mechanism of photocatalytic alcohol dehydrogenation over Pt/TiO₂ using poisons and labelled ethanol. *J. Chem. Soc, Faraday T. 1*, **83**, 697-704.
 183. **Pietron, J.J., R.M. Stroud and D.R. Rolison** (2002) Using three dimensions in catalytic mesoporous nanoarchitectures. *Nano Lett.*, **2**, 545-549.
 184. **Pignatello, J.J.** (1992) Dark and photoassisted Fe³⁺- catalyzed degradation of chlorophenoxy herbicides by hydrogen peroxide. *Environ. Sci. Technol.*, **26**, 944-951.
 185. **Pottier, A., C. Chaneac, E. Tronc, L. Mazerolles and J.P. Jovilet** (2001) Synthesis of brookite TiO₂ nanoparticles by thermolysis of TiCl₄ in strongly acidic aqueous media. *J. Mater. Chem.*, **11**, 1116-1121.
 186. **Pulgarin, C. and J. Kiwi** (1996) Overview on photocatalytic and electrocatalytic pretreatment of industrial non-biodegradable pollutants and pesticides. *Chimia*, **50**, 50-55.
 187. **Rajeshwar, K.** (1995) Photoelectrochemistry and the environment. *J. Appl. Electrochem.*, **25**, 1067-1082.
 188. **Ranade, M. R., A. Navrotsky, H.Z. Zhang, J.F. Banfield, S.H. Elder, A. Zaban, P.H. Borse, S.K. Kulkarni, G.S. Doran and H.J. Whitfield** (2002). Energetics of nanocrystalline TiO₂. *P. Natl. Acad. Sci. USA*, **99**, 6476-6481.
 189. **Ravelli, D., D. Dondi, M. Fagnoni and A. Albini** (2009) Photocatalysis. A multi-faceted concept for green chemistry. *Chem. Soc. Rev.*, **38**, 1999-2011.
 190. **Reber, J. F. and M. Rusek** (1986) Photochemical hydrogen production with platinized suspensions of Cadmium sulfide and Cadmium Zinc sulfide modified by Silver Sulfide. *J. Phys. Chem.*, **90**, 824-834.
 191. **Remediakis, I. N., N. Lopez and J. K. Norskov** (2005) CO oxidation on rutile-supported Au nanoparticles. *Angew. Chem. Int. Edit.*, **44**, 1824-1826.
 192. **Robert, D.** (2007) Photosensitization of TiO₂ by M_xO_y and M_xS_y nanoparticles for heterogeneous photocatalysis applications. *Catal. Today*, **122**, 20-26.
 193. **Rodriguez, J. A., G. Liu, T. Jirsak, J. Hrbek, Z.P. Chang, J. Dvorak and A. Maiti** (2002) Activation of gold on titania: Adsorption and reaction of SO₂ on Au/TiO₂(110). *J. Am. Chem. Soc.*, **124**, 5242-5250.
 194. **Roessler, S., R. Zimmermann, D. Scharnweber, C. Werner and H. Worch** (2002) Characterization of oxide layers on Ti₆Al₄V and titanium by streaming potential and streaming current measurements. *Colloid. Surface. B*, **26**, 387-395.

195. **Sadezky, A., H. Muckenhuber, H. Grothe, R. Niessner and U. Poschl** (2003) Raman microspectroscopy of soot and related carbonaceous materials: Spectral analysis and structural information. *Carbon*, **43**, 1731-1742.
196. **Sakthivel, S. and H. Kisch** (2003) Daylight photocatalysis by carbon-modified titanium dioxide. *Angew. Chem. Int. Edit.*, **42**, 4908-4911.
197. **Sakthivel, S., M. Janczarek, and H. Kisch** (2004) Visible light activity and photoelectrochemical properties of Nitrogen-doped TiO₂. *J. Phys. Chem. B*, **108**, 19384-19387.
198. **Sanchez, A., S. Abbet, U. Heiz, W.D. Schneider, H. Hakkinen, R.N. Barnett and U. Landman** (1999) When gold is not noble: Nanoscale gold catalysts. *J. Phys. Chem. A*, **103**, 9573-9578.
199. **Sanchez, R.M.T., A. Ueda, K. Tanaka and M. Haruta** (1997) Selective oxidation of CO in hydrogen over gold supported on manganese oxides. *J. Catal.*, **168**, 125-127.
200. **Sandell, E.B.** (1959) *Colorimetric determination of traces of metals*, 3rd Edition. Interscience publishers, London.
201. **Sankaran, M. and B. Viswanathan** (2006) A DFT study of the electronic property of gold nanoclusters (Au_x, x =1-12 atoms). *Bull. Catal. Soc. India*, **5**, 26-32.
202. **Sathish, M., B. Viswanathan and R.P. Viswanath** (2007) Characterization and photocatalytic activity of N-doped TiO₂ prepared by thermal decomposition of Ti-melamine complex. *Appl. Catal. B-Environ.*, **74**, 307-312.
203. **Sathish, M., B. Viswanathan, R.P. Viswanath and C.S. Gopinath** (2005) Synthesis, characterization, electronic structure, and photocatalytic activity of nitrogen-doped TiO₂ nanocatalyst. *Chem. Mater.*, **17**, 6349-6353.
204. **Sathish, M., R.P. Viswanath and C.S. Gopinath** (2009) N,S-Co-doped TiO₂ nanophotocatalyst: Synthesis, electronic structure and photocatalysis. *J. Nanosci. Nanotechnol.*, **9**, 423-432.
205. **Sato, J., N. Saito, H. Nishiyama and Y. Inoue**, (2001) New photocatalyst group for water decomposition of RuO₂-loaded p-block metal (In, Sn, and Sb) oxides with d¹⁰ configuration. *J. Phys. Chem. B*, **105**, 6061-6063.
206. **Sato, J., N. Saito, H. Nishiyama and Y. Inoue**, (2003) Photocatalytic activity for water decomposition of indates with octahedrally coordinated d¹⁰ configuration. I. Influences of preparation conditions on activity. *J. Phys. Chem. B*, **107**, 7965-7969.
207. **Sayilkan H.** (2007) Improved photocatalytic activity of Sn⁴⁺-doped and undoped TiO₂ thin film coated stainless steel under UV- and VIS-irradiation. *Appl. Catal. A-Gen.*, **319**, 202-204.

208. **Schubert, M.M., S. Hackenberg, A.C.V. Veen, M. Muhler, V. Plzak and R.J. Behm** (2001) CO oxidation over supported gold catalysts—"inert" and "active" support materials and their role for the oxygen supply during reaction. *J. Catal.*, **197**, 113-122.
209. **Serpone, N. and E. Pelizzetti** (1989) *Photocatalysis-fundamentals and applications*. Wiley Interscience, New York.
210. **Shi, J. Y., W.H. Leng, W.C. Zhu, J.Q. Zhang and C.N. Cao** (2006) Electrochemically assisted photocatalytic oxidation of nitrite over Cr-doped TiO₂ under visible light. *Chem. Eng. Technol.*, **29**, 146-154.
211. **Shimodaira, Y., H. Kato, H. Kobayashi and A. Kudo** (2006) Photophysical properties and photocatalytic activities of bismuth molybdates under visible light irradiation. *J. Phys. Chem. B*, **110**, 17790–17797.
212. **Sun, S., W. Wang, L. Zhang and M. Shang** (2009) Visible light-induced photocatalytic oxidation of phenol and aqueous ammonia in flowerlike Bi₂Fe₄O₉ suspensions. *J. Phys. Chem. C*, **113**, 12826-12831.
213. **Tada, H., T. Mitsui, T. Kiyonaga, T. Akita and K. Tanaka** (2006) All-solid-state Z-scheme in CdS–Au–TiO₂ three-component nanojunction system. *Nature Mater.*, **5**, 782-786.
214. **Tandon, S.P. and J.P. Gupta** (1970) Measurement of forbidden energy gap of semiconductors by diffuse reflectance technique. *Phys. Status Solidi B*, **38**, 363-367.
215. **Titus, M. P., V.G. Molina, M.A. Banos, J. Gimenez and S. Esplugas** (2004) Degradation of chlorophenols by means of advanced oxidation processes: a general review. *Appl. Catal. B Environ.*, **47**, 219-256.
216. **Tong, T., J. Zhang, B. Tian, F. Chen, D. He and M. Anpo**, (2007) Preparation of Ce–TiO₂ catalysts by controlled hydrolysis of titanium alkoxide based on esterification reaction and study on its photocatalytic activity. *J. Colloid Interface Sci.*, **315**, 382-388.
217. **Torres, G.R., T. Lindgren, J. Lu, C.G. Granqvist and S.E. Lindquist** (2004) Photoelectrochemical study of nitrogen-doped titanium dioxide for water oxidation. *J. Phys. Chem. B*, **108**, 5995-6003.
218. **Tunesi, S. and M. Anderson** (1991) Influence of chemisorption on the photodecomposition of salicylic acid and related compounds using suspended titania ceramic membranes. *J. Phys. Chem.*, **95**, 3399-3405.
219. **Valden, M., S. Pak, X. Lai and D.W. Goodman** (1998) Structure sensitivity of CO oxidation over model Au/TiO₂ catalysts. *Catal. Lett.*, **56**, 7-10.

220. **Valden, M., X. Lai and D.W. Goodman** (1998) Onset of catalytic activity of gold clusters on titania with the appearance of nonmetallic properties. *Science*, **281**, 1647-1650.
221. **Valentin, C. D., G. Pacchioni, H. Onishi and A. Kudo** (2009) Cr/Sb co-doped TiO₂ from first principles calculations. *Chem. Phys. Lett.*, **469**, 166-171.
222. **Viswanathan, B.** (2003) Photocatalytic processes – Selection criteria for the choice of materials. *Bull. Catal. Soc. India*, **2**, 71-74.
223. **Viswanathan, B.** (2005) Photo electrochemical production of hydrogen – A dream or reality?. *Photo/Electrochemistry & Photobiology in the Environment, Energy and Fuel*, 1-12.
224. **Wang, D. F., Z. G. Zou and J. H. Ye** (2005) Photocatalytic water splitting with the Cr-doped Ba₂In₂O₅/In₂O₃ composite oxide semiconductors. *Chem. Mater.*, **17**, 3255–3261.
225. **Wang, Y. D., X.H. Wu, Z.L. Zhou and Y.F. Li** (2003) The reliability and lifetime distribution of SnO₂ and CdSnO₃ gas sensors for butane. *Sensor. Actuat. B Chem.*, **92**, 186-190.
226. **Wei, H., Y. Wu, N. Lun and F. Zhao** (2004) Preparation and photocatalysis of TiO₂ nanoparticles co-doped with nitrogen and lanthanum. *J. Mater. Sci.*, **39**, 1305-1308.
227. **Weiherr, N., E. Bus, L. Delannoy, C. Louis, D.E. Ramaker, J.T. Miller and J.A.V. Bokhoven** (2006) Structure and oxidation state of gold on different supports under various CO oxidation conditions *J. Catal.*, **240**, 100-107.
228. **Wolf, A. and F. Schuth** (2002) A systematic study of the synthesis conditions for the preparation of highly active gold catalysts. *Appl. Catal. A-Gen.*, **226**, 1-13.
229. **Wu, L., J.C. Yu and X. Fu** (2006) Characterization and photocatalytic mechanism of nanosized CdS coupled TiO₂ nanocrystals under visible light irradiation. *J. Mol. Catal. A-Chem.*, **244**, 25-32.
230. **Wu, X., L. Senapati, S.K. Nayak, A. Selloni and M. Hajaligol** (2002) A density functional study of carbon monoxide adsorption on small cationic, neutral, and anionic gold clusters. *J. Chem. Phys.*, **117**, 4010-4015.
231. **Wu, X., W.P. Mulligan and T.J. Coutts** (1996) Recent developments in RF sputtered cadmium stannate films. *Thin Solid Films*, **286**, 274-276.
232. **Wu, Y., J. Zhang, L. Xiao and F. Chen** (2009) Preparation and characterization of TiO₂ photocatalysts by Fe³⁺ doping together with Au deposition for the degradation of organic pollutants. *Appl. Catal. B-Environ.*, **88**, 525-532.

233. **Xiao, Q., J. Zhang, C. Xiao, Z. Si and X. Tan** (2008) Solar photocatalytic degradation of methylene blue in carbon-doped TiO₂ nanoparticles suspension. *Sol. Energy*, **82**, 706-713.
234. **Xie, Y. and C. Yuan** (2004a) Photocatalysis of neodymium ion modified TiO₂ sol under visible light irradiation. *Appl. Surf. Sci.*, **221**, 17-24.
235. **Xie, Y. and C. Yuan** (2004b) Characterization and photocatalysis of Eu³⁺-TiO₂ sol in the hydrosol reaction system. *Mater. Res. Bull.*, **39**, 533-543.
236. **Xie, Y., C. Yuan and X. Li** (2005a) Photocatalytic degradation of X-3B dye by visible light using lanthanide ion modified titanium dioxide hydrosol system. *Colloid. Surface. A*, **252**, 87-94.
237. **Xie, Y., C. Yuan and X. Li** (2005b) Photosensitized and photocatalyzed degradation of azo dye using Lnⁿ⁺-TiO₂ sol in aqueous solution under visible light irradiation. *Mater. Sci. Eng. B-Adv.*, **117**, 325-333.
238. **Xu, J., Y. Ao, D. Fu and C. Yuan** (2008) Low-temperature preparation of F-doped TiO₂ film and its photocatalytic activity under solar light. *Appl. Surf. Sci.*, **254**, 3033-3038.
239. **Xu, X. and D.W. Goodman** (1993) An infrared and kinetic study of carbon monoxide oxidation on model silica-supported palladium catalysts from 10⁻⁹ to 15 Torr. *J. Phys. Chem.*, **97**, 7711-7718.
240. **Xu, Y. and M.A.A. Schoonen** (2000) The absolute energy positions of conduction and valence bands of selected semiconducting minerals. *Am. Mineral.*, **85**, 543-556.
241. **Xu, Y., H. Chen, Z. Zeng and B. Lei** (2006) Investigation on mechanism of photocatalytic activity enhancement of nanometer cerium-doped titania. *Appl. Surf. Sci.*, **252**, 8565-8570.
242. **Yamakata, A., T.A. Ishibashi, K. Takeshita and H. Onishi** (2005) Time-resolved infrared absorption study of photochemical reactions over metal oxides. *Top. Catal.*, **35**, 211-216.
243. **Yamaki, T., T. Sumita and S. Yamamoto** (2002) Formation of TiO_{2-x}F_x compounds in fluorine-implanted TiO₂. *J. Mater. Sci. Lett.*, **21**, 33-35.
244. **Yamanaka, T. and K. Tanabe** (1975) New determination of acid-base strength distribution of a common scale on solid surfaces. *J. Phys. Chem.*, **79**, 2409-2411.
245. **Yamashita, Y., M. Tada, M. Kakihana, M. Osada and K. Yoshida** (2002) Synthesis of RuO₂-loaded BaTi_nO_{2n+1} (n= 1, 2 and 5) using a polymerizable complex method and its photocatalytic activity for the decomposition of water. *J. Mater. Chem.*, **12**, 1782-1786.

246. **Yan, W., B. Chen, S.M. Mahurin, S. Dai and S.H. Overbury** (2004) Brookite-supported highly stable gold catalytic system for CO oxidation. *Chem. Commun.*, 1918-1919.
247. **Yan, W., B. Chen, S.M. Mahurin, V. Schwartz, D. R. Mullins, A. R. Lupini, S. J. Pennycook, S. Dai and S. H. Overbury** (2005) Preparation and comparison of supported gold nanocatalysts on anatase, brookite, rutile, and P25 polymorphs of TiO₂ for catalytic oxidation of CO. *J. Phys. Chem. B*, **109**, 10676-10685.
248. **Yang, S., C. Sun, X. Li, Z. Gong and X. Quan** (2010) Enhanced photocatalytic activity for titanium dioxide by co-modifying with silica and fluorine. *J. Hazard. Mater.*, **175**, 258-266.
249. **Yang, X., C. Cao, L. Erickson, K. Hohn, R. Maghirang and K. Klabunde** (2008) Synthesis of visible-light-active TiO₂-based photocatalysts by carbon and nitrogen doping. *J. Catal.*, **260**, 128-133.
250. **Yang, Y., J. Ma, Q. Qin and X. Zhai** (2007) Degradation of nitrobenzene by nano-TiO₂ catalyzed ozonation. *J. Mol. Catal. A-Chem.*, **267**, 41-48.
251. **Yoshihara, T., R. Katoh, A. Furube, Y. Tamaki, M. Murai, K. Hara, S. Murata, H. Arakawa and M. Tachiya** (2004) Identification of reactive species in photoexcited nanocrystalline TiO₂ films by wide-wavelength-range (400–2500 nm) transient absorption spectroscopy. *J. Phys. Chem. B*, **108**, 3817-3823.
252. **Yoshimura, J., Y. Ebina, J. Kondo, K. Domen and A. Tanaka** (1993) Visible light-induced photocatalytic behavior of a layered perovskite-type rubidium lead niobate, RbPb₂Nb₃O₁₀. *J. Phys. Chem.*, **97**, 1970–1973.
253. **Yu, J., Q. Xiang and M. Zhou** (2009) Preparation, characterization and visible-light-driven photocatalytic activity of Fe-doped titania nanorods and first-principles study for electronic structures. *Appl. Catal. B-Environ.*, **90**, 595-602.
254. **Yu, J. C., W. Ho, J. Yu, H. Yip, P. K. Wong and J. Zhao** (2005) Efficient visible-light-induced photocatalytic disinfection on sulfur-doped nanocrystalline titania. *Environ. Sci. Technol.*, **39**, 1175–1179.
255. **Yu, J.C., J.G. Yu, W.K. Ho, Z.T. Jiang and L.Z. Zhang** (2002) Effects of F-doping on the photocatalytic activity and microstructures of nanocrystalline TiO₂ powders. *Chem. Mater.*, **14**, 3808-3816.
256. **Zanella, R., L. Delannoy and C. Louis** (2005) Mechanism of deposition of gold precursors onto TiO₂ during the preparation by cation adsorption and deposition–precipitation with NaOH and urea. *Appl. Catal. A-Gen.*, **291**, 62-72.

257. **Zhang, D.R., Y.H. Kim and Y.S. Kang** (2006) Synthesis and characterization of nanoparticle of TiO₂ co-doped with Sc³⁺ and V⁵⁺ ions. *Curr. Appl. Phys.*, **6**, 801-804.
258. **Zhang, H., G. Chen and D.W. Bahnemann** (2009) Photoelectrocatalytic materials for environmental applications. *J. Mater. Chem.*, **19**, 5089-5121.
259. **Zhang, L., Y. Xu, Y. Song, C. Wu, M. Zhang and Y. Xie** (2009) Nearly monodisperse CuInS₂ hierarchical microarchitectures for photocatalytic H₂ evolution under visible light. *Inorg. Chem.*, **48**, 4003-4009.
260. **Zhang, T., Y. Shen, R. Zhang and X. Liu** (1996) Ammonia-sensing characteristics of Pt-doped CdSnO₃ semiconducting ceramic sensor. *Mater. Lett.*, **27**, 161-164.
261. **Zhao, W., W. Ma, C. Chen, J. Zhao and Z. Shuai** (2004) Efficient degradation of toxic organic pollutants with Ni₂O₃/TiO_{2-x}B_x under visible irradiation. *J. Am. Chem. Soc.*, **126**, 4782-4783.
262. **Zheng, R., L. Lin, J. Xie, Y. Zhu and Y. Xie** (2008) State of doped phosphorus and its influence on the physicochemical and photocatalytic properties of P-doped titania. *J. Phys. Chem. C*, **112**, 15502-15509.
263. **Zheng, R., Y. Guo, C. Jin, J. Xie, Y. Zhu and Y. Xie** (2010) Novel thermally stable phosphorus-doped TiO₂ photocatalyst synthesized by hydrolysis of TiCl₄. *J. Mol. Catal. A-Chem.*, **319**, 46-51.
264. **Zhou, J. X. Wu, A. Duda, G. Teeter and S.H. Demtsu** (2007) The formation of different phases of Cu_xTe and their effects on CdTe/CdS solar cells. *Thin Solid Films*, **515**, 7364-7369.
265. **Zhou, M., J. Yu and B. Cheng** (2006) Effects of Fe-doping on the photocatalytic activity of mesoporous TiO₂ powders prepared by an ultrasonic method. *J. Hazard. Mater.*, **137**, 1838-1847.
266. **Zhu, J., Z. Deng, F. Chen, J. Zhang, H. Chen, M. Anpo, J. Huang and L. Zhang** (2006) Hydrothermal doping method for preparation of Cr³⁺-TiO₂ photocatalysts with concentration gradient distribution of Cr³⁺. *Appl. Catal. B-Environ.*, **62**, 329-335.
267. **Zhu, J., W. Zheng, B. He, J. Zhang and M. Anpo** (2004) Characterization of Fe-TiO₂ photocatalysts synthesized by hydrothermal method and their photocatalytic reactivity for photodegradation of XRG dye diluted in water. *J. Mol. Catal. A-Chem.*, **216**, 35-43.

LIST OF PUBLICATIONS

REFEREED JOURNALS

Magesh, G., B. Viswanathan, R.P. Viswanath and T.K. Varadarajan (2009)
Photocatalytic behavior of CeO₂-TiO₂ system for the degradation of methylene blue.
Indian J. Chem., Sec A, **48A**, 480-488.

OTHER PUBLICATIONS

Magesh, G., B. Viswanathan, R.P. Viswanath and T.K. Varadarajan (2007)
Photocatalytic routes for chemicals. *Photo/Electrochemistry & Photobiology in the Environment, Energy and Fuel*, 321-357.

PRESENTATIONS IN SYMPOSIUM/CONFERENCE

1. **Magesh, G., B. Viswanathan, R. P. Viswanath and T. K. Varadarajan**, 'Visible light photocatalytic activity of Ce modified TiO₂ nanoparticles for methylene blue decomposition', International Conference on Nanomaterials and its Applications (Poster presentation), February 4-6th 2007, NIT, Trichy, India.
2. **Magesh, G., B. Viswanathan, T.K. Varadarajan and R.P. Viswanath**, 'CeO₂-TiO₂ system as visible light photocatalyst for the degradation 4-chlorophenol', Catworkshop-2008 (Poster Presentation), February 18-20, 2008, IMMT, Bhubaneswar, India.
3. **Magesh, G., T.K. Varadarajan and R.P. Viswanath**, 'Enhanced photocatalytic activity of carbon-TiO₂ composites towards pollutant removal', CATSYMP-19, (Poster presentation) January 18-21, 2009, National Chemical Laboratory, Pune, India.
4. **Magesh, G., B. Viswanathan, T.K. Varadarajan and R.P. Viswanath**, 'Cadmium stannates as photocatalysts for decontamination of water', Indo-Hungarian workshop on future frontiers in catalysis (poster presentation) February 16-18, 2010, IIT Madras, Chennai, India.

CURRICULUM VITAE

Name : G. Magesh
Date of Birth : 30th June 1980
Address : New no. 92, Perumal koil street
Kottur
Chennai 600 085

Educational Qualification

Degree	Year	Institution
B.Sc (Chemistry)	2000	Presidency College Chepauk, Chennai 600 005 University of Madras
M.Sc (Chemistry)	2002	Anna University Chennai 600 025
Ph.D (Chemistry)	2010	Indian Institute of Technology Madras Chennai 600 036